POLITECNICO DI MILANO
DEPARTMENT OF MECHANICAL ENGINEERING
DOCTORAL PROGRAMME IN MECHANICAL ENGINEERING

STUDY OF RAIL VEHICLE DYNAMICS AND WHEEL-RAIL CONTACT USING FULL-SCALE ROLLER RIGS

Doctoral Dissertation of:
Binbin Liu

Supervisor:
Prof. Stefano Bruni

Tutor:
Prof. Stefano Beretta

The Chair of the Doctoral Program:
Prof. Maria Bianca Colosimo

2016 – XXVIII

Acknowledgements

The work presented in this thesis was carried out at the Department of Mechanical Engineering, Politecnico di Milano under the supervision of Prof. Stefano Bruni. First and foremost, I would like to thank him for giving me the opportunity to conduct this research, for providing guidance, and for being extremely supportive and understanding when any circumstances interfered with my work. Other than being a great supervisor, a smart, intelligent, knowledgeable expert in his field, he has a very nice and caring personality. It has been a rewarding experience to work with him, and I will forever be grateful for everything he has done for me.

I would also like to thank my tutor Prof. Stefano Beretta and all the members of the Railway Dynamics Research Group in which I am working, for their help, support and all the fun we had together. Thank you to the colleagues and friends at our department. It is a real privilege to work in an environment that one can enjoy.

During the period of my PhD study, also thanks to my supervisor, I had the opportunity to be involved in a joint project at the University of Salford in the UK under the supervision of Prof. T.X. Mei. I would like to thank him for his professional guidance and generous hospitality. It was a very fruitful and enjoyable collaboration. Special thanks also go to Prof. Roger Lewis of the University of Sheffield for giving me access to their measurement data, to Dr. E.A.H. Vollebregt of VORtech CMCC for valuable discussions on contact mechanics, and to Dr. Zili Li of Delft University of Technology for providing relevant materials and valuable discussions. I am also sincerely indebted to Prof. Chengguo Wang, Dr. Junbiao Wang and many former colleagues at China Academy of Railway Sciences and Prof. Jing Zeng of Southwest Jiaotong University for their continuous encouragement and support.

Last, but not least, I am extremely grateful to my family, especially during the time when I am studying abroad, without whom I would not have been able to accomplish anything I have achieved. Thank you to Mum and Dad for all you gave me. Thank you to my brother for your unconditional support. And thank my wife Dan Li for everything. You are the most beautiful thing that has ever happened to me. There is so much I could not have done without you.

<div align="right">

Binbin Liu
Milan, January 2016

</div>

Abstract

Rail vehicle dynamics and wheel-rail contact mechanics are two relevant issues in railway engineering and have been subjected to extensive research since the advent of railways. The powerful computing technique facilitates the problem solving process. However, the conclusions coming from numerical simulations cannot be applied into practice before validation normally by experiments in laboratory or field. The field experiments for these purposes are often challenging due to the difficulties in adequately controlling the test conditions. Roller rigs are a good alternative in this case because they can offer a repeatable environment for a specific test and allow for the use of multiple sensors and data acquisition equipment either difficult or impossible to use in the field. Full-scale roller rigs for tests on a single wheelset are recognized as useful test stands to investigate wheel-rail contact/damage issues and to develop new solutions to extend the life and improve the dynamic behaviour of railway systems. The replacement of the real track by a pair of rollers on the roller rig causes, however, inherent differences between wheel-rail and wheel-roller contact. In order to ensure efficient utilization of the roller rigs and correct interpretation of the test results with respect to the field wheel-rail scenarios, the differences and the corresponding causes must be understood a priori.

The aim of this thesis is to derive the differences between these two systems from both contact mechanics and dynamics points of view based on a full-scale single wheelset roller rig and to find the influence factors of the differences, with the final aim of better translating the results of tests performed on a roller rig to the field case, demonstrating the ability of the experiment and further exploiting the best potential of this test equipment for rail vehicle dynamics and wheel-rail contact study.

In this thesis, an approximate non-Hertzian contact model has been developed for dealing with the wheel-rail and wheel-roller contact problems, which is an extension of the well-known Kik-Piotrowski model with some significant improvements in the accuracy and wider application scope. Furthermore, advanced methods have been proposed to best reproduce the dynamic behaviour of a wheelset in a running condition of interest as obtained either from multibody system simulation or from on-track measurements based on the existing theories and experimental experiences, which will mark a

step forward with respect to presently exiting methods and allow for much increased accuracy of the roller rig tests and widening the scope of ability of this kind of facility. Based on the testing methods developed in this thesis, two typical tests namely the curving test and the wheel wear test on a full-scale roller rig are described in detail. The proposed contact model and roller rig testing methods are expected to be of benefit to a number of institutions which operate roller rigs.

Contents

INTRODUCTION

With the rapid development of high-speed train all over the world, the railway technology has received a renewed interest more than ever. The traditional problems such as rail corrugation and derailment mechanisms have not been understood completely yet and newly emerged problems for modern trains such as mechatronics and aerodynamics become the main concerns in the design of the new generation high-speed trains. Vehicle dynamics and wheel-rail contact mechanics are the most relevant issues among others in railway engineering [93]. In order to better understand the mechanisms underlying the phenomena, many attempts have been made from both theoretical and experimental points of view. However, field experiments on wheel-rail contact mechanics and vehicle dynamics in some special scenarios can prove to be challenging due to the difficulties in adequately controlling the test conditions and data acquisition [58]. Roller rigs are a good alternative to carry out experiments in such cases, thanks to their high controllability and flexibility. They have been used in the railway research community for more than one century for contact theory validation, suspension system optimisation, testing of new concept components, etc. The role they played becomes more and more important in the development of the railway industry.

A few test rigs with new features have been developed recently to meet the demands of rapid development of railway industry around the world, such as the newly opened full-scale roller rig for a single wheelset test in China Academy of Railway Sciences (CARS) [38, 73], another similar one in Korea Railroad Research Institute (KRRI) [1], a full-scale test rig in the Osmannoro Railway Research Centre in Florence, Italy [38], and other two are going to be put into service, one of which is a full-scale roller rig at the University of Huddersfield in the UK, while the other is a scaled test rig at Delft University of Technology in the Netherlands [81].

Among all of the existing roller rigs, the full-scale roller rig for a single wheelset

test is one of the most similar test devices to real wheelset-track system in such a simple configuration from both dynamics and contact mechanics points of view. It represents the best compromise between cost and test ability without loss of the coupling property between dynamics and contact for a suspended wheelset system. Therefore, it has been selected as the main study subject in this work. The BU300 roller rig at Lucchini RS in Italy and the RaSSP roller rig owned by DB Systemtechnik in Germany as shown in Figure 1.1 are the typical practical applications of this kind of roller rig. More details about roller rigs and their applications will be given in Chapter 2.
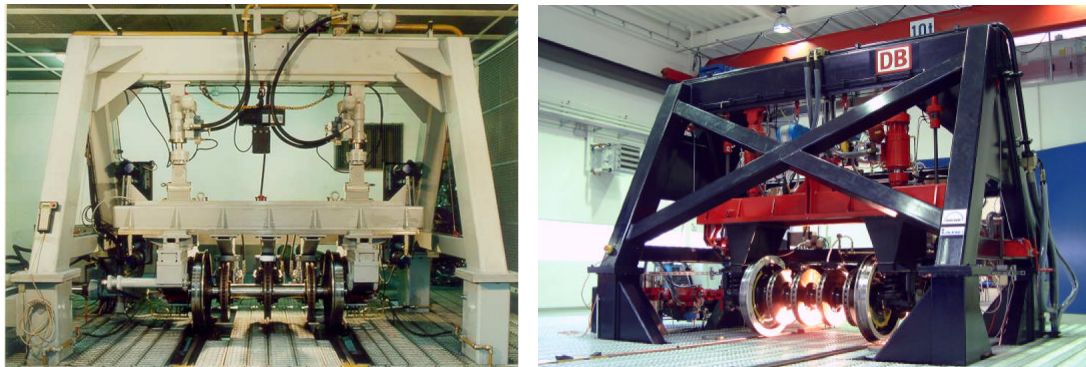
Figure 1.1: *The BU300 rig at Lucchini RS (left) and the RaSSP rig at DB Systemtechnik (right) [99].*

1.1 Motivations and aims

The roller rigs offer the advantages that the experiments are independent of weather conditions, individual phenomena can be investigated, the experiments and the constraints as well as the particular conditions are reproducible [47]. Though there are considerable differences between the dynamics of railway vehicles on roller rigs and on real tracks, these rigs have been proved useful for both basic research and development of innovative designs, as well as for the optimisation of suspensions and vehicle components. However, it should be kept in mind that the roller rig test will never completely replace the field test, due to inherent differences caused by the replacement of the rail by rollers in a roller rig system. Therefore, it is very important to understand the differences between the roller rig test and field test, to find the corresponding causes of the differences, to correctly interpret the test results and to find countermeasures for deviations that might arise between the test on the roller rig and a field test. It is clear that the choice of testing method and the interpretation of testing results are the keys of success to running the tests on a roller rig. However, the description of the testing method, the explanation of the testing principle, the systematic analysis of wheel-roller contact and its differences with respect to the wheel-rail case, the interpretation of the final testing results, and especially the challenges faced in the curving test are seldom addressed in the literature.

There are two principal goals of this thesis: the first is to explore the potential abilities of roller rigs, a full-scale single axle roller rig in particular, based on a comprehensive investigation of the capability of the roller rig to study of the rail vehicle dynamics and wheel-rail contact from theoretical and experimental points of view and the second is to develop an advanced contact model and a complete testing method for interpreting

and translating the testing results on the rig to the corresponding field test case.

The outcomes of this research will hopefully be of benefit to a number of institutions which operate roller rigs for research in railway field. It is not possible to develop one single general method valid for various types of test rigs existing all over the world, but the general methodology proposed and the conclusions obtained in this thesis can be applied at least on a qualitative basis to any roller rigs with similar configurations.

1.2 Methodology and contributions

The methodology used in this thesis is based on a so-called co-simulation technique by constructing a network among multi-body system (MBS) simulation, contact modelling and modern control theory to solve a complex multi-physics problem related to the wheelset dynamics and wheel-rail/roller contact mechanics in a roller rig system.

The main original contributions of this work can be summarized as follows:

- a systematic description of the differences between the wheel-rail and wheel-roller contact systems from global geometry contact to local contact mechanics;

- a new contact model developed for dealing with non-elliptic wheel-rail/roller contact problem considering the effect of yaw angle based on the Kik-Piotrowski method;

- a systematic description of the MBS modelling of a roller rig system and a complete rail vehicle system;

- a set of testing strategies for performing tests on a full-scale roller rig. These are meant to improve the agreement of the dynamic behaviour of a wheelset running on a roller rig and on the track;

- two typical testing cases concerning wheelset curving negotiation and wheel profile wear test are provided respectively in detail.

1.3 Thesis structure

The present work is organized in different chapters, each one dedicated to a particular issue ranging from general dynamics and contact problems in railway field to the theoretical and experimental studies of roller rigs. Hereafter a short description of the content of each chapter is given: the state of the art of research on the application of roller rigs to rail vehicle dynamics and wheel-rail contact mechanics is introduced in Chapter 2. This is followed by a detailed description of wheel-rail and wheel-roller contact analysis including the solutions of geometry contact problem, kinematic problem, normal contact problem and tangential contact problem. A new contact model is proposed based on the well-known Kik-Piotrowski method for dealing with wheel-rail and wheel-roller contact in presence of yaw angle in Chapter 3. It is shown that the new model improves the accuracy regarding the contact size and area as well as the pressure distribution over the contact patch compared with the original method, considering as a reference to software CONTACT.

A detailed description on the MBS modelling of the roller rig and that of a complete rail vehicle is provided in Chapter 4. Chapter 5 describes a general testing procedure

on a full-scale roller rig and the numerical simulation methodology of virtual test for a roller rig. In order to show the practical application of the roller rig to vehicle dynamics and wheel-rail contact study, two challenging topics in this field, namely curving test and wear test on a roller rig are discussed in detail in Chapter 6 and Chapter 7, respectively. The relevant conclusions drawn from this research are summarised and the directions for future work in this field are provided in Chapter 8. The interconnections of the content in each chapter can be described by the relations between system dynamics and local contact mechanics in the whole vehicle-track coupling system as presented in Figure 1.2.

ΔN_i – Normal force at the contact point, ΔU – Displacement,
Tx– Longitudinal tangential force, **Ty**– Longitudinal tangential force, **Mz**- Spin moment,
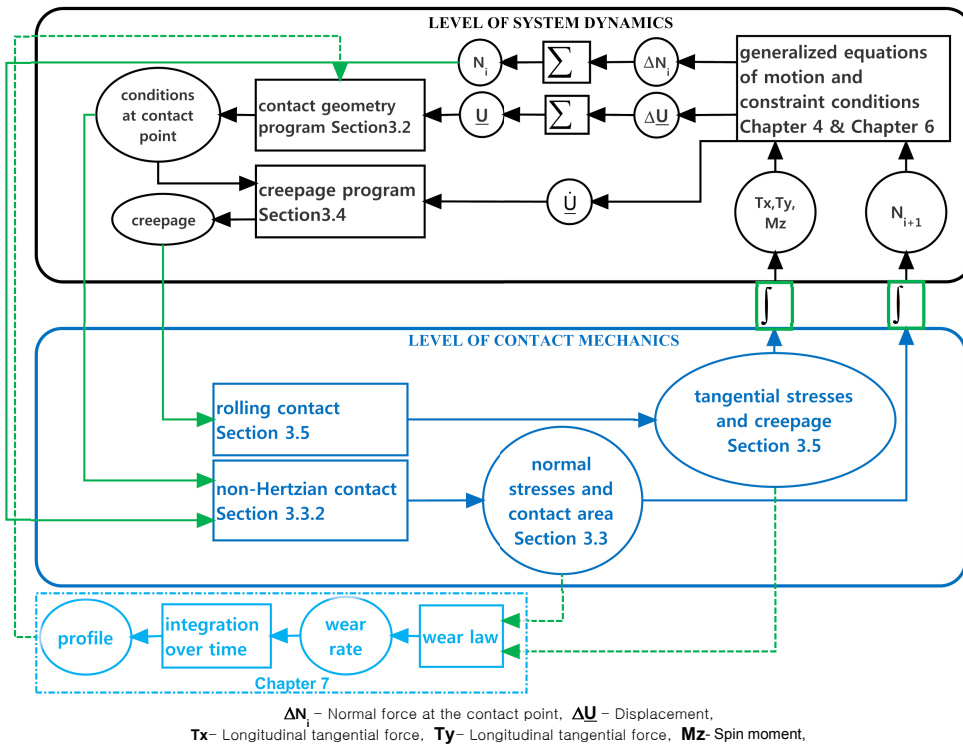
Figure 1.2: *Contact problem in the field of railway vehicle dynamics, adapted from [64].*

The content in the black block mainly relates to system dynamics corresponding to Chapter 4 and Chapter 6, in contrast, the content in the blue block mainly belongs to contact mechanics which are treated in Chapter 3 and Chapter 7. Chapter 3 focuses on the theoretical analysis and numerical modelling for the wheel-rail and wheel-roller contact, which paves the way for further study of wheel-rail contact at a system level in practical applications, such as the wear test addressed in Chapter 7.

CHAPTER *2*

LITERATURE REVIEW

2.1 Chapter summary

The application of roller rigs to railway engineering has a very long history, and it becomes more widespread and diverse in recent decades thanks to their high controllability and flexibility compared to the field test. The main objective of the roller rigs is to reduce time of new vehicle/component testing and to extend the range of possible tests in order to perform different studies without using a dedicated track [115]. The main interest of this thesis is the application of the roller rig to wheel-rail contact and vehicle dynamics studies. Therefore, a detailed survey on the development history of roller rigs is given in this chapter, serving as a theoretical background of this study, and it is followed by a summary of the state of the art in the filed.

2.2 Development history of roller rigs in railway application

Roller rigs were originally used for the investigation of the performance of steam locomotives over 100 years ago [115]. The first roller rig was built at full scale in 1904 at Swindon in the UK. This roller rig was also reproduced in the USA at the Purdue University for the Pennsylvania Railway.

Similar test rigs were probably used by Musashi to carry out model tests in 1935 in Japan as reported by Jaschinski in [47]. In 1957, the development of new bogies for the high-speed train on Shinkansen was performed at first with the aid of scaled roller rigs and finally with a full-scale roller rig using an eccentric roller to create a sinusoidal excitation built at the Railway Technical Research Institute (RTRI) in Japan [19, 75]. Around 1960, tests of bogies commenced on the full-scale roller rig with only two axles [115]. Then in 1989, simultaneously with the entry into service of the new high

speed trains, this roller rig was completed with two additional axles to allow tests on complete vehicles up to 500 km/h [80].

In 1959, the British Rail Research Centre built a two-axle roller rig in Derby, UK, then completed it with another two axles in 1971 [109]. This roller rig had the capacity to assess braking power, resonant vibration, and vehicle stability. Latterly, the roller rig was modified to a modal analysis test stand mainly used for the vibration analysis of vehicle suspension systems [115].

In 1964, a roller rig was built in Vitry, France by CAFL Company. It allows lateral and vertical motions of the roller on each axle simultaneously using simple hydraulic control methods. By using the roller rig, the vertical, lateral, and yaw vibration frequencies, amplitudes and resonance can be measured. In particular, the influence of the change of the vertical and lateral excitation forces due to the impart force on the vehicle running performance can be studied and the running safety and ride performance can also be investigated [115].

In 1967, a roller rig was built in Berlin, Germany. It allows evaluation of traction equipment, acceptance tests for vehicle springs, and assessment of braking systems [115].

In 1977, Bundesbahn built a four axles full-scale roller rig at Deutsche Bahn AG in Munich, Germany, in order to perform tests on vehicles and locomotives [32]. The rollers had four degrees of freedom including vertical, lateral, inclination, and rotation. The servohydraulic excitation control system was adopted for the roller rig and could accurately simulate track conditions for the dynamic simulation of a vehicle operating on tracks. The rig was mainly utilised for the measurement of the dynamic performance of vehicles and determination of the effects of vehicle modifications on the system performance. The Munich roller rig played a very important role in the development of the ICE high-speed trains. Due to considerable cost and a lack of capacity utilization this roller rig had to be closed in 2003. It was widely used in Europe to certify new vehicles for different railway administrations [115].

In 1978, a roller rig, called the roll dynamics unit, with vibrations applied through the wheels to simulate track conditions, began operation at Pueblo, Colorado, USA. The rig consists of two separate test stands, one for roller-based testing, and another used as a vibration stand. The rolling stand can be used for hunting stability and traction power simulation tests and the vibration stand used for studies of suspension system features, vehicle system natural frequencies, fatigue strength, and freight load reliability, etc. The rig was designed for speed of up to 480 km/h [115].

In 1988, NTSEL in Japan developed a full-scale bogie roller rig that can simulate curving condition [76]. The basic model of the roller rig had four rolling-rig units to simulate rails. Each rolling-rig unit had a pair of wheels for standard gauge (1435 mm gauge) track and narrow gauge (1067 mm gauge) track. In 1993, train driving controller and flying wheel were added to the original designed facility, to reinforce the traction and braking test functions. The test of regeneration brake of VVVF driving bogie was carried out. In order to deal with the experiment that involves high creep forces, the wheel-rig driving system including the driving shafts and gear boxes were reinforced in 2003. At the same time, a bogie-angle simulating function was added. The roller rig at NTSEL is shown in Figure 2.1 on the left side.

In 1992, a four-axle roller rig was completed at the Ansaldo Transport Research

Centre in Naples, Italy. The roller rig was designed to allow future upgrading to test six-axle vehicles and mainly used to test railway locomotives for traction simulation. Its rollers can only rotate about their axles to simulate running on a straight track. The maximum running speed is (22 t/axle, 1500 mm diameter rollers) 300 km/h [37].

Figure 2.1: *The roller rigs at NTSEL (left) [77] and SWJTU (right).*

In 1995, a four-axle roller rig was built at the State Key Laboratory of Traction Power in Southwest Jiaotong University (SWJTU), China. This roller rig was built for the optimum design and testing of railway vehicles. Each roller can vibrate in lateral and vertical directions. In 2002, two new sets of rollers were added, to form six axles, allowing locomotives to be tested on the rig. With the development of high-speed railway in China from 2004, the design speed of high-speed trains reached 380 km/h, while the design of the roller rig was modified, increasing the roller diameter from 1370 mm to 1800 mm and the axis traction to 2000 kW, and realising a new roller rig with speed up to 600 km/h in 2011. In China there are four roller rigs for whole vehicle tests and two rigs for bogie tests [38]. The roller rig at SWJTU is shown in Figure 2.1 on the right side.

In 2013, a new roller rig has been put into service for vehicles of up to six axles at Osmannoro CDS (Centro Dinamica Sperimentale) testing centre near Florence in Italy, owned by Italcertifer (ITCF), which is one of the Italian notified bodies for the certification of the railway rolling stock [38]. This rig can simulate degraded adhesion conditions to test rail vehicle response.

The roller rigs introduced above are some typical representatives in different eras in the development history of the roller rigs, and most of them are full-scale bogie or vehicle test rigs. This kind of roller rigs come closest to reality because full bogie or vehicle can be tested under conditions very close to a real track. However, the costs are very high and the wheel/rail contact parameters cannot be controlled accurately. Actually, the scaled roller rigs have contributed to the railway research together with the full-scale roller rigs, and the wheel/rail contact parameters can be controlled accurately in this case. But the major drawback of a scaled system is that it eliminates the ability to directly test standard components. For more details on the application of the scaled roller rigs to the railway research, the reader is referred to [3].

There is a relatively recent design of roller rig specially for a single wheelset test which now is a very popular type of rig for testing railway vehicle dynamics in the

laboratory. It is considered as the best way to test quickly new components of wheelset system and to perform stress and wear analysis without a proper track. That is why it is chosen as the main research subject in this work. To the best of the author's knowledge, four test rigs of this type are presently existing as mentioned in Chapter 1. More details are given in this section.

The RaSSP roller rig owned by Deutsche Bahn's Research & Technology Centre (FTZ) at Brandenburg-Kirchmöser in Germany was built in 1999, see Figure 1.1(right). The 36-tonne steel body of the test rig rests on a 200-tonne vibration pedestal. The roller rig consists of a roller with two wheels driven by a motor. A full-size wheelset is mounted on the top of the rollers having a diameter of 2100 mm with actual rail profiles and connected through primary suspensions to a transversal beam representing one half of the bogie frame. While the axis of the rail rollers is fixed in space, wheel contact forces, lateral displacement and the angle of attack of the wheelset are induced by a system of six hydraulic actuators, which rotates and displaces the wheelset along all three spatial axes [46]. It is primarily designed for testing rolling contact processes, and the unit allows full-size wheelsets to be subjected to stressing on a pair of rail rollers under reproducible dynamic contact conditions. The maximum running speed is continuously 300 km/h and briefly 330 km/h [100].

The BU300 roller rig owned by Lucchini RS at Lovere, Italy, has been in use since 2001, see Figure 1.1(left). It has similar configuration with RaSSP rig, but electric servomotors are used for yaw actuation instead of hydraulic actuators. In addition, the rollers bearing tow rail rings with real rail profiles have a diameter of 2000 mm. The maximum operating speed is 300 km/h [38].

The roller rig at KRRI in South Korea was opened to service in 2011 [1] and has a similar concept as the BU300 and the RaSSP rigs, particularly in terms of layout of the actuators used to apply the vertical and lateral loads. The yaw of the half bogie is in this case actuated using three hydraulic actuators. It is mainly used to the study of wheel-rail forces, wear and rolling contact fatigue, and wheelset derailment. The maximum testing speed of this roller rig is up to 320 km/h [38].

Figure 2.2: *The roller rig for tests on a single wheelset at CARS.*

The roller rig was newly built at CARS in China using the similar concept to the other three rigs described above. The diameter of the roller is 3000 mm and the designed testing speed is up to 500 km/h. Moreover, this roller rig allows adhesion tests

to be performed by introducing a single wheel unit driven by a motor, so that both traction and braking scenarios can be simulated on the rig [38], see Figure 2.2.

There is no doubt that the significant improvements in roller rigs have considerably increased their ability to replicate and study rail vehicle dynamics and wheel-rail contact, while further improvements are still highly desirable.

2.3   The application of roller rigs to rail vehicle dynamics

The roller rigs for railway dynamics application have been the subject of extensive research. One important paper by A. Jaschinski *et al.* [47] in 1999 described the details about the roller rig application to railway vehicle dynamics for both full-scale and scaled roller rigs. Different roller rig designs were presented and discussed along with their advantages and disadvantages. The paper also illustrates the use of roller rigs for testing and experimental purposes and for validation real railway vehicle dynamic simulations. In 2006, a comprehensive study on the application of roller rig in railway system especially for the full-scale vehicle roller rigs was performed by W. Zhang *et al.* [115]. Recently, a brief survey was made by S. Meymand *et al.* [79] in 2013 to highlight the advantages and disadvantages of using roller rigs for engineering issues of importance to the railway industry. In 2014, A. Facchinetti *et al.* [38] reviewed some typical roller rigs for rolling stock dynamic evaluation.

To sum up, the application of roller rigs to railway dynamics study primarily focuses on new concepts of innovative railway design or vehicle components optimization [32, 35, 41], the curving dynamics and performance [61, 115], and further investigations hardly performable on the track for safety reasons e.g. determination of critical speed [4, 34, 35, 43, 66, 106] and derailment [1, 20].

It should be mentioned that the curving test is generally difficult to be simulated on a roller rig because of the centrifugal forces and since the different distance to be travelled on inner and outer rail is neglected by most roller rigs. Therefore, this study is limited in the literature [61, 115], especially for a single wheelset roller rig [72]. In order to fill this gap, a detailed discussion about the curving test on the full-scale roller rig for a single wheelset test will be given in Chapter 6.

2.4   The application of roller rigs to wheel-rail contact

The roller rigs for wheel-rail contact study are generally in the form of disc-on-disc, wheel-on-roller and wheelset-on-rollers rather than vehicle-on-rollers setup so as to fully control the wheel-rail contact parameters under various conditions.

Many rigs have been built to deepen the understanding of physics behind the contact mechanics at the wheel-rail interface [76, 78, 90, 99]. In more detail, the purpose of the test includes but is not limited to the study of adhesion and creep characteristics between the wheel and rail [8, 18, 78, 90, 105, 114], validation or improvement of the existing contact theories [8, 90], and investigation of the surface damage mechanism of the wheel and rail, e.g. wear , rolling contact fatigue (RCF) [21, 30, 39, 65, 99], and rail corrugation [74]. More details about wear tests on a roller rig will be provided in Chapter 7.

2.5 Roller rig modelling and simulation

Numerical modelling and simulation of the roller rig is useful in the design of such rig, for guiding the test and for post-processing after test on the rig. A variety of mathematical models have been developed for different purposes.

R. Dukkipati [33] derived the expressions of the creepages and the four-degrees-of-freedom equations of motion for a railway wheelset on a roller rig to help the design of a roller rig in the USA. S. Bruni *et al.* [23] developed a detailed mathematical model including control unit for a full-scale roller rig in Italy, and the validation of the model is achieved by the comparison of testing results. For the same roller rig, F. Braghin *et al.* [20] presented the results of experimental and numerical investigations on a derailment test. S. Iwnicki *et al.* [45] developed a numerical model in MATLAB for a scaled roller rig originally at Manchester Metropolitan University (MMU) in the UK. For the same roller rig, a comprehensive study was performed afterwards on the inherent errors of the scaled roller rig with the help of numerical simulations [2, 110]. N. Bosso *et al.* in paper [16] simulated a scaled roller rig in ADAMS/Rail to compare the results obtained by using different scaling techniques and to describe the behaviour of a vehicle on the roller rig, then the dynamic behaviour of a railway wheelset on a roller rig versus tangent track was investigated with the help of the numerical simulation in [17]. Recently, they designed an approach for the real-time simulation for a scaled test rig based on a decomposition of the mechatronic system into groups with elements [19]. A. Schmid [92] developed a numerical model of the full-scale roller rig at DB in SIMPACK for excitation data generation. F. Cheli *et al.* [26] developed a numerical model of a full-scale locomotive roller rig system (including the locomotive, the roller rig and the corresponding control systems) to perform parametric analysis and to investigate the influence of the roller rig dynamics on the test rig behaviour in a design stage. Recently, B. Allotta *et al.* [5] developed a Hardware-In-the-Loop (HIL) railway roller rig model for the traction and braking testing activities under degraded adhesion conditions. J. Kalivoda *et al.* [54] developed a mechatronic model via co-simulation between SIMPACK and SIMULINK to verify and demonstrate the possibilities of the active wheelset control on a scaled roller rig at Czech Technical University in Prague, Czech Republic.

The work mentioned above mainly concentrates on the simulation of the dynamic characteristics of the roller rig system, while few references are available on the contact study in the wheel-roller interface. A. Keylin *et al.* [58] derived explicit analytical expressions for comparing contact patch dimensions and Kalker's coefficients for a wheel moving on a roller and on a tangent track, based on Hertz and Kalker's linear theory. M. Taheri *et al.* [98] developed a model for a single wheelset coupled to a roller rig in SIMPACK to compare the contact patch formed in wheel-rail and wheel-roller interfaces under the assumptions of the Hertzian theory. The non-Hertz contact modelling of the wheel-roller contact and the modelling of a roller rig system will be discussed in detail in Chapter 3 and Chapter 4, respectively.

CHAPTER *3*

WHEEL-RAIL/ROLLER CONTACT ANALYSIS

3.1 Chapter summary

The contact between wheel and rail is one of the most important features of the railway system, and this contact pair has attracted great attention since the advent of railway engineering. Unfortunately, the problems involved in the wheel-rail contact interface have not been completely understood due to the complexity of the problem. Many attempts have been made from both theoretical and experimental points of view. Moreover, field experiments on wheel-rail contact mechanics and dynamics are often challenging due to the difficulties in adequately controlling the test conditions [58]. Roller rigs are a good alternative in this case, thanks to their high controllability and flexibility and have been used as experimental tools in railway engineering over a long time. However, the roller rig test will never completely replace the field test due to inherent differences caused by the replacement of the rails by rollers in a roller rig system. Therefore, it is very important to know the differences between these two systems and the corresponding causes, in order to efficiently perform wheel-rail contact study on a roller rig, to correctly interpret the test results and to compensate for deviations between the roller rig and a real track. A novel non-Hertzian method is proposed for dealing with both wheel-rail and wheel-roller contact problems considering the effect of the yaw angle based on a detailed analysis of the contact problem in the wheel-rail system.

3.2 General calculation procedure for contact problem

From a mathematical point of view, the contact problem can be solved for both wheel-rail and wheel-roller contact according to the following four steps [19, 93]. The first step is to solve the geometrical problem, in which the locations of the contact points on the contacting bodies are determined. This is followed by solving the normal contact

problem, in which the shape and size of the contact patch formed in the contact interface due to body deformation and the normal pressure distribution over the contact patch are determined. The third step is to deal with the kinematic problem, in which normalized kinematic quantities, the so-called creepages, are determined. These creepages measure the relative velocities between the contacting bodies at the contact points. In the final step, the tangential problem is solved. This step concerns the prediction of tangential stresses at the contact interface which are generated by friction and creepages within the contact zone. All these steps need to be dealt with differently for the case of wheel-roller contact compared to the wheel-rail case, as described in this chapter.

3.3 Contact geometry

Contact geometry analysis deals with the contact searching problem between the contacting bodies. The contact positions depend on the dynamic conditions as well as material properties of the contact pair. The problem can be simplified as rigid contact detection with geometric constraints or more complicated elastic contact detection. There are many approaches for the detection of the contact points in the wheel-rail system as documented in [93]. Most of the approaches available in the literature assume that the yaw angle of the wheelset with respect to the track is very small and negligible when solving the geometric contact problem so as to form the so-called bi-dimensional method [87]. This assumption largely simplifies the calculation, leading to fast solutions that can be implemented in rail vehicle online dynamic simulations. Nevertheless, when a train negotiates curves with very small radii, the yaw angle of the wheelset relative to the track also known as the wheelset's angle of attack, might be large and therefore the bi-dimensional method is no longer valid. The three-dimensional method has been developed to deal with these situations [6, 20, 59, 84, 91]. The effect of the yaw angle of the wheelset on the contact position is shown in Figure 3.1 generated by the so-called apparent profile method [59, 84] where the contact lines of wheel are the visible profiles of the yawed wheel as seen along the rail, and the contact line on rail coincides with the rail profile.
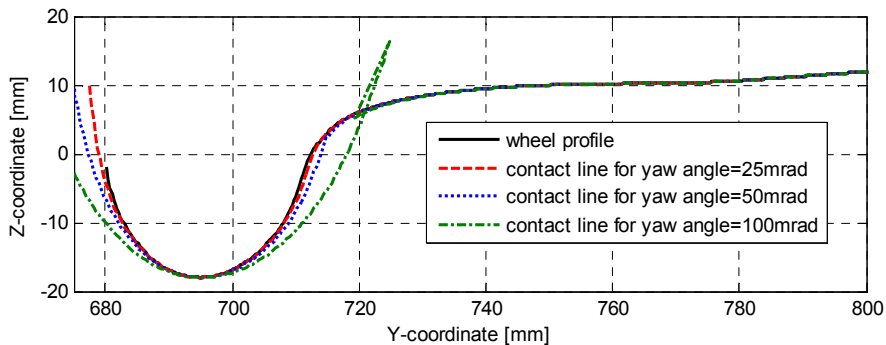
Figure 3.1: *Effect of the yaw angle on the contact position, adapted from [84].*

The replacement of the rail by the roller makes the geometric contact problem more complicated, which means some traditional approaches of contact geometry analysis of wheel-rail contact may not be applicable any more to the wheel-roller contact condition.

As stated in [113], three-dimensional wheel-rail contact problem on the tangent track can be simplified by projecting the yawed wheel profile onto the rail cross-section plane then calculated with traditional bi-dimensional methods, which is not the case for the wheel-roller contact where the profile of the rollers are varying in both longitudinal and vertical directions. To deal with this problem, a method specific to the wheel-roller contact system is needed. The existing approaches available in the literature can be found in [112, 113, 115].
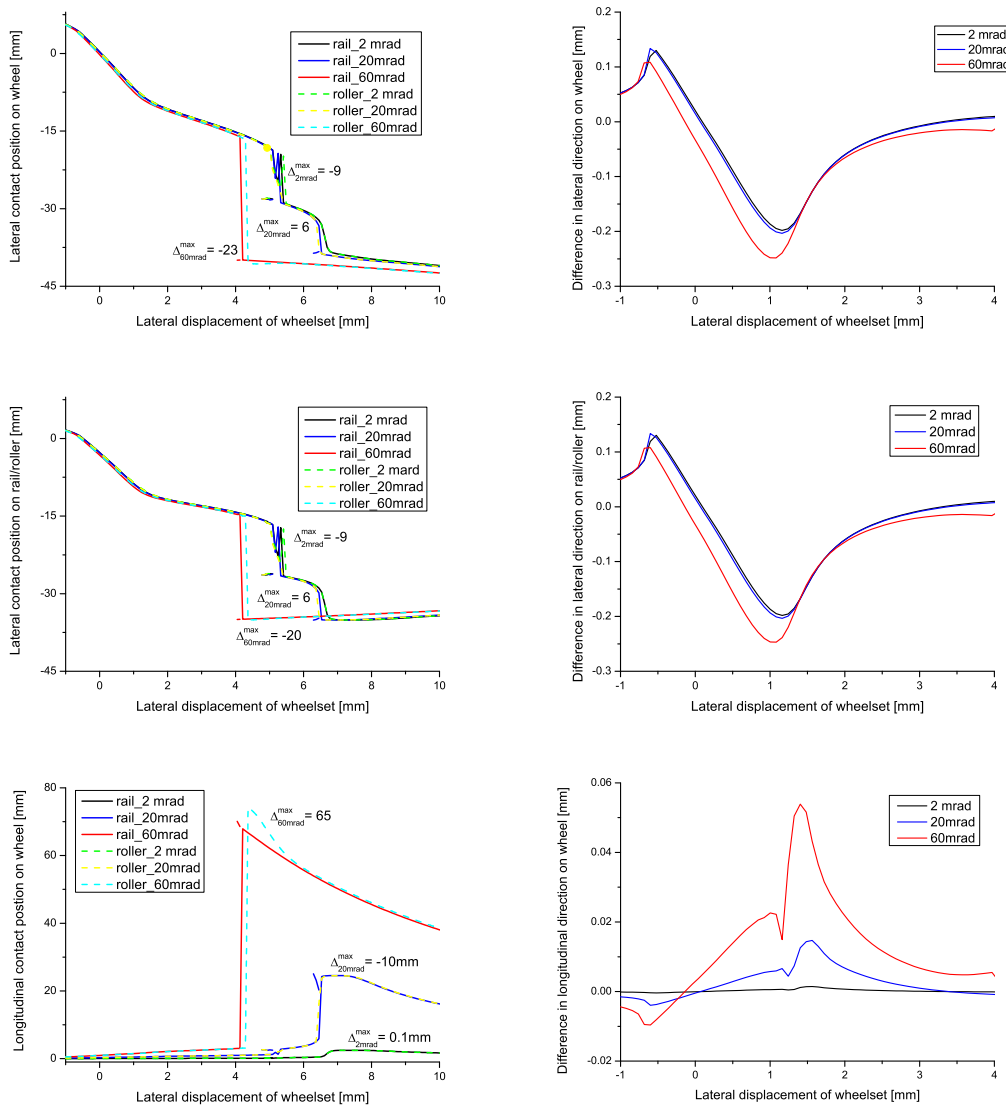
Figure 3.2: *Comparisons of geometric contact characteristics between the wheel-rail and wheel-roller contact.*

It is clear that the geometric contact condition between the wheel-rail and wheel-roller contact pairs is the same for zero yaw angle conditions assuming the contacting bodies to be rigid. There is a rich body of literature on comparisons of the geome-

try contact relationship between the wheel-rail and wheel-roller contact pairs, for instance [19, 113, 115]. Therefore, no further discussion is needed here, but a set of typical case studies are shown in Figure 3.2 for the completeness of this chapter. The comparisons were made with various magnitudes (2, 20, 60 mrad) of the yaw angle of the wheelset for the wheel-rail and wheel-roller contact cases. The profile combination is new S1002/UIC60 with 1:20 rail inclination, the radius of the roller is set to 1 m in the simulation. Figure 3.2 shows the comparison of geometric contact characteristics for the right-hand side contact pair of the wheel-rail and wheel-roller systems, and the differences are calculated by subtracting the quantities of the wheel-roller contact case from that of the wheel-rail contact case.

As can be seen from Figure 3.2 that the variations of contact geometry relationship in terms of the lateral and longitudinal contact positions on the wheel and lateral contact position on the rail/roller are similar when the lateral displacement of the wheelset is less than 4 mm. In presence of a small yaw angle of the wheelset, the flange contact occurs when the wheelset displaces approximately 5 mm in lateral direction, while it takes place at approximately 4 mm in case of a large yaw angle (60 mrad in this case).

It can also be observed that the contact positions detected at the wheel-rail and wheel-roller interfaces are different even though the wheelset has the same yaw angle (non-zero) and the same lateral displacement due to the finite radius of the roller. It should be also noted that 60 mrad is a quite large yaw angle for the wheelset and that smaller differences are found for smaller yaw angles. Obviously, the differences can be decreased by increasing the radius of the roller, but the dimension of the roller is limited in practice considering the increased cost and difficulties related with manufacturing and installation of the rig.

The contact points detected from the contact geometry analysis in this section are the inputs of the local contact analysis to be done in the following sections. As an external load is applied on each body of contact, the two contacting bodies will deform at the contact point to form a contact area referred to as a contact patch. The forces generated at the contact patch can be divided into compressive force in the direction normal to the interface, and frictional force in the direction tangent to the interface. Fortunately, these two components can be treated separately for quasi-identical contacting bodies i.e. the same elastic material properties of shear modulus and Poisson's ratio, and the wheel-rail and wheel-roller contact are generally assumed to be the case.

3.4 Normal contact

In this section, a brief review of the commonly used methods for solving the normal contact problem in the wheel-rail system is given first. It is followed by proposing a novel model for dealing with non-Hertzian contact condition in the wheel-rail and wheel-roller systems based on the well-known Kik-Piotrowski model [60].

3.4.1 Review of methods for solving the wheel-rail normal problem

One of the first studies of wheel-rail normal contact was carried out by F. Redtenbacher in 1855 [89]. In 1882, Heinrich Hertz [42] presented a contact theory that accounts for the shape of the surfaces in the neighbourhood of the contact area. Although the Hertzian theory relies on a number of rather restrictive assumptions, it is still widely

used in studying wheel-rail contact mechanics and dynamics and serves as a foundation for many tangential contact theories. The assumptions made in the Hertzian theory can be summarized as follows [52, 62]:

- complete linearity, i.e. linear kinematic equations and linear-elastic material law (additionally the material is isotropic and homogeneous);

- the surfaces are frictionless;

- both bodies are considered as half-spaces and

- the surfaces of the two bodies are regarded as second-order polynomials.

However, the shape and size of the contact patch obtained from the Hertzian theory are often a poor representation of the true contact patch, primarily due to non-constant surface curvatures [57, 62]. More accurate contact model is required in these cases, especially for the simulation of wear, rolling contact fatigue (RCF) and rail corrugation etc., in the wheel-rail system. For this reason, a number of non-Hertzian and semi-Hertzian normal contact theories have been proposed to improve the accuracy of the solution. Some of these theories are modifications of the Hertzian theory, and some are based on different principles.

The most elaborate contact model to date can be established by finite element method [29, 102] which is quite complicated and time consuming. The same problem can be dealt with using the boundary element method as done, e.g. by Prof. Kalker's algorithm CONTACT [57] and by the model proposed by Knothe and Le The [63]. The so-called approximate contact methods represent a trade-off between efficiency and accuracy in the solution of the normal problem and therefore are generally considered as best suited for both local contact analysis and on-line dynamics simulation. Methods of this type include those based on the approximation of a non-elliptic contact zone by a set of ellipses developed by Pascal and Sauvage, the well-known method based on the virtual penetration of contacting bodies proposed by Kik and Piotrowski [60, 83, 84], a similar concept adopted by Ayasse and Chollet [13], and Linder's model [71] etc. Some interesting surveys of the existing approximate methods and the comparisons among them can be found in [83, 95, 96].

3.4.2 The Extended Kik-Piotrowski model

The Kik-Piotrowski method is a fast and non-iterative method for solving normal contact problem, which will be abbreviated as KP method in this thesis. An outline of this method will be given in this section. For more details, the reader is referred to [60, 83, 84]. The idea of the method is presented in Figure 3.3. When the undeformed surfaces of the wheel and rail, touching at the initial point of contact O, also called geometrical point of contact which is determined from geometric contact analysis, are shifted towards each other by a distance δ called the penetration, they penetrate and intersect on a closed line, whose projection on Oxy plane is called the interpenetration region. In reality, the bodies cannot penetrate, deflections occur and the contact zone comes into being. On the basis of some similarities of the shapes of the contact zone and interpenetration region, the contact zone is determined by scaling the interpenetration approach $\delta_0 = \epsilon\delta$ with a scaling factor $\epsilon = 0.55$, then the resulting interpenetration region is taken as the approximation of the real contact zone.

15
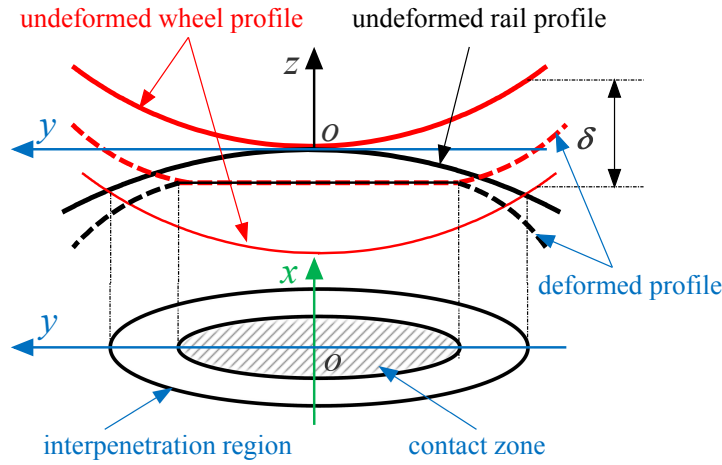
Figure 3.3: *The Kik-Piotrowski method for contact estimation, adapt from [60].*

In common of the widely used approximate methods, the contact patch is always assumed to be symmetric about its lateral axis in contact plane. This is not true in presence of a non-negligible yaw angle of the wheelset against the track. Past study has been done to account for the effect of the yaw angle on wear indexes and derailment risk by applying elastic three-dimensional contact point searching algorithm [91] which produces more realistic results compared with the traditional methods used in rail vehicle dynamics simulation. Actually, the yaw angle of the wheelset affects not only the contact position but also the characteristics of the contact patch as presented in [102] by using the finite element method. However, this significant effect is rare to be considered in the commonly used contact models. To fill this gap, a new non-Hertzian contact model is proposed as an extension of the KP model named Extend Kik-Piotrowski (EKP) model in this thesis which is capable of taking into account the influence of the yaw angle and the non-constant surface curvatures of contact bodies on the normal contact solution in the wheel-rail system.

Two coordinate systems are defined in the contact patch. The first is $Oxyz$ representing the general contact reference system in which the x-axis points along the rolling direction of the wheelset, the z-axis is normal to the contacting surfaces, and the y-axis is mutually perpendicular. The second is $Ox_0y_0z_0$ indicating the state of $Oxyz$ when the yaw angle of the wheelset is zero, which means the x_0-axis is always along the rail in longitudinal direction. It is clear that the contact frame $Oxyz$ can be obtained from $Ox_0y_0z_0$ by performing a rotation around the z_0-axis by an angle ψ representing the yaw angle of the wheelset.

The cross-sections of the contacting surfaces by xz plane are named rolling sections, and by yz plane called lateral sections. Therefore, the wheel and rail rolling sections are $z_{xz}^w(x)$ and $z_{xz}^r(x)$ and the lateral sections are $z_{yz}^w(y)$ and $z_{yz}^r(y)$, respectively. In addition, $z_{y_0z_0}^w(y_0)$ and $z_{y_0z_0}^r(y_0)$ represent the wheel and rail profiles in the conventional sense according to the definition. The separation function in contact reference system can be expressed as follows:

$$z(x, y) = z^w(x, y) + z^r(x, y) \tag{3.1}$$

The next step is to determine the virtual interpenetration region by penetrating the

wheel and rail surfaces to the depth δ_0 called virtual interpenetration. The resulting interpenetration region is taken as the area of contact. To this end, the interpenetration function of profiles is defined in the KP by the following formula:

$$g_{yz}(y) = \begin{cases} \delta_0 - f(y) & \text{if } f(y) \leq \delta_0 \\ 0 & \text{else.} \end{cases} \tag{3.2}$$

where $f(y) = z_{yz}^w(y) + z_{yz}^r(y)$ is the distance function at the undeformed state.

Then the contact width can be determined by solving Equation 3.2. It should be mentioned that the contact width is corrected by adjusting the interpenetration function in a later version of the KP method, cf. [84].

The leading and trailing edges of the contact patch can be determined by Equation 3.3 in the KP method based on the assumption that the wheel-rail contact problem is stated in terms of two bodies of revolution with their axes laying in the same plane. The same assumption was made by Linder [71].

$$x_{xz}^l(y) = -x_{xz}^r(y) \approx \sqrt{2R_w g_{yz}(y)} \tag{3.3}$$

where the subscripts xz represents the function defined in xz plane, the subscripts l and t indicate the terms associated with the leading and trailing edges of the contact patch, respectively, and R_w is the rolling radius of the wheel.

According to Equation 3.3, the contact area is always symmetric about the y-axis in the contact reference frame. However, this assumption is violated in case of a yaw angle formed between the wheel and rail/roller considering the radius of curvature of the rail/roller rolling section $z_{xz}^r(x)$ is no longer constant, which results in an asymmetric contact area as illustrated in Figure 3.4 for the wheel-rail case.
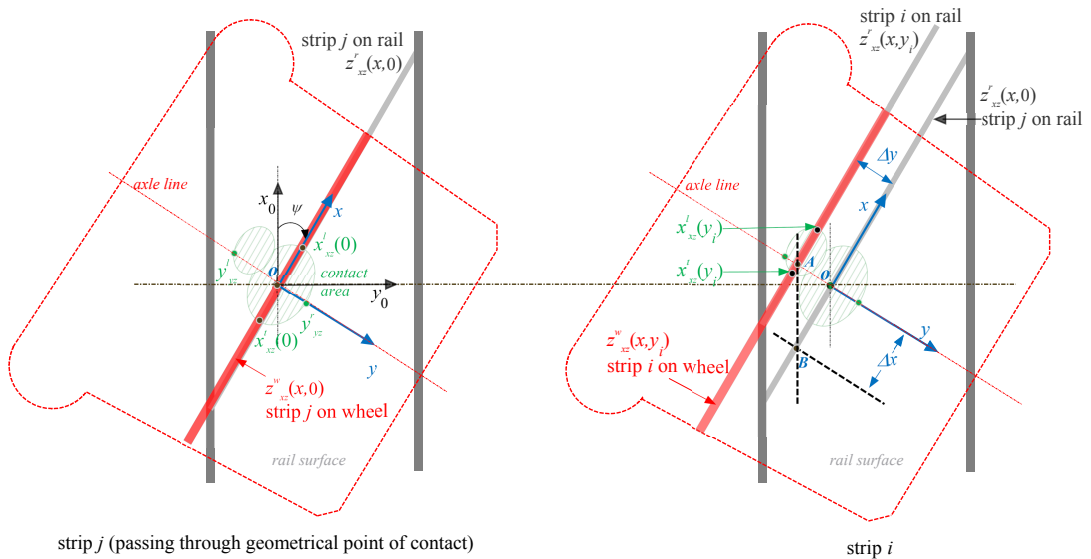
Figure 3.4: *Effect of the yaw angle ψ on the contact patch for the wheel-rail case (top view, right wheel).*

To determine the contact zone in presence of a non-zero yaw angle, the rolling and lateral sections are required. It is clear that the rolling section of the wheel is a circle

with a radius of R_{cw} passing through the contact point and independent of the yaw angle as express by Equation 3.4.

$$z_{xz}^{w}(x) = R_{cw} - \sqrt{R_{cw}^2 - x^2} \tag{3.4}$$

where the radius R_{cw} is assumed to be constant here though it may vary slightly over the contact patch.

The rolling section of the rail is a straight line, and it is a circle for the roller, when the yaw angle of the wheelset is zero. For non-zero yaw angle conditions ($\psi \neq 0$), it can be obtained from the following equation with reference to Figure 3.4.

$$z_{xz}^{r}(x) = z_{y_0 z_0}^{r} \left(\frac{y_0}{\sin \psi} \right) - h_{xz} \tag{3.5}$$

with

$$h_{xz} = R_{cr} - \sqrt{R_{cr} - (\Delta x \cos \psi)^2} \tag{3.6}$$

where h_{xz} is the arc height of the roller corresponding to the chord $\Delta x \cos \psi$ as shown in Figure 3.5, $\Delta x = \Delta y \cot \psi$, Δy being the distance from the origin in y direction, and $h_{xz} = 0$ for the wheel-rail case.

side view of roller
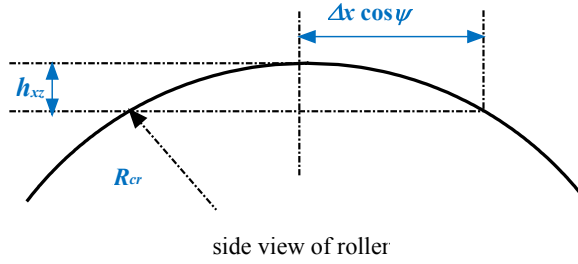
Figure 3.5: *Illustration of the arc height of the roller.*

It should be noted that the rail lateral section $z_{yz}^{r}(y)$ varies with the yaw angle, while the wheel lateral section $z_{yz}^{w}(y)$ remains the same as its profile $z_{y_0 z_0}^{w}(y_0)$. They can be expressed as follows:

$$\begin{cases} z_{yz}^{w}(y) = z_{y_0 z_0}^{w}(y_0) \\ z_{yz}^{r}(y) = z_{y_0 z_0}^{r} \left(\dfrac{y_0}{\cos \psi} \right) - h_{yz} \end{cases} \tag{3.7}$$

where $h_{yz} = R_{cr} - \sqrt{R_{cr} - (\Delta y \sin \psi)^2}$ is the arc height of the roller corresponding to the chord $\Delta y \sin \psi$, R_{cr} being the rolling radius of the roller at the contact point, and $h_{yz} = 0$ for the wheel-rail case.

Substituting the lateral section functions derived above into Equation 3.2, the width of the contact patch can be determined. The next task is to determine the contact boundary in rolling direction. To this end, the contact patch is partitioned into strips paralleling with the x-axis in contact plane, and O is the geometrical point of contact determined in Section 3.3. Hence, the section functions are converted to discrete forms by strips $y_i (i = 1...n)$, as illustrated in Figure 3.4 where the two figures show two strips

(j and i) in the same contact patch of the same wheel. The rail rolling section strip $z^r_{xz}(x, y_i)$ corresponding to the rolling section of the wheel at the i-th strip in contact patch can be obtained by shifting the rail rolling section strip $z^r_{xz}(x, 0)$ (denoted by j-th strip in Figure 3.4) that passes through the geometrical point of contact along the x-axis. Because the curvature of the rail rolling section at the contact position A corresponding to i-th strip is identical to that of the rolling section at position B which is located in the rail rolling section strip $z^r_{xz}(x, 0)$. This means the contact condition between the wheel rolling section strip $z^w_{xz}(x, y_i)$ and the rail rolling section strip $z^r_{xz}(x, y_i)$ at position A is equivalent to the contact condition between the wheel strip $z^w_{xz}(x, y_i)$ and the rail strip $z^r_{xz}(x, 0)$ at position B. This relation can be expressed as follows:

$$z^r_{xz}(x, y_i) = z^r_{xz}(x - \Delta x_i, 0) \tag{3.8}$$

where $\Delta x_i = y_i \cot \psi$ is the shifting distance from j-th strip to i-th strip in x direction.

Equation 3.8 makes it possible to determine the so-called undeformed distance surface $H(x, y) = z(x, y) + \delta_0$ by simply solving a set of equations without the need of three-dimensional rolling surfaces of the wheel and rail. Therefore, the computing time can be reduced considerably. The undeformed distance surface is an important input for surface-based contact calculation methods, for instance the software CONTACT [103].

In the case of wheel-roller contact, the roller rolling section strip $z^r_{xz}(x, y_i)$ corresponding to the rolling section of the wheel at the i-th strip in contact patch can be obtained by rotating instead of shifting (for the wheel-rail case) the rolling section strip $z^r_{xz}(x, 0)$ by an angle γ. This relation can be expressed by Equation 3.9.

$$[x, z^r_{xz}(x, y_i) + R_{cr}] = [x, z^r_{xz}(x, 0) + R_{cr}] \begin{bmatrix} \cos \gamma & \sin \gamma \\ -\sin \gamma & \cos \gamma \end{bmatrix} \tag{3.9}$$

where $\gamma = \arcsin \frac{\Delta x_i}{R_{cr}}$ is the rotating angle.

The length of each strip is determined by solving Equation 3.10 instead of Equation 3.3 to include the yaw effect.

$$z^w_{xz}(x, y_i) - z^r_{xz}(x, y_i) = g_{yz}(y_i) \tag{3.10}$$

Equation 3.10 produces two solutions in which the larger one corresponds to the leading edge. All the extremities of the strips together comprise the boundary of the contact zone. Figure 3.6 illustrates the determination of the contact length where the figures (b) and (c) correspond to the two strips shown in Figure 3.4.
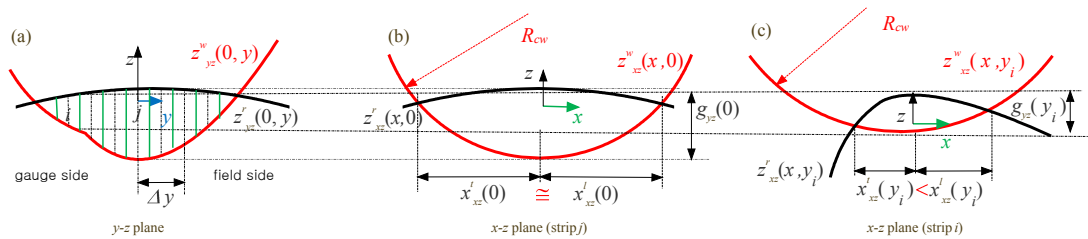
Figure 3.6: *Illustration of the determination of the contact length.*

In order to estimate the normal pressure distribution over the contact patch, the strips in contact zone are divided into 50×50 elements. The centre of each element is denoted

by (x_j, y_i). For each element the pressure is assumed to be constant and determined by the following formula:

$$p(x_j, y_i) = \frac{p_0}{x_{xz}^l(0)} \sqrt{(x_{xz}^l(y_i))^2 - (x_j(y_i))^2} \tag{3.11}$$

where p_0 is the maximum pressure over the contact patch, $x_j(y_i)$ is the coordinate along x-axis of the j-th element in the i-th strip. More details about the determination of p and p_0 can be found in [60, 83, 84].

Past studies [95, 96] have shown that the contact estimated by the KP method considerably deviates from CONTACT's result in terms of the contact shape and pressure distribution when the contact zone spreads into a region with non-constant surface curvatures, which is a condition in which the Hertzian theory is not valid [111]. The main reason for this discrepancy in contact shape mentioned above is due to the fact that a single constant approach scaling factor is used in the KP model, whereas the difference in pressure is due to the assumption made in the KP model that the maximum pressure in each strip is similar to the length of that strip [95]. It implies that the dependency of the maximum pressure on other parameters e.g. the variation of the surface curvature is neglected. However, the comparison between the results from CONTACT and the KP method shows that the KP model provides satisfactory results in the vicinity of the geometrical point of contact [60, 84, 95]. Therefore, the KP model could be improved by introducing the influence of varying curvatures of the contacting bodies for the multi-patch or joined-patch contact conditions.

To this end, the KP model is corrected by taking the geometrical point of contact position as the reference in the EKP model. Firstly, the contact boundary obtained from Equation 3.10 is corrected according to Equation 3.12.

$$\begin{cases} x_{xz}^l(y_i) = \frac{k_1 - 1 + k_2(y_i)}{k_1} \left(x_0^l(y_i) - x_c(y_i) \right) + x_c(y_i) \\ x_{xz}^t(y_i) = \frac{k_1 - 1 + k_2(y_i)}{k_1} \left(x_0^t(y_i) - x_c(y_i) \right) + x_c(y_i) \end{cases} \tag{3.12}$$

where $x_0^{l,t}(y_i)$ represents the boundary solution obtained from Equation 3.10, $x_c(y_i)$ is the centre coordinate of the i-th strip along x-axis, k_1 and k_2 are correction coefficients, k_1 being a non-zero constant and k_2 being a function of the strip position at the contact patch. It should be noted that Equation 3.12 is equivalent to the solution of Equation 3.10 when $k_2 = 1$ and $x_c(y_i) = 0$ corresponding to zero yaw angle contact condition.

Then Equation 3.11 is corrected to include the effect of yaw angle and the variation of curvature at contact region as expressed by Equation 3.13.

$$p(x_j, y_i) = \begin{cases} \frac{p_0(k_1 - 1 + k_2(y_i))}{k_1(x_l(0) - x_c(0))} \sqrt{(x_{xz}^l(y_i) - x_c(y_i))^2 - (x_j(y_i) - x_c(y_i))^2}, \text{if } x_j(y_i) \geq 0 \\ \frac{p_0(k_1 - 1 + k_2(y_i))}{k_1(x_t(0) - x_c(0))} \sqrt{(x_{xz}^t(y_i) - x_c(y_i))^2 - (x_j(y_i) - x_c(y_i))^2}, \text{if } x_j(y_i) < 0 \end{cases} \tag{3.13}$$

where $x_{l,t}(0)$ and $x_c(0)$ stand for the leading and trailing edges and the centre coordinate of the strip including the geometrical point of contact. Equation 3.13 has the same form as Equation 3.11 if $k_2 = 1$ and $x_c(y) = 0$.

It should be pointed out that the corrections are applied only for the contact conditions where the interpenetration function $g_{yz}(y)$ determined by the KP method possesses negative curvatures, which implies that the contact zone includes jointed contact

patch or multiple contact patches, to account for the influence of the curvature variation of the contact bodies on the contact boundary and pressure.

As mentioned above, the approach scaling factor is treated as a constant of 0.55 in the KP model for the determination of the interpenetration function $g_{yz}(y)$ according to Equation 3.2. Consequently, the contact width, which is the range of y coordinate values considering $y > 0$, is obtained. However, the contact width may be under estimated in this way under some certain circumstances, for instance the situation shown in Figure 3.7.
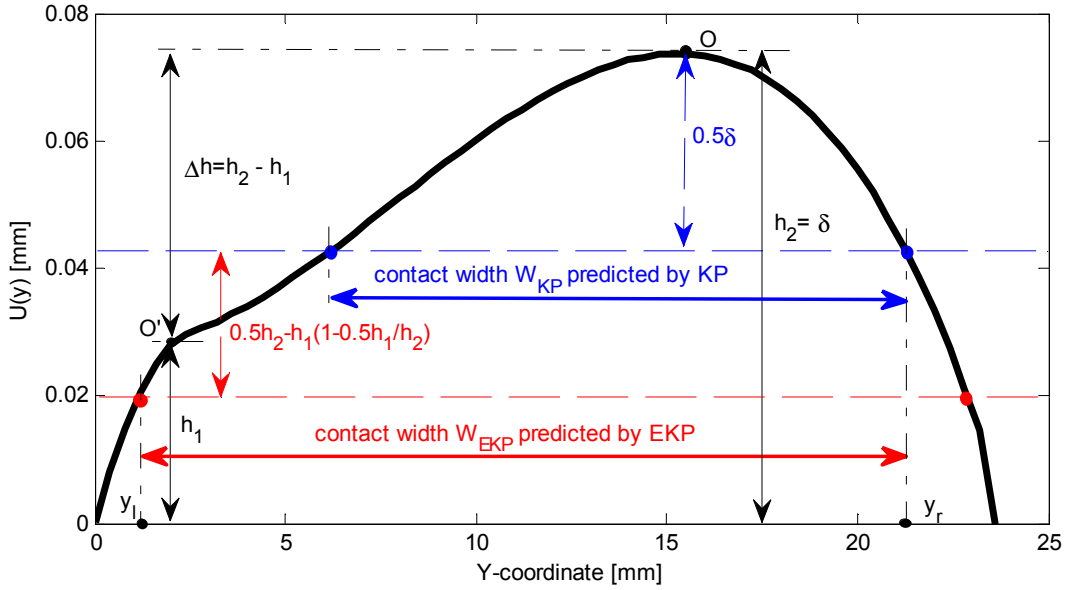
Figure 3.7: *Illustration of the determination of the contact width.*

With reference to Figure 3.7, the predicted contact width is W_{KP} according to the KP method. However, the Greenwood and Williamson model [40] for dealing with multi-contact problem shows that the heights of the asperities and the radii of curvature play primary role for contact estimation. It means some essential information related to the first height in Figure 3.7 may be missing when the KP method is applied. To deal with this special situation, the following correction is made for the contact width prediction in the EKP model.

In order to check if the potential contact zone is a jointed patch or multiple contact patches, the potential interpenetration $U(y)$ obtained by setting $\delta_0 = \delta$ in Equation 3.2 is compressed in lateral coordinate so as to easily capture the variation of its curvature. The compressed $U(y)$ is denoted by U_c and its curvature is denoted by C_u .

$$U_c(y) = U(\alpha y) \tag{3.14}$$

where $\alpha < 1$ is the compression coefficient, and it is found that 0.01 is a suitable value.

Then the interpenetration function $g_{yz}(y)$ and the contact width can be determined as follows:

Step 1, if C_u has negative values, which means there is more than one height in function $U(y)$, denoted by h_1 and h_2, respectively, from left to right as shown in Figure 3.7, go to Step 2. Otherwise, the KP is used with $\epsilon = 0.5$, instead of 0.55 that is the value applied in the original KP.

Step 2, if the difference of the two heights denoted by $\Delta h = |h_1 - h_2|$ is less than 0.5δ, the KP is applied with $\epsilon = 0.5$, else go to next step.

Step 3, the two extremities (y_l and y_r) of the contact width are obtained solving the following equations. The predicted contact width by the EKP is denoted by W_{EKP} in Figure 3.7.

$$\text{if } h_1 < h_2 \begin{cases} U(y_l) = h_2 - h_1(1 - \frac{h_1}{h_2}) \\ U(y_r) = 0.5h_2 \end{cases} \text{else} \begin{cases} U(y_l) = 0.5h_2 \\ U(y_r) = h_2 - h_1(1 - \frac{h_1}{h_2}) \end{cases} \tag{3.15}$$

Then the updated interpenetration function is obtained in the form of Equation 3.16 instead of Equation 3.2.

$$g_{yz}(y) = \begin{cases} 0.5\delta \frac{U(y)}{\max(U(y))} & \text{if } y_l < y < y_r \\ 0 & \text{else} \end{cases} \tag{3.16}$$

As with function $U(y)$, the interpenetration function is compressed in the same way, and the compressed interpenetration function is denoted by $g_c(y)$.

$$g_c(y) = g_{yz}(\alpha y) \tag{3.17}$$

In order to define the correction coefficients, the curvature of the interpenetration function is normalized with respect to its value at the reference point as follows:

$$C_n(y) = \frac{C(g_c(y))}{C(g_c(0))} \tag{3.18}$$

where $C(\cdot)$ defines curvature function, thereby $C(g_c(0))$ represents the curvature of the compressed interpenetration function at the reference point which is the geometrical point of contact.

The minimum value of Equation 3.18 is denoted by $C_n(y_m) = \min(C_n(y))$. The corresponding strip y_m is chosen to determine the correction coefficient k_1. Assuming that the length of this strip is proportional to its corresponding interpenetration approach, the following relationship holds according to Equation 3.12.

$$\frac{k_1 - 1 + C_n(y_m)}{k_1 - 1 + k_2(0)} = \frac{g_{yz}(y_m)}{g_{yz}(0)} \tag{3.19}$$

where $g_{yz}(0) = 1$ and $k_2(0) = 1$ represent the values obtained at the reference point, more detailed definition of k_2 will be given later.

Hence, the correction coefficient k_1 can be determined as follows:

$$k_1 = \frac{g_{yz}(0)(1 - C_n(y_m))}{g_{yz}(0) - g_{yz}(y_m)} \tag{3.20}$$

In order to define the correction coefficient k_2, an intermediate function $R(y)$ is introduced according to Equation 3.21.

$$R(y) = \begin{cases} C_n^{0.08}(y) & \text{if } C_n(y) > 0 \\ 0 & \text{else} \end{cases} \tag{3.21}$$

As mentioned above, these corrections are only applied to the contact conditions where the interpenetration function $g_{yz}(y)$ possesses negative curvatures, which means function $R(y)$ has more than one peak. The first peak is denoted by $R(y_p)$ and the second by $R(y_q)$ with $q > p$. The contact zone can be divided into two regions with the width of w_p and w_q, respectively, by the strip y_m. It is assumed that the maximum pressure at each contact region is directly proportional to the peak value of $R(y)$ and inversely proportional to the area of the contact region, the following relation holds according to Equation 3.13.

$$\left(\frac{k_1 - 1 + k_p}{k_1} \right)^2 = |C_n(y_m)|^{1.4} \left(\frac{R(y_p)}{R(y_q)} \right)^{0.8} \left(\frac{g_{yz}(0)w_q}{g_{yz}(y_p)w_p} \right)^{0.08} \tag{3.22}$$

Hence, the constant k_p is obtained as follows:

$$k_p = k_1 \sqrt{|C_n(y_m)|^{1.4} \left(\frac{R(y_p)}{R(y_q)} \right)^{0.8} \left(\frac{g_{yz}(0)w_q}{g_{yz}(y_p)w_p} \right)^{0.08}} + 1 - k_1 \tag{3.23}$$

Finally, the correction coefficient k_2 is defined as the following non-linear function:

$$k_2(y_i) = \begin{cases} k_p & i \leq p \\ R(y_i) & p < i < m \\ R(y_m) : \frac{R(y_q) - R(y_m)}{q-m} : R(y_q) & m \leq i \leq q \\ 1 & i > q \end{cases} \tag{3.24}$$

It should be noted that the function of k_2 is obtained under the assumption of $q > p$. If it is not the case, the sequence of k_2 should be reversed.

One example for a typical contact condition is presented in Figure 3.8 to better explain the relations among the relevant parameters introduced by the correction process. It can be observed from Figure 3.8 that the EKP model is suitable for this case, since there is a negative value in function C_n at strip m. The correction coefficient $k_2 > 1$ before strip p which means the contact pressure and contact length are amplified in this contact region and $k_2 = 1$ after strip q which means there is no correction applied in this region.
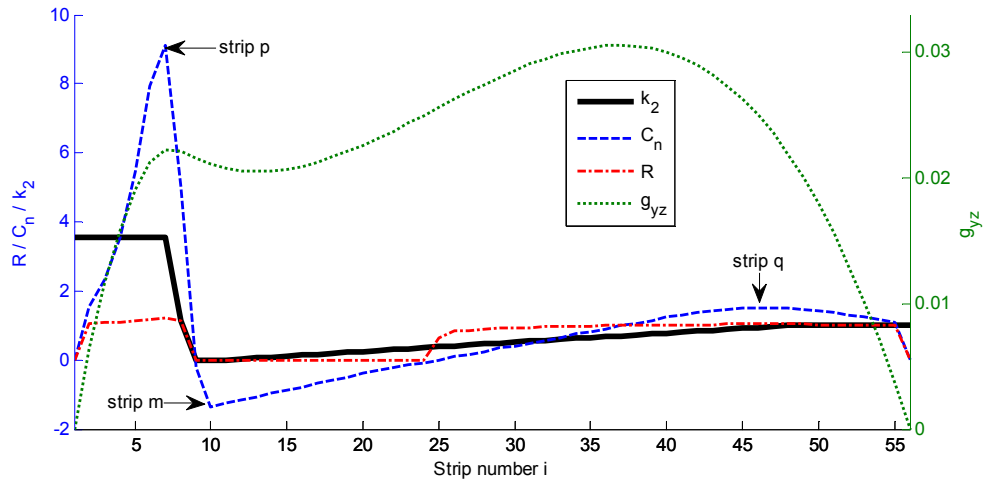
Figure 3.8: *Illustration of typical variables introduced for correction.*

3.4.3 Validation of the EKP model

In order to validate the proposed contact model and to show its improvement with re-
spect to the original KP, a set of comparisons have been performed among three models
namely EKP, KP and the CONTACT algorithm which is taken here as a reference. The
calculation parameters used for the simulations are listed in Table 3.1.

Table 3.1: *Calculation parameters*

Parameter type	Value
Wheel/rail profile combination	New S1002/UIC60
Rail inclination	1:40
Track gauge	1435 mm
Wheel flange back spacing	1360 mm
Tape circle to flange back distance	70 mm
Wheel radius	460 mm
Possion's ratio	0.3
Young's modulus	210 MPa

A first run by CONTACT with the parameters listed in Table 3.1 under a normal
force of 80 kN with various contact positions by setting the lateral displacement Δy
of the wheelset from -5 mm to 5 mm in 1 mm increment is conducted to select the
suitable simulation cases for further study. The calculated contact patches under the
given calculation conditions are presented in Figure 3.9.

24

| Δy=-5mm | Δy=-4mm | Δy=-3mm | Δy=-2mm | Δy=-1mm |

| Δy=0mm | Δy=1mm | Δy=2mm | Δy=3mm | Δy=4mm | Δy=5mm |
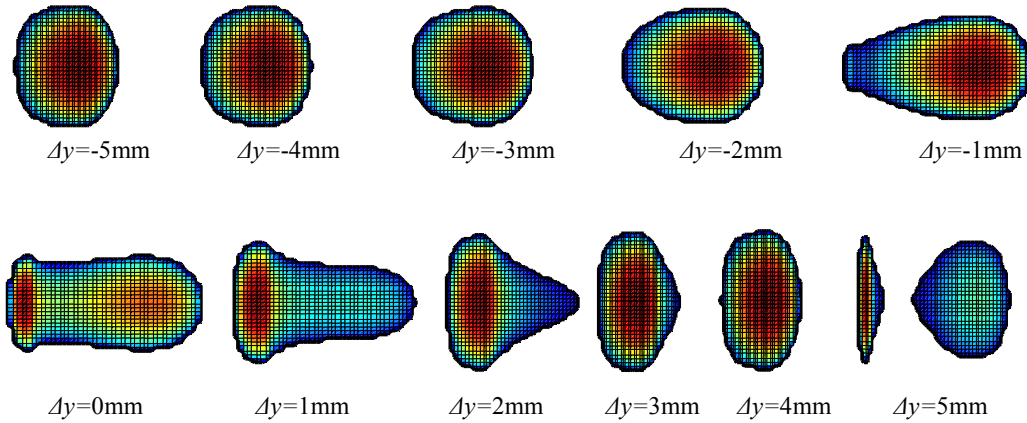
Figure 3.9: *Contact patch variation with lateral displacement (results of CONTACT calculations).*

Considering that the EKP is an extension version of the KP in the sense of the inclusion of yaw effect and the improvement for non-Hertzian contact estimation, the highly non-elliptic contact conditions where the wheelset has the displacement of -1 mm, 0 mm, 1 mm and 5 mm, respectively, are chosen for the purpose of comparisons among the three contact models.

The details of the simulation cases selected are summarized in Table 3.2 where F_n represents the normal load acting on the contact patch, and Δy denotes the lateral displacement of the wheelset with respect to the track.

Table 3.2: *Contact simulation cases*

Case	F_n [kN]	Δy [mm]	yaw angle [mrad]	Case	F_n [kN]	Δy [mm]	yaw angle [mrad]
1	40	-1	0	2	40	-1	25
3	40	-1	50	4	40	0	0
5	40	0	25	6	40	0	50
7	40	1	0	8	40	1	25
9	40	1	50	10	40	5	0
11	40	5	25	12	40	5	50
13	80	-1	0	14	80	-1	25
15	80	-1	50	16	80	0	0
17	80	0	25	18	80	0	50
19	80	1	0	20	80	1	25
21	80	1	50	22	80	5	0
23	80	5	25	24	80	5	50
25	120	-1	0	26	120	-1	25
27	120	-1	50	28	120	0	0
29	120	0	25	30	120	0	50
31	120	1	0	32	120	1	25
33	120	1	50	34	120	5	0
35	120	5	25	36	120	5	50

The geometrical point of contact for each case is determined in SIMPACK. The same undeformed distance surface $H(x, y)$ computed by the EKP model is used for the

same simulation case by different models. The detailed comparisons of the outputs are presented below. For the sake of simplicity, only the results concerning the shape and area of the contact patch and the pressure distribution along y-axis for the cases with a normal load of 80 kN, i.e. cases 13-24 are shown in separate figures in sequence.

It can be seen from Figure 3.10 that the correction in the contact width by the EKP improves the agreement with CONTACT compared to the KP, and it seems a little bit over corrected for the results shown in Figure 3.10 (b1) and (b2) but still better than the KP. When the contact patch tends to be elliptic as shown in Figure 3.10 (c1), the difference between the KP and EKP methods is marginal. The agreement between the three models is generally good in this case.
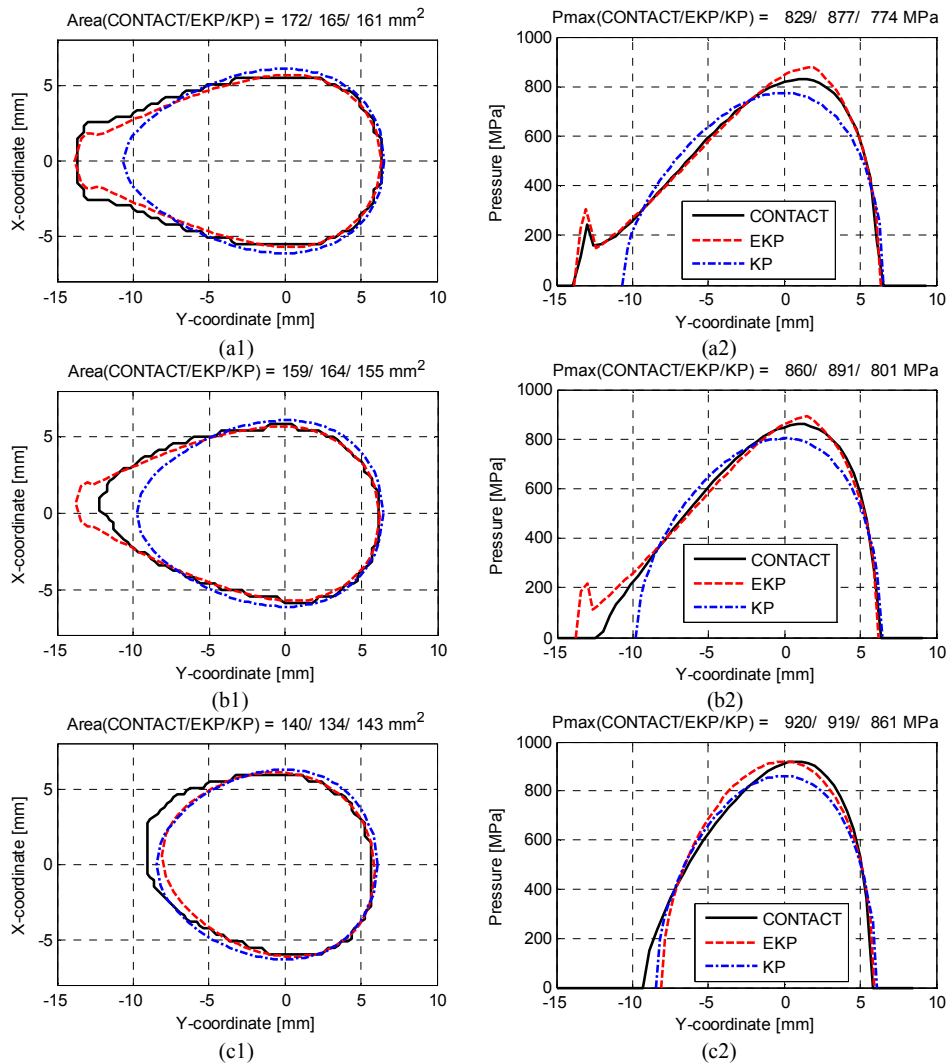
Figure 3.10: *Contact shape (left) and pressure distribution (right) for the cases with a constant lateral displacement of y= -1 mm, at an angle of yaw ψ=0 mrad (a1, a2), ψ=25 mrad (b1,b2) , and ψ=50 mrad (c1, c2), respectively.*

Figure 3.11 shows the contact condition formed when the wheelset is placed at the central position of the track. It can be observed that the KP can correctly predict the

contact shape when the yaw angle is small as shown in Figure 3.11 (a1) and (b1), while it fails to capture the peak in pressure. On the other hand, the discrepancies of the KP with respect to CONTACT in terms of contact shape and area increase with the increase of the yaw angle. Because the effect of the yaw angle is ignored in the original KP method, the contact patch is always symmetric about y-axis in contact plane. The difference between the KP and CONTACT is approximately 7% in terms of the area of the contact patch for 50 mrad yaw angle, see Figure 3.11 (c1). In contrast, the EKP has a good agreement with CONTACT in both contact shape and pressure distribution for all cases shown in Figure 3.11.
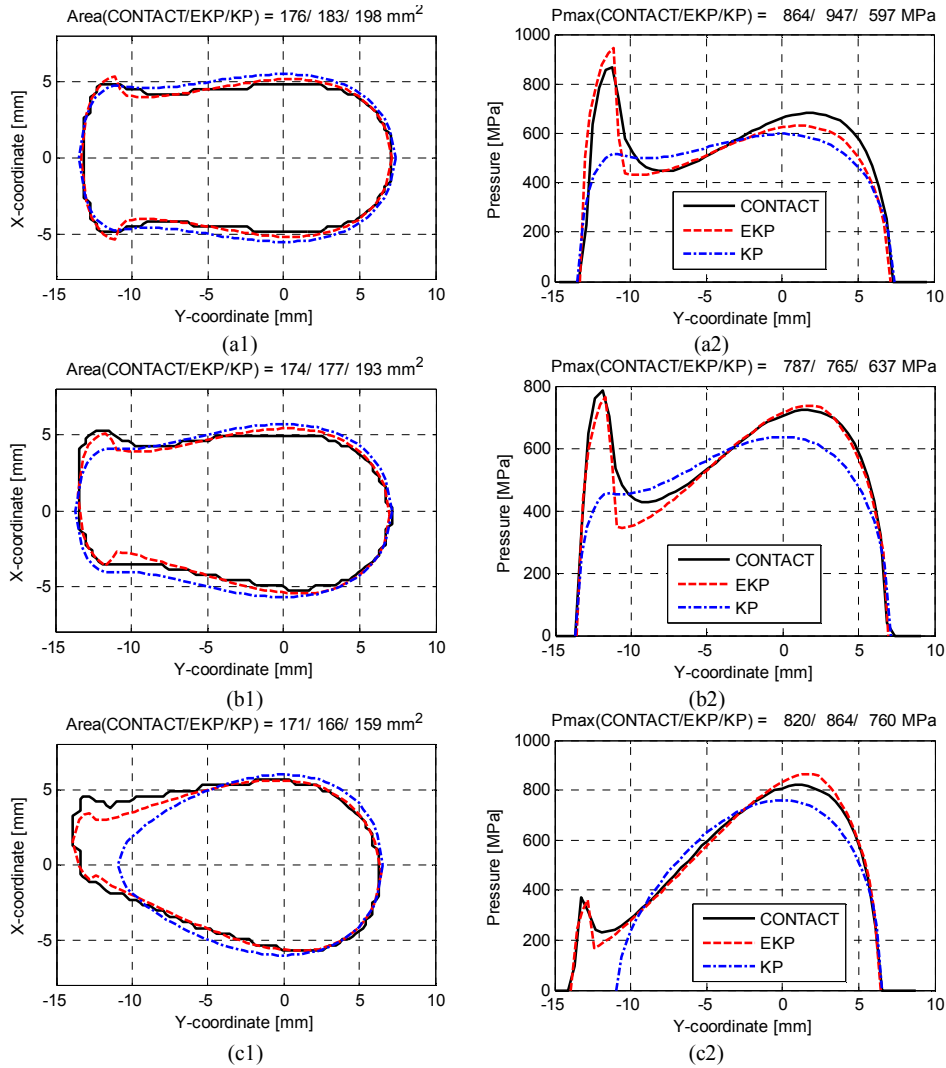
Figure 3.11: *Contact shape (left) and pressure distribution (right) for the cases with a constant lateral displacement of y= 0 mm, at an angle of yaw ψ=0 mrad (a1, a2), ψ=25 mrad (b1,b2) , and ψ=50 mrad (c1, c2), respectively.*

Figure 3.12 shows the results obtained for the cases with lateral displacement $y=1$ mm and yaw angles $\psi=0$, 25 and 50 mrad. It can be seen that the contact width predicted by the KP is shorter compared with CONTACT, although the contact shapes

estimated by these two methods are similar when the yaw angle is less than 25 mrad. The difference between the KP and CONTACT in terms of the contact shape is significant when the yaw angle is 50 mrad. In contrast, the contact shapes are in good agreement between the EKP and CONTACT for all cases shown in Figure 3.12. However, the pressure distributions predicted by the EKP and KP are similar when the yaw angle is less than 25 mrad, and they deviate from CONTACT as shown in Figure 3.12 (a2) and (b2). Because the pressure peaks appear over the geometrical point of contact, there is no correction for the EKP in this case. The maximum difference in pressure with reference to CONTACT is approximately 22%. The last case shown in Figure 3.12 (c2) suggests that the EKP is able to improve the accuracy of the KP significantly in presence of a yaw angle, taking CONTACT as a reference.
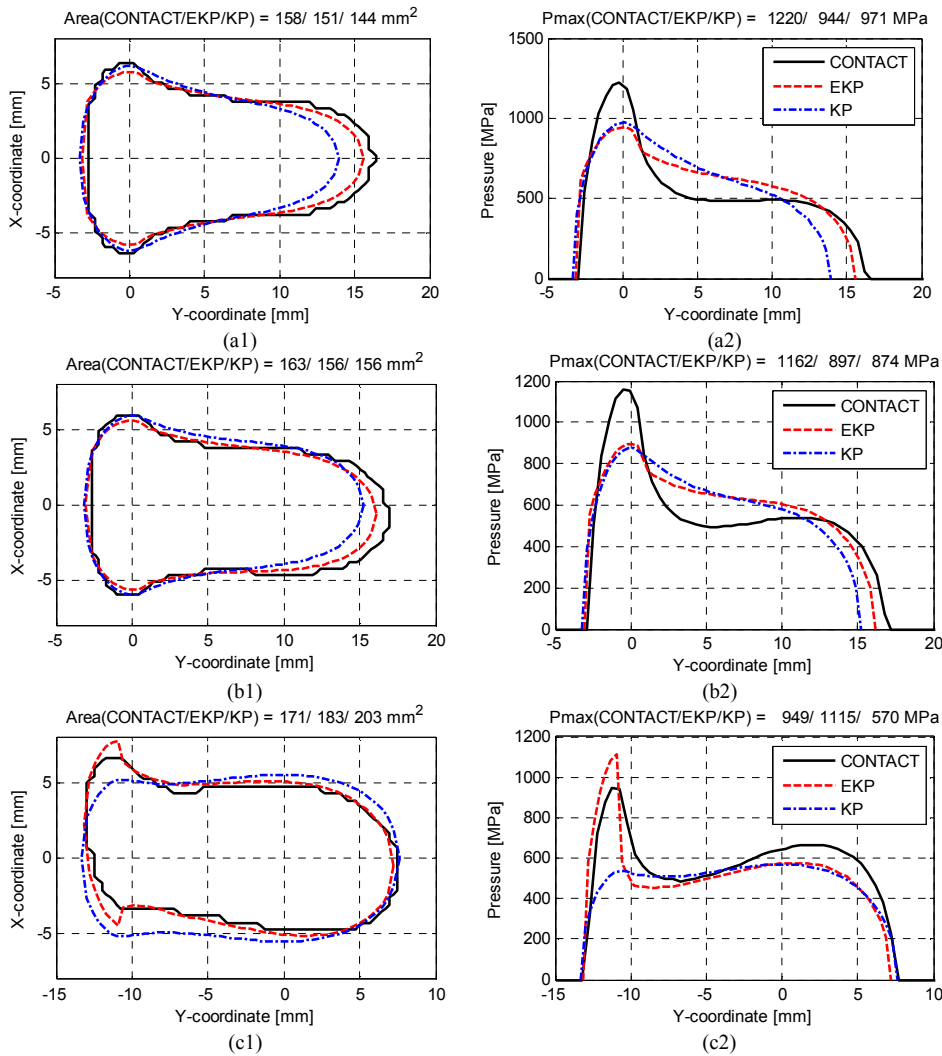
Figure 3.12: *Contact shape (left) and pressure distribution (right) for the cases with a constant lateral displacement of y= 1 mm, at an angle of yaw ψ=0 mrad (a1, a2), ψ=25 mrad (b1,b2) , and ψ=50 mrad (c1, c2), respectively.*

Figure 3.13 shows the results obtained for the cases with lateral displacement y =5

mm and yaw angles ψ=0, 25 and 50 mrad. These results show that the KP predicts a jointed contact patch, while the EKP and CONTACT produce similar results with two separate contact patches. Once again, the KP model fails to capture the maximum pressure values for such highly non-elliptic contact conditions as shown in Figure 3.13 (a2) and (b2). Moreover, the considerable effect of yaw angle on the contact shape presented in Figure 3.13 (b1) is missing in the KP's result. In addition, the same conclusion that the results from three contact models are in good agreement under a nearly elliptic contact condition can be drawn as for Figure 3.10(c1) and (c2) once again from Figure 3.13 (c1) and (c2).
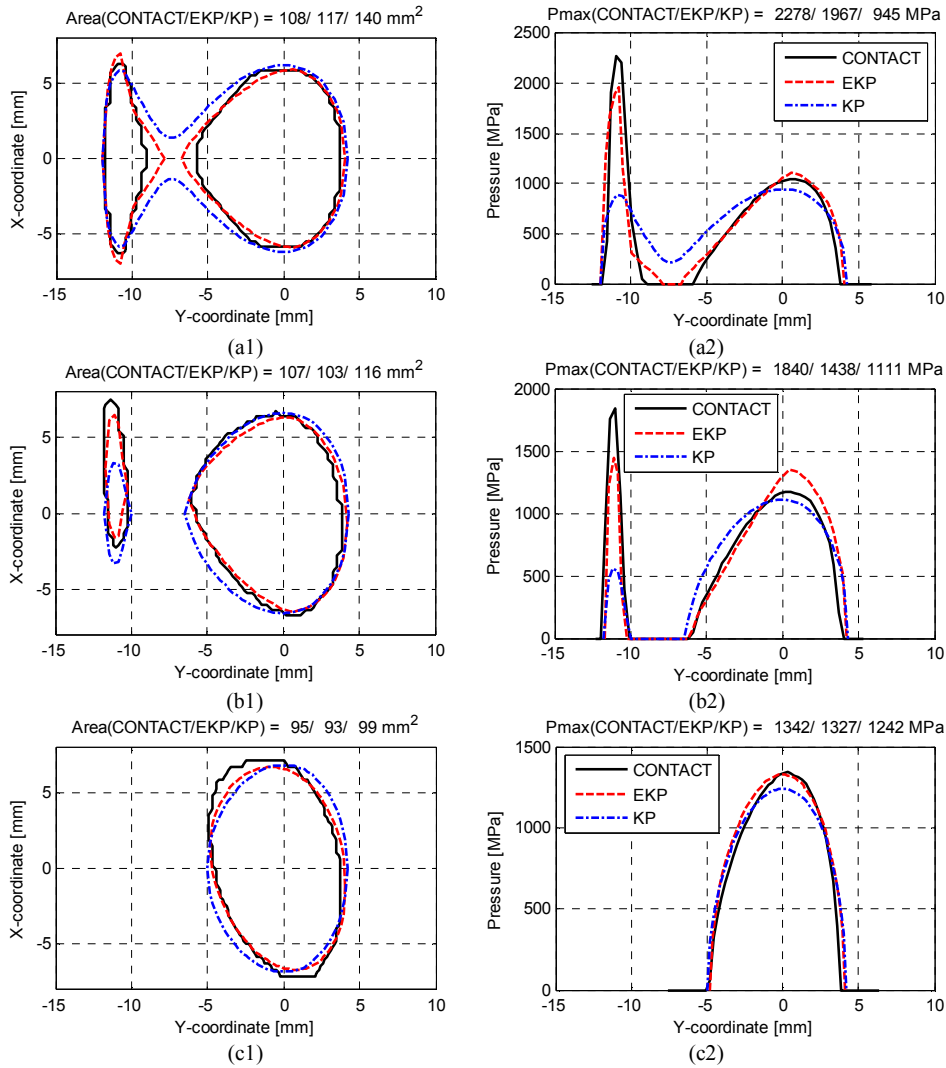
Figure 3.13: *Contact shape (left) and pressure distribution (right) for the cases with a constant lateral displacement of y= 5 mm, at an angle of yaw ψ=0 mrad (a1, a2), ψ=25 mrad (b1,b2) , and ψ=50 mrad (c1, c2), respectively.*

To compare the EKP and KP with respect to CONTACT for a wider range of contact conditions, the results for all cases listed in Table 3.2 in terms of the contact area and the maximum pressure are plotted against CONTACT's corresponding results in Figure

3.14 (a) and (b), respectively. Moreover, the coefficients of determination R^2 for the KP and EKP models are computed by taking CONTACT as the regression line to measure their deviations from CONTACT.
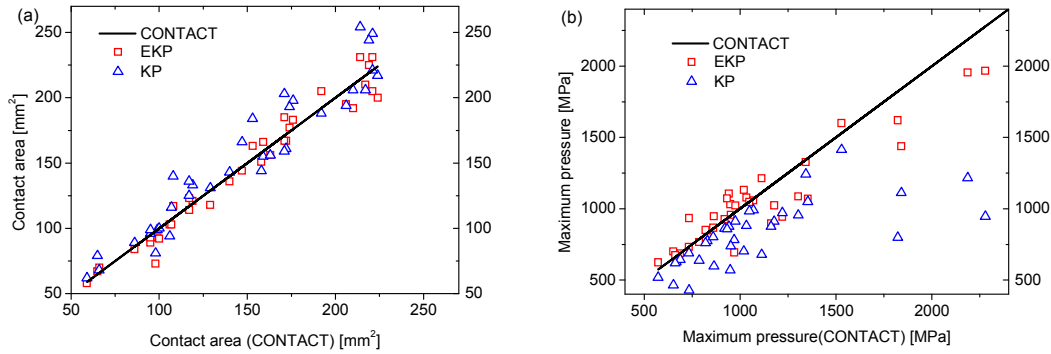
Figure 3.14: *Comparisons of the correspondence to CONTACT:(a) contact area (b) maximum pressure.*

As far as the contact area is concerned, see Figure 3.14 (a), the coefficients of determination for the KP and EKP are 0.92 and 0.96, respectively. It means both models have a good agreement with CONTACT, with the EKP being closer to CONTACT with respect to the KP since its coefficient of determination is a little bit larger. The coefficients of determination for the KP and EKP in terms of the maximum pressure over the contact patch are 0.45 and 0.91, respectively. With reference to Figure 3.14 (b), it can be concluded that the EKP substantially improves the correspondence to CONTACT compared with the KP, in terms of the maximum pressure obtained in the CONTACT. The deviation of the KP from CONTACT rapidly increases when the maximum pressure is larger than 1500 MPa.

It should be kept in mind that the comparisons considered in Figure 3.14 are only made for the contact area and maximum pressure within the contact patch. Extending the comparison to include more details, e.g. the shape of the contact patch and the pressure distribution over the contact patch, the advantages of the EKP are expected to be more remarkable compared to the KP as shown in some of the cases presented in Figure 3.10-Figure 3.13.

In the light of the results shown, it can be concluded that the results obtained by the EKP improve substantially the agreement with CONTACT in terms of the shape and size of the contact patch as well as the pressure distribution over the contact patch with various yaw angle of the wheelset against the track for all contact conditions considered, whereas the results of the KP are not satisfactory for highly non-Hertzian contact conditions and the KP is not able to take the effect of the yaw angle into account. It can also be concluded that the effect of the yaw angle on the normal contact solution is significant when the angle is around 25-50 mrad, especially accompanied by a large lateral displacement of the wheelset, because the contact patch could change from non-elliptic contact to nearly elliptic with the change of the yaw angle, as presented in Figure 3.10 and Figure 3.13, and also could change from double-point contact to single-point contact as shown in Figure 3.13.

These variations caused by the yaw angle will not only influence the normal contact solution as discussed above but also the tangential contact solution which depends on

the shape and size of the contact patch, the distribution of the normal pressure and friction between the wheel and rail, and subsequently the contact deterioration mechanisms as well as the vehicle's dynamic behaviour. Therefore, the effect of yaw should be taken into account for wheel-rail contact calculation and rail vehicle dynamics simulation.

The analyses and comparisons have shown that the proposed contact model is capable of solving wheel-rail normal contact problem taking into account the effect of yaw for the contact conditions under consideration. Similar conclusions for the case of wheel-roller contact can be expected. Therefore, no further discussion of that case is reported, for the sake of conciseness. Of course, massive comparisons need to be done for wider conditions of contact to verify the scope of application of the proposed model, such as worn wheel and rail contact, flange contact, and multi-point contact formed with varied load and yaw angles, which are the task of future research.

3.5 Kinematic problem

Due to the elasticity of the bodies and the externally applied normal load, when tangential forces are applied to wheel-rail contact, some points on the surfaces in the contact region may slip while others may stick when the two bodies move relatively to each other. The difference between the tangential strains of the bodies in the adhesion area leads to a small apparent slip. This slip normalized by the rolling speed is called creepage and is defined using the kinematics of the two bodies. Therefore, the aim of this section is to determine the creepages in the wheel-rail/roller interface.
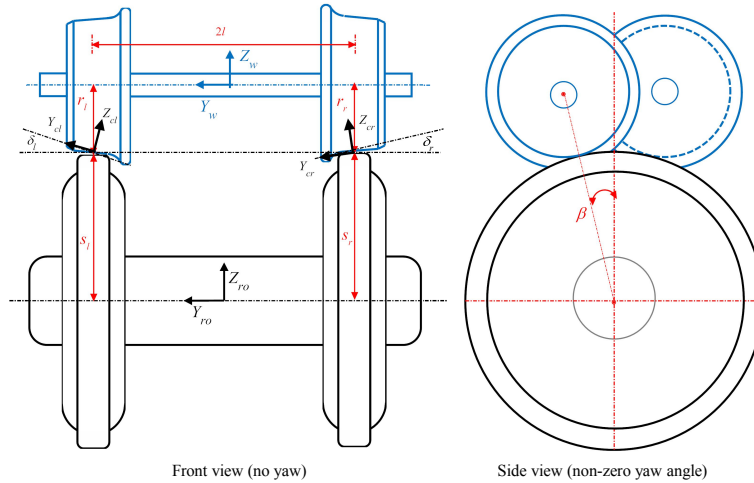
Figure 3.15: *A wheelset rests on rollers.*

3.5.1 Kinematics of a wheelset on rollers

For the single wheelset roller rig, the wheelset on the roller has the same degrees of freedom as on a track, except the constraint in longitudinal direction. Furthermore, the two rollers fixed on the same axle can only rotate around its axle. To accomplish the kinematic analysis of a wheelset on rollers, a convenient set of reference frame systems should be introduced as shown in Figure 3.15. The wheelset reference frame is denoted by $O_w X_w Y_w Z_w$ attached to the wheelset's center of mass so that axis $O_w Y_w$

coincides with the wheelset's axis of rotation, the $O_w Z_w$ axis points upwards and the $O_w X_w$ axis completes the right-handed coordinate system. Similarly, a roller reference frame is introduced and denoted by $O_{ro} X_{ro} Y_{ro} Z_{ro}$ attached to the roller's center of mass which is defined as the inertial frame. Two contact reference frames $O_{cl} X_{cl} Y_{cl} Z_{cl}$ and $O_{cr} X_{cr} Y_{cr} Z_{cr}$ are introduced at the contact interfaces between the wheelset and roller on the left and right sides at the wheelset central position.

It is assumed that the wheelset reference frame $O_w X_w Y_w Z_w$ is obtained from the inertial frame by performing two successive rotations. The axes of the reference frames are parallel before rotation, and the first rotation is made about the z-axis by an angle ψ called yaw angle (positive in counter-clockwise direction) followed by a second rotation about the x-axis by an angle ϕ called roll angle. Therefore, the transformation matrix A^{w2i} connecting the wheelset frame to the inertial frame is expressed as follows:

$$A^{w2i} = \begin{bmatrix} \cos\psi & -\sin\psi & 0 \\ \sin\psi\cos\phi & \cos\psi\cos\phi & -\sin\phi \\ \sin\psi\sin\phi & \cos\psi\sin\phi & \cos\phi \end{bmatrix}. \tag{3.25}$$

Since the angles of rotation are generally small in railway dynamics, the small angle approximation can be applied, so that the transformation matrix reduces to:

$$A^{w2i} \approx \begin{bmatrix} 1 & -\psi & 0 \\ \psi & 1 & -\phi \\ 0 & \phi & 1 \end{bmatrix}. \tag{3.26}$$

The position vectors of the contact points on the wheel and roller can be defined in the inertial frame as follows:

$$r_{wi} = R_w + A^{w2i}\bar{u}_{wi} \quad (i = l, r) \tag{3.27}$$

where the position vector of the origin of the wheelset reference frame in the inertial frame is expressed as follows:

$$R_w = \begin{bmatrix} 0 & y & z \end{bmatrix}^T \tag{3.28}$$

and the position vectors of the contact points in the wheelset reference frame can be expressed in the following forms: for the left-hand wheel

$$\bar{u}_{wl} = \begin{bmatrix} r_l\sin\beta & l & -r_l\cos\beta \end{bmatrix}^T \tag{3.29}$$

and for the right-hand wheel

$$\bar{u}_{wr} = \begin{bmatrix} -r_r\sin\beta & -l & -r_r\cos\beta \end{bmatrix}^T \tag{3.30}$$

where $r_i(i = l, r)$ represents the radius of the left and right wheels, l is the half distance between the contact points on the left and right wheels, and β is the shift angle of the contact point on the roller with respect to the vertical plane of the inertial frame in presence of a non-zero angle of yaw. It is assumed that this angle is the same for the left-hand and right-hand sides on the roller and can be approximated by Equation 3.31, since it is very small in ordinary circumstances.

$$\beta = \frac{l\psi}{s_0 + r_0} \tag{3.31}$$

In Equation 3.31, r_0 and s_0 denote the nominal radii of the wheel and roller, respectively.

Taking the derivative of the Equation of 3.27, the velocity vector of the contact point located on the wheel with respect to the inertial frame is obtained as:

$$v_{wi} = \dot{R}_w + \omega_w \times u_{wi} \quad (i = l, r) \tag{3.32}$$

where $u_{wi} = A^{w2i}\bar{u}_{wi}$ is the position vector of the point of contact on the wheel defined in the inertial frame which is determined from Equations 3.26, 3.29 and 3.30 for the left-hand and right-hand wheels, respectively, as follows:

$$u_{wl} = A^{w2i}\bar{u}_{wl} \approx \begin{bmatrix} r_l \sin\beta - l\psi \\ r_l\psi\sin\beta + l + r_l\phi\cos\beta \\ l\phi - r_l\cos\beta \end{bmatrix} \approx \begin{bmatrix} r_l\beta - l\psi \\ l + r_l\phi \\ l\phi - r_l \end{bmatrix} \tag{3.33}$$

and

$$u_{wr} = A^{w2i}\bar{u}_{wr} \approx \begin{bmatrix} -r_r\sin\beta + l\psi \\ -r_r\psi\sin\beta - l + r_r\phi\cos\beta \\ -l\phi - r_r\cos\beta \end{bmatrix} \approx \begin{bmatrix} -r_r\beta + l\psi \\ -l + r_r\phi \\ -l\phi - r_r \end{bmatrix} \tag{3.34}$$

and ω_w is the absolute angular velocity vector at the point of contact defined in the inertial system as:

$$\omega_w = \begin{bmatrix} 0 \\ 0 \\ \dot{\psi} \end{bmatrix} + A^{w2i}\begin{bmatrix} \dot{\phi} \\ \Omega_w \\ 0 \end{bmatrix} = \begin{bmatrix} \dot{\phi}\cos\psi - \Omega_w\sin\psi\cos\phi \\ \dot{\phi}\sin\psi + \Omega_w\cos\psi\cos\phi \\ \dot{\psi} + \Omega_w\sin\phi \end{bmatrix} \approx \begin{bmatrix} \dot{\phi} - \Omega_w\psi \\ \dot{\phi}\psi + \Omega_w \\ \dot{\psi} + \Omega_w\phi \end{bmatrix} \tag{3.35}$$

with $\Omega_w = \frac{V}{r_0}$ the rolling angular velocity of the wheelset.

Substituting Equations 3.28, 3.33, 3.34 and 3.35 into Equation 3.32, the velocity vectors of the contact points on the wheelset in the inertial frame are obtained as follows: for the left-hand wheel

$$v_{wl} = \dot{R}_w + \omega_w \times u_{wl}$$

$$\approx \begin{bmatrix} 0 \\ \dot{y} \\ \dot{z} \end{bmatrix} + \begin{bmatrix} l(\dot{\phi}\psi\phi - \dot{\psi}) - r_l(\dot{\phi}\psi + \dot{\psi}\phi + \Omega_w) \\ l(-\dot{\psi}\psi - \dot{\phi}\phi) + r_l(\dot{\psi}\beta + \dot{\phi} - \Omega_w\psi) \\ l\dot{\phi} + r_l(\dot{\phi}\phi - \Omega_w\beta) \end{bmatrix} \tag{3.36}$$

$$\approx \begin{bmatrix} -l\dot{\psi} - r_l(\dot{\phi}\psi + \dot{\psi}\phi + \Omega_w) \\ \dot{y} + l(-\dot{\psi}\psi - \dot{\phi}\phi) + r_l(\dot{\psi}\beta + \dot{\phi} - \Omega_w\psi) \\ \dot{z} + l\dot{\phi} + r_l(\dot{\phi}\phi - \Omega_w\beta) \end{bmatrix}$$

and for the right-hand wheel

$$
v_{wr} = \dot{R}_w + \omega_w \times u_{wr}
$$

$$
\approx \begin{bmatrix} 0 \\ \dot{y} \\ \dot{z} \end{bmatrix} + \begin{bmatrix} l(-\dot{\phi}\psi\phi + \dot{\psi}) - r_r(\dot{\phi}\psi + \dot{\psi}\phi + \Omega_w) \\ l(\dot{\psi}\psi + \dot{\phi}\phi) + r_r(-\dot{\psi}\beta + \dot{\phi} - \Omega_w\psi) \\ -l\dot{\phi} + r_r(\dot{\phi}\phi + \Omega_w\beta) \end{bmatrix}
$$

$$
\approx \begin{bmatrix} l\dot{\psi} - r_r(\dot{\phi}\psi + \dot{\psi}\phi + \Omega_w) \\ \dot{y} + l(\dot{\psi}\psi + \dot{\phi}\phi) + r_r(-\dot{\psi}\beta + \dot{\phi} - \Omega_w\psi) \\ \dot{z} - l\dot{\phi} + r_r(\dot{\phi}\phi + \Omega_w\beta) \end{bmatrix} .
$$

(3.37)

Similarly, the velocity vector of the contact point on the roller in the inertial frame can be expressed as

$$
v_{roi} = \omega_{ro} \times u_{roi} \quad (i = l, r) \tag{3.38}
$$

where ω_{ro} is the angular velocity of the roller with the following form:

$$
\omega_{ro} = \begin{bmatrix} 0 \\ \Omega_{or} \\ 0 \end{bmatrix} = \begin{bmatrix} 0 \\ -\frac{V}{s_0} \\ 0 \end{bmatrix} \tag{3.39}
$$

and u_{roi} stands for the position vector of the contact point in the inertial frame. For the left-hand roller, the expression of this vector is

$$
u_{rol} = \begin{bmatrix} -s_l \sin \beta & l & s_l \cos \beta \end{bmatrix}^T \tag{3.40}
$$

and for the right-hand roller the expression is

$$
u_{ror} = \begin{bmatrix} s_r \sin \beta & -l & s_r \cos \beta \end{bmatrix}^T \tag{3.41}
$$

Hence, the velocity vectors of the points of contact are obtained. For the left-hand roller

$$
v_{rol} = \omega_{ro} \times u_{rol} = \begin{bmatrix} 0 \\ -\frac{V}{s_0} \\ 0 \end{bmatrix} \times \begin{bmatrix} -s_l \sin \beta \\ l \\ s_l \cos \beta \end{bmatrix} = \begin{bmatrix} -\frac{V}{s_0} s_l \cos \beta \\ 0 \\ -\frac{V}{s_0} s_l \sin \beta \end{bmatrix} \approx \begin{bmatrix} -\frac{V}{s_0} s_l \\ 0 \\ -\frac{V}{s_0} s_l \beta \end{bmatrix} \tag{3.42}
$$

and for the right-hand roller

$$
v_{ror} = \omega_{ro} \times u_{ror} = \begin{bmatrix} 0 \\ -\frac{V}{s_0} \\ 0 \end{bmatrix} \times \begin{bmatrix} s_r \sin \beta \\ -l \\ s_r \cos \beta \end{bmatrix} = \begin{bmatrix} -\frac{V}{s_0} s_r \cos \beta \\ 0 \\ \frac{V}{s_0} s_r \sin \beta \end{bmatrix} \approx \begin{bmatrix} -\frac{V}{s_0} s_r \\ 0 \\ \frac{V}{s_0} s_r \beta \end{bmatrix} . \tag{3.43}
$$

Thus the velocity difference between the wheel and roller at each point of contact in the inertial frame can be calculated as follows. For the left side

$$\Delta v_l = v_{wl} - v_l - = \begin{bmatrix} -l\dot{\psi} - r_l(\dot{\phi}\psi + \dot{\psi}\phi + \Omega_w) + \frac{V}{s_0}s_l \\\\ \dot{y} + l(-\dot{\psi}\psi - \dot{\phi}\phi) + r_l(\dot{\psi}\beta + \dot{\phi} - \Omega_w\psi) \\\\ \dot{z} + l\dot{\phi} + r_l(\dot{\phi}\phi - \Omega_w\beta) + \frac{V}{s_0}s_l\beta \end{bmatrix} \quad (3.44)$$

for the right side

$$\Delta v_r = v_{wr} - v_r - = \begin{bmatrix} l\dot{\psi} - r_r(\dot{\phi}\psi + \dot{\psi}\phi + \Omega_w) + \frac{V}{s_0}s_r \\\\ \dot{y} + l(\dot{\psi}\psi + \dot{\phi}\phi) + r_r(-\dot{\psi}\beta + \dot{\phi} - \Omega_w\psi) \\\\ \dot{z} - l\dot{\phi} + r_r(\dot{\phi}\phi + \Omega_w\beta) - \frac{V}{s_0}s_r\beta \end{bmatrix} \quad (3.45)$$

and the difference of angular velocity is

$$\Delta\omega = \omega_w - \omega_{ro} = \begin{bmatrix} \dot{\phi}\cos\psi - \Omega_w\sin\psi\cos\phi \\ \dot{\phi}\sin\psi + \Omega_w\cos\psi\cos\phi + \frac{V}{s_0} \\ \dot{\psi} + \Omega_w\sin\phi \end{bmatrix} \approx \begin{bmatrix} \dot{\phi} - \Omega_w\psi \\ \dot{\phi}\psi + \Omega_w + \frac{V}{s_0} \\ \dot{\psi} + \Omega_w\phi \end{bmatrix}. \quad (3.46)$$

To determine the creepages and spin, the velocity differences obtained above must be projected in the contact plane where they are defined. It is assumed that the contact frames are connected to the wheelset frame by the following transformation matrices for the left and right wheels, respectively.

$$A^{w2cl} = \begin{bmatrix} \cos\beta & 0 & \sin\beta \\ -\sin\beta\sin\delta_l & \cos\delta_l & \cos\beta\sin\delta_l \\ -\sin\beta\cos\delta_l & -\sin\delta_l & \cos\beta\cos\delta_l \end{bmatrix} \approx \begin{bmatrix} 1 & 0 & \beta \\ 0 & 1 & \delta_l \\ -\beta & -\delta_l & 1 \end{bmatrix} \quad (3.47)$$

and

$$A^{w2cr} = \begin{bmatrix} \cos\beta & 0 & -\sin\beta \\ -\sin\beta\sin\delta_r & \cos\delta_r & -\cos\beta\sin\delta_r \\ \sin\beta\cos\delta_r & \sin\delta_r & \cos\beta\cos\delta_r \end{bmatrix} \approx \begin{bmatrix} 1 & 0 & -\beta \\ 0 & 1 & -\delta_r \\ \beta & \delta_r & 1 \end{bmatrix} \quad (3.48)$$

where $\delta_i(i = l, r)$ denotes the contact angle.

Hence, the transformation matrices connecting the inertial frame to the contact frame can be obtained for the left and right side wheels by the following operation. For the left side

$$A^{i2cl} = A^{w2cl}A^{i2w} = A^{w2cl}(A^{w2i})^T$$

$$\approx \begin{bmatrix} 1 & 0 & \beta \\ 0 & 1 & \delta_l \\ -\beta & -\delta_l & 1 \end{bmatrix} \begin{bmatrix} 1 & \psi & 0 \\ -\psi & 1 & \phi \\ 0 & -\phi & 1 \end{bmatrix} \approx \begin{bmatrix} 1 & \psi & \beta \\ -\psi & 1 & \delta_l + \phi \\ -\beta & -\delta_l - \phi & 1 \end{bmatrix} \quad (3.49)$$

and for the right side

$$A^{i2cr} = A^{w2cr} A^{i2w} = A^{w2cr} (A^{w2i})^T$$

$$\approx \begin{bmatrix} 1 & 0 & -\beta \\ 0 & 1 & -\delta_r \\ \beta & \delta_r & 1 \end{bmatrix} \begin{bmatrix} 1 & \psi & 0 \\ -\psi & 1 & \phi \\ 0 & -\phi & 1 \end{bmatrix} \approx \begin{bmatrix} 1 & \psi & -\beta \\ -\psi & 1 & -\delta_r + \phi \\ \beta & \delta_r - \phi & 1 \end{bmatrix}. \tag{3.50}$$

The velocity differences between the wheelset and rollers in the contact plane are obtained. For the left side

$$\Delta v_{cl} = A^{i2cl} \Delta v_l \tag{3.51}$$

$$\Delta \omega_{cl} = A^{i2cl} \Delta \omega \tag{3.52}$$

Therefore, the longitudinal component is

$$\Delta v_{clx} \approx -l\dot{\psi} - r_l \dot{\psi}\phi - V\frac{r_l}{r_0} + V\frac{s_l}{s_0} + \dot{y}\psi + \beta\dot{z} + l\dot{\phi}\beta \tag{3.53}$$

the lateral component is

$$\Delta v_{cly} \approx \dot{y} - V\psi\frac{s_l}{s_0} + r_l\dot{\psi}\beta + r_l\dot{\phi} + \delta_l\dot{z} + l\delta_l\dot{\phi} + \phi\dot{z} \tag{3.54}$$

and the normal component of the rotation is

$$\Delta \omega_{clz} \approx -\beta\dot{\phi} - V\frac{\delta}{r_0} - V\frac{\delta}{s_0} - V\frac{\phi}{s_0} + \dot{\psi} \tag{3.55}$$

For the right side

$$\Delta v_{cr} = A^{i2cr} \Delta v_r \tag{3.56}$$

$$\Delta \omega_{cr} = A^{i2cr} \Delta \omega \tag{3.57}$$

Therefore, the longitudinal component is

$$\Delta v_{crx} \approx l\dot{\psi} - r_r\dot{\psi}\phi - V\frac{r_r}{r_0} + V\frac{s_r}{s_0} + \dot{y}\psi - \beta\dot{z} + l\dot{\phi}\beta \tag{3.58}$$

the lateral component is

$$\Delta v_{cry} \approx \dot{y} - V\psi\frac{s_r}{s_0} - r_r\dot{\psi}\beta + r_r\dot{\phi} + \delta_r\dot{z} + l\delta_r\dot{\phi} - \phi\dot{z} \tag{3.59}$$

and the normal component of the rotation is

$$\Delta \omega_{crz} \approx \beta\dot{\phi} + V\frac{\delta}{r_0} + V\frac{\delta}{s_0} - V\frac{\phi}{s_0} + \dot{\psi}. \tag{3.60}$$

Now, the creepages can be obtained by definition as follows. The longitudinal creepages on the left- and right-hand wheels are

$$\xi_{lx} = \frac{\Delta v_{clx}}{V} \approx \frac{-l\dot{\psi} - r_l\dot{\psi}\phi - V\frac{r_l}{r_0} + V\frac{s_l}{s_0} + \dot{y}\psi + \beta\dot{z} + l\dot{\phi}\beta}{V} \tag{3.61}$$

$$\xi_{rx} = \frac{\Delta v_{clx}}{V} \approx \frac{l\dot{\psi} - r_r\dot{\psi}\phi - V\frac{r_r}{r_0} + V\frac{s_r}{s_0} + \dot{y}\psi - \beta\dot{z} + l\dot{\phi}\beta}{V} \tag{3.62}$$

the lateral creepages are

$$\xi_{ly} = \frac{\Delta v_{cly}}{V} \approx \frac{\dot{y} - V\psi\frac{s_l}{s_0} + r_l\dot{\psi}\beta + r_l\dot{\phi} + \delta_l\dot{z} + l\delta_l\dot{\phi} + \phi\dot{z}}{V} \tag{3.63}$$

$$\xi_{ry} = \frac{\Delta v_{cry}}{V} \approx \frac{\dot{y} - V\psi\frac{s_r}{s_0} - r_r\dot{\psi}\beta + r_r\dot{\phi} + \delta_r\dot{z} + l\delta_r\dot{\phi} - \phi\dot{z}}{V} \tag{3.64}$$

and the spin creepages are

$$\xi_{lz} = \frac{\Delta \omega_{crz}}{V} \approx \frac{-\beta\dot{\phi} - V\frac{\delta}{r_0} - V\frac{\delta}{s_0} - V\frac{\phi}{s_0} + \dot{\psi}}{V} \tag{3.65}$$

$$\xi_{rz} = \frac{\Delta \omega_{crz}}{V} \approx \frac{\beta\dot{\phi} + V\frac{\delta}{r_0} + V\frac{\delta}{s_0} - V\frac{\phi}{s_0} + \dot{\psi}}{V}. \tag{3.66}$$

It can be seen from the expressions above that the radius of the roller and the shift angle (function of yaw) contribute to the differences in terms of the longitudinal and lateral creepages and spin with respect to wheel-rail contact condition. Moreover, the longitudinal and lateral creepages can be simplified further by assuming that the contacting bodies remain in contact at all times which means the z components vanish in the corresponding expressions. Knowing these quantities, the creep forces and spin moment can be calculated as shown in Section 3.6. Moreover, it should be noted that the forces and moment obtained are defined in the contact reference frame, they must be transformed to the inertial frame before being substituted to the equations of motion.

3.5.2 Kinematics of a wheelset on a track

The wheel-rail contact can be considered as the limit condition of wheel-roller contact when the radius of roller goes to infinite. It means the corresponding expressions for wheel-rail contact condition can be obtained by setting $s_0 = \infty$ and $\beta = 0$ in equations 3.61-3.66. Therefore, the kinematics behaviour of the wheelset on a track can be derived easily by following the same procedure described above. Any terms in the preceding equations that include the quantity of roller radius present the differences between the wheel-rail contact and wheel-roller contact from kinematic point of view.

3.6 Tangential problem

Tangential forces arise due to the relative motion between wheel and rail. However, the resolution of the tangential problem has been the question that draws the attention of researchers, leading to define different contact theories [19]. A brief review of the development of the theories for solving wheel-rail tangential contact problem will be given first, and this is followed by a description of the method applied in the current study.

3.6.1 Review of methods for solving the wheel-rail tangential problem

The tangential contact problem in the context of wheel-rail system refers to the rolling contact. Continuum rolling contact theory started with a publication by Carter in 1926 [24], in which he approximated the wheel as a cylinder and the rail as an infinite

half-space. The analysis was bi-dimensional and an exact solution was found. Carter showed that the difference between the circumferential velocity of a driven wheel and the translational velocity of the wheel has a non-zero value as soon as an accelerating or braking torque is applied to the wheel. This difference is called creepage that increases as the torque increases until the maximum value according to Coulomb's law is reached, this phenomenon is referred to as saturation. Carter formulated a creep-force law relating the driving-braking torque and the velocity difference.

In 1958, Johnson derived an approximate three-dimensional solution to the rolling contact problem, considering both longitudinal and lateral creep forces [51]. Johnson analysed an elastic sphere rolling on an elastic plane and assumed that the overall contact patch is circular, and that the adhesion region is also circular and tangent to the leading edge of the contact patch, as shown in 1938 by Cattaneo [25]. Johnson verified his findings experimentally and also investigated the effects of spin creepage on lateral creep force [51]. Vermeulen and Johnson [101] expanded Johnson's earlier work and obtained an approximate solution for creep forces in the case of an elliptical contact patch, neglecting the spin creepage.

In 1976, Kalker suggested that, for very small creepages, the area of slip is very small and its effect can be neglected which is known as Kalker's linear theory [55]. A program called FASTSIM, which is based on the simplified theory, was developed by Kalker in 1982 [56] and has been widely used in railway vehicle computer programs. In 1984, Kalker calculated the creepage and spin coefficients when the relative slip is small but the contact area is not necessarily elliptic. These calculations were made with the aid of the program CONTACT [57].

In 1983, Shen *et al*. [94]. suggested a new approximate heuristic nonlinear theory based on Kalker's linear theory. In this theory, the saturation law of Johnson and Vermeulen is used, and the effect of spin creepage on the creep forces is considered. The longitudinal and lateral creep forces are first calculated using Kalker's linear theory.

In 1999, Polach [85] introduced an algorithm for the computation of the wheel/rail creep forces, which is implemented in some computer codes for the dynamic simulation of railway systems. All of this work is Hertzian-based, giving contact solutions for a class of geometrical objects satisfying the half-space restriction.

3.6.2   Extended FASTSIM algorithm

The common method to solve the wheel-rail tangential contact problem is represented by the FASTSIM algorithm due to Kalker. This method was originally developed for elliptic contact condition, but can be extended to cover a more general geometry of the contact patch. The difficulty is to determine the flexibility parameter that is required by this method. To overcome this, Kik and Piotrowski proposed a method to define an equivalent ellipse for each separate contact zone by setting the ellipse area equal to the non-elliptic contact area and the ellipse semi-axes ratio equal to length to width ratio of the patch. This is also the choice made in the current study. The flexibility parameter is determined by equating the two solutions obtained from the linear complete theory and from the simplified theory for elliptical contact area and pure longitudinal, lateral and spin creepages. In addition, there are two options with respect to the choice of the flexibility parameter, namely one single weighted mean flexibility parameter or three flexibility parameters, one for each creepage component. According to paper [104], the

single flexibility parameter will reduce the agreement of FASTSIM to the exact theory. Therefore, three flexibility parameters are used in the current study.

It should be noted that the spin does not contribute to the longitudinal creep force when an elliptic contact patch is assumed. However, for non-elliptical especially the asymmetric contact patch, see Figure 3.11(b1) and Figure 3.13(b1), both the lateral creepage and the spin can produce longitudinal forces. To take this effect into account, a new tangential contact theory is required. One possible solution could be achieved by introducing four flexibility parameters instead of the three used originally in FASTSIM, for instance in [7, 64]. For the sake of simplicity, the original method proposed in the KP is used for solving tangential problem as described below.

From the main assumption of the linear theory which neglects slip in the contact zone, the tangential stress distribution is derived in the form:

$$\begin{cases} \tau_x(x,y) = \frac{\xi_x}{L_1} - y\frac{\xi_z}{L_3}(x - x_{xz}^l) \\ \tau_y(x,y) = \frac{\xi_y}{L_2}(x - x_{xz}^l) + \frac{\xi_z}{2L_3}\left(x^2 - (x_{xz}^l)^2\right) \end{cases} \tag{3.67}$$

where $\xi_i(i = x, y, z)$ are the longitudinal, lateral and spin creepages, and $L_j(j = 1 - 3)$ denotes the flexibility parameter for each creepage component.

The stresses stated in Equation 3.67 cannot exceed the so-called traction bound. Slip occurs in the region where the tangential stresses predicted by Equation 3.67 are greater than the traction bound. The formulation for the traction bound used in this paper is obtained by applying Coulomb's friction law locally with a constant friction coefficient, i.e. $\mu p(x,y)$. The tangential forces are obtained from the numerical integration of the stresses over the contact patch.

3.7 Comparisons between wheel-rail and wheel-roller contact

The effects of roller on the contact solution with respect to the wheel-rail case have been addressed in this chapter under four different points of view. In reality, all of these factors are interacting with each other, thereby it is essential to investigate their combined influence on the contact solution. To this end, a set of cases with various contact positions and radii of roller have been chosen to quantify the influence. The calculation parameters listed in Table 3.1 are used, in addition, the normal load is 80 kN, the rolling velocity is 72 km/h, the friction coefficient is 0.35, and the radius of roller is set to 0.5 m and 1.0 m, respectively, for the purpose of comparison.

For simplicity, track irregularities are neglected and no wheelset velocity component is considered except in the rolling direction. The creepages of the right wheel of the wheelset are calculated according to expressions 3.61-3.66 as presented in Table 3.3 where $\xi_i(i = x, y, z)$ represents the longitudinal, lateral and spin creepages. Two contact cases are considered for the central position of the wheelset on the track, i.e. $\Delta y = 0$ mm and a lateral displaced position of the wheelset with $\Delta y = 3$ mm.

It is clear that the major difference in the longitudinal creepage obtained in Table 3.3 is caused by the variation of the roller head circumferential velocity across its profile according to Equation 3.62. The lateral creepage is zero when the yaw angle is assumed to be zero according to Equation 3.64 under the considered contact condition. It can be seen from Equation 3.66 that the additional contribution of the roller rig to the spin creepage is from the effect of both the wheelset yaw angle and the angular velocity of

the roller. The contact estimation results are presented in two groups for normal contact solution and tangential contact solution, respectively.

Table 3.3: *Calculation cases for comparison between wheel-rail and wheel-roller contact*

No.	Δy [mm]	Rail			Roller s_0=1.0 m			Roller s_0=0.5 m		
		ξ_x	ξ_y	ξ_z[1/m]	ξ_x	ξ_y	ξ_z[1/m]	ξ_x	ξ_y	ξ_z[1/m]
1	0	0	0	0.075	0	0	0.109	0	0	0.143
2	3	-0.0017	0	0.197	-0.0022	0	0.287	-0.0027	0	0.377

The solutions of the normal contact problem in terms of the shape and area of the contact patch and the corresponding pressure distribution within the contact patch are obtained by the EKP model for wheel-rail and wheel-roller contact conditions, respectively. The calculation results for the case studies listed in Table 3.3 are presented in Figure 3.16, and the results of wheel-rail contact and of wheel-roller contact at the same contact position are presented in the same figure for comparison.
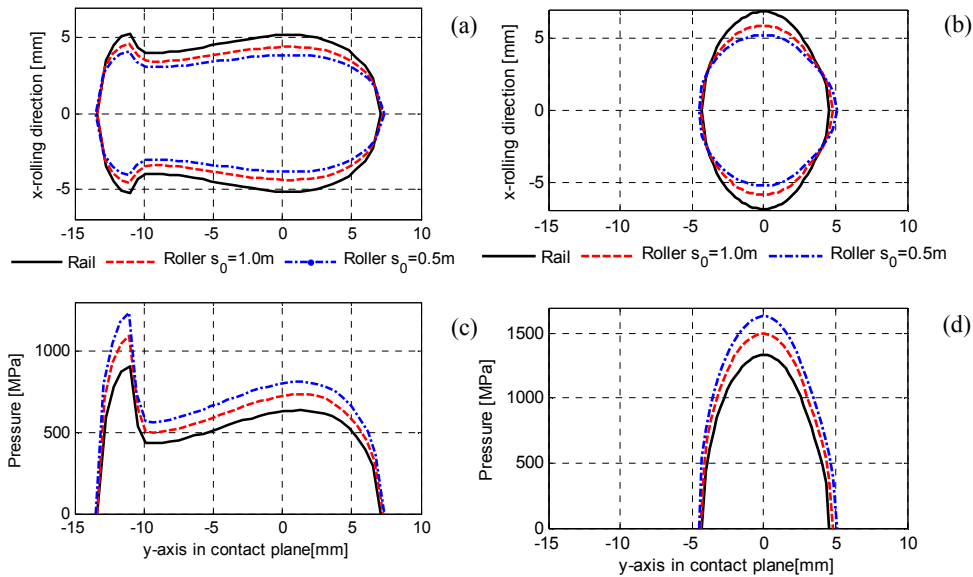
Figure 3.16: *Contact patch (top) and the pressure distribution along its y-axis (bottom) for Case 1 (left) and Case 2(right).*

It can be seen from Figure 3.16 that these two simulation cases correspond to a highly non-elliptic contact condition in the first case (left column) and nearly elliptic contact condition in the second case (right column), respectively. In Figure 3.16 (a) and (b), it is observed that the length of the contact patch in longitudinal direction decreases on the roller compared to the rail due to the finite radius of roller and this effect being more visible for the smaller value of the roller radius. On the contrary, the width of the contact patch is slightly increased in the case of wheel-roller contact. Eventually, the contact area of the contact patch decreases with the increase of the radius of the roller. The maximum contact pressure over the contact zone is increased by a decrease of the roller radius as the same load is spread across a smaller contact

area, see Figure 3.16 (c) and (d). The change in the contact patch also affects the semi-axis ratio and consequently the creep coefficient and the creep forces according to Kalker's theory. The differences caused by the roller rig in terms of the contact shape and contact pressure should be taken into account when the roller rig is used for contact deterioration mechanism studies such as wear and RCF.

The corresponding tangential contact solutions in terms of the stress distribution for the cases considered are presented in Figure 3.17.
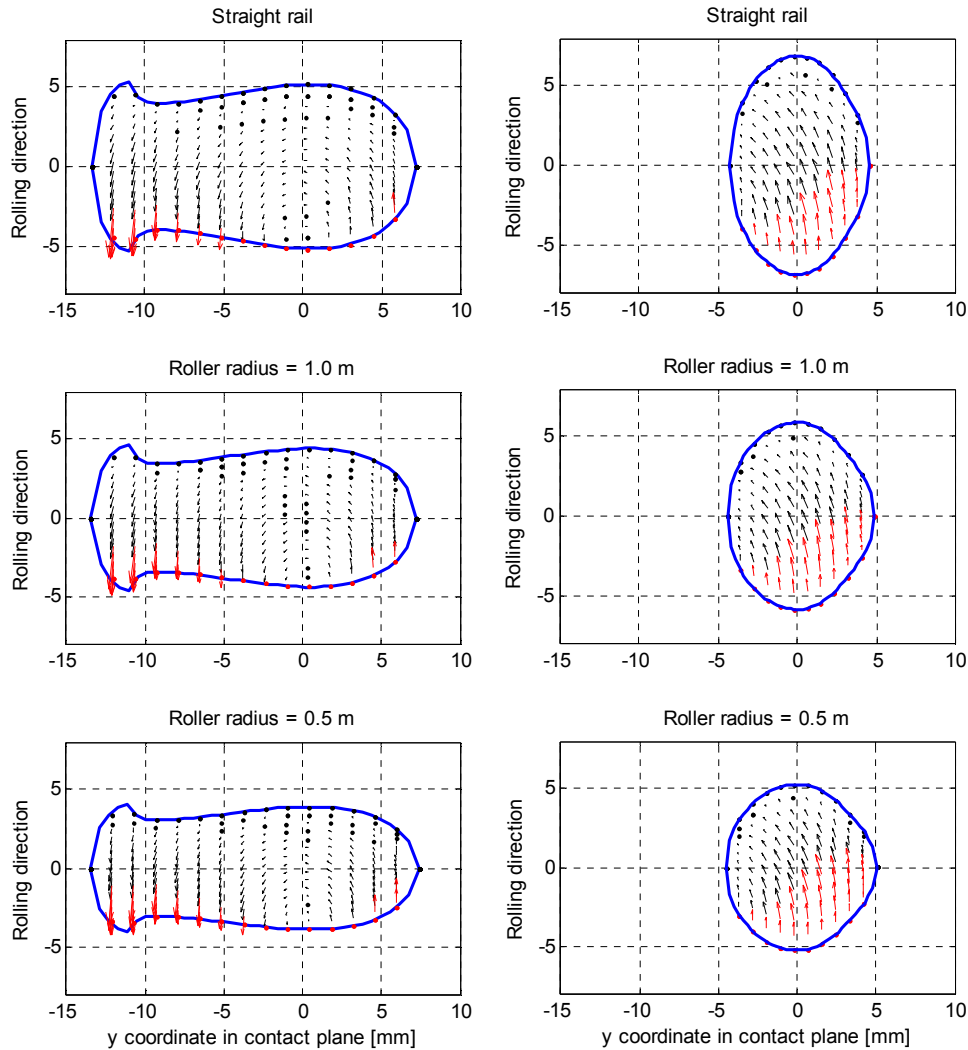
Figure 3.17: *Stress distribution over the contact patch formed by wheel-rail (top), wheel-roller with a radius of 1 m (middle) and wheel-roller with a radius of 0.5 m (bottom) for Case 1 (left) and Case 2(right). Black and red arrows represent the stress vector in the stick and slip regions, respectively.*

It can be observed from Figure 3.17 that the pattern of the stress distribution over the contact patch is similar for wheel-rail and wheel-roller cases. However, the division between the slip and stick regions in the contact patch varies case by case.

To quantify the differences involved in the contact solution between wheel-rail and wheel-roller contact for the cases considered above, the contact area, resulting longitu-

dinal force, lateral force, spin moment around the z-axis of the local coordinate system, the percentage of the slip region over the complete contact area, and the frictional power dissipated by the surface tractions within the contact patch are calculated as listed in Table 3.4.

Table 3.4: *Resulting figures of the contact problems listed in Table 3.3*

Figures	Case 1 ($\Delta y = 0mm$)			Case 2 ($\Delta y = 3mm$)		
	Rail	Roller$_{1m}$	Roller$_{0.5m}$	Rail	Roller$_{1m}$	Roller$_{0.5m}$
Contact area A_c [mm^2]	183	158	142	94	84	78
Longitudinal force [kN]	-4.67	-5.97	-6.32	16.46	17.03	17.87
Lateral force [kN]	-2.57	-2.96	-2.92	-5.70	-5.45	-5.65
Spin moment [Nm]	58.14	75.96	81.85	9.35	7.64	8.29
A_{slip}/A_c [%]	8.33	13.33	15.25	26.32	27.40	29.41
Frictional power [W]	87.21	165.58	234.10	608.50	847.42	1119.02

It is observed that when the rail is replaced by a roller with a radius of 1 m and 0.5 m, the contact area decreases by approximately 10% and 20%, respectively, for both cases. Correspondingly, the resulting longitudinal contact force increases approximately 28% and 35%, respectively, for Case 1 and 3.5% and 8.6%, respectively, for Case 2. The different variation in the longitudinal force between the two cases because Case 1 is a pure spin condition where the longitudinal contact force is only attributed to the spin, whereas the longitudinal creepage and spin both contribute to the resulting longitudinal contact force for Case 2.

Since there is no lateral creepage considered, the resulting lateral contact force completely comes from the contribution of the spin. Therefore, the resulting lateral contact force is relatively small, and the influence of the roller on its value is limited, as far as the lateral contact force is concerned.

The spin moment increases approximately 30% and 40%, respectively, when the rail is replaced by a roller with a radius of 1 m and 0.5 m, under the pure spin condition, i.e. Case 1. The inclusion of the longitudinal creepage in Case 2 reduces the magnitude of the spin moment even though the spin creepage increases with the reduction of the roller's radius, since the longitudinal creepage is dominant in this case, resulting in a reduction of approximately 18% and 11%, respectively, when the radius of roller is 1 m and 0.5 m.

The ratio of the slip area to the entire contact area is increased for both cases, and the increase is considerable for Case 1. Similar conclusions are applied to the frictional power dissipation by the surface tractions over the contact patch. The increase of the frictional power is approximately 160% and 80%, respectively, for Case 1 and Case 2 when the roller's radius is 0.5 m. The significant increase of the frictional power caused by the roller rig will affect the surface damage/deterioration of the wheel, e.g. wear and RCF, therefore, it must be taken into account for performing this kind of test on the roller rig. More details on this topic will be provided in Chapter 7.

MULTIBODY SYSTEM SIMULATION OF A ROLLER RIG AND A RAIL VEHICLE

4.1   Chapter summary

Modelling and simulation play an important role in roller rig application to railways as mentioned in Chapter 2, and in particular for single-wheelset roller rigs. They strongly complement the physical testing. On the one hand, because wheelsets are constrained by the vehicle suspension, the movement of the single wheelset on the roller rig is different from the actual behaviour of the wheelset on the track, unless appropriate references are fed to the roller rig actuators starting from the simulated/measured behaviour of a complete vehicle. This problem will be discussed in Chapter 6 for the case of a wheelset negotiating a curve. On the other hand, the numerical simulation of the test performed on the roller rig is also required for at least two reasons. The first one is to predict the results of the test, ensuring that these will meet expectations: in this way the complicated and resource consuming full-scale tests can be tuned and optimised before they are actually performed. Secondly, the comparison of experimental results with the simulation can be used to assess the accuracy of models and theories.

Therefore, it is the aim of this chapter to develop numerical models for the roller rig system and a complete rail vehicle separately, which will be used for further study in the following chapters where they are needed. To this end, the multibody system (MBS) simulation technique is selected to accomplish this task in this chapter.

4.2   Multibody system simulation in railway application

Multibody system (MBS) dynamics is a branch of the general field of computational mechanics that is concerned with developing and solving the non-linear equations that

govern the motion of complex physical systems [93]. MBS simulation is one of the key methods for the design, homologation and research in the field of railway vehicles. The complexity of modern rail vehicles requires an as deep as possible insight into the dynamics of the vehicles already in very early stages of their development. MBS simulation is able to avoid many costly measurements and tests as well as unwanted vehicle's behaviours when the vehicle is in service. Today nearly every newly developed rail vehicle, from tramcars to high-speed trains and from people movers to roller coasters, undergoes a thorough analysis by means of MBS simulation as a part of its design process [107]. For more details on the MBS simulation in railway application, the reader is referred to [93, 107].

A variety of MBS simulation packages is available for railway application in the market. Some of them are general purpose packages with rail modules, e.g. SIMPACK, VI-Grade and UM, while some other codes were especially developed for railway application e.g. VAMPIRE, NUCARS, GENSYS and VOCOLIN. Some interesting comparisons among the packages that are suitable for railway simulations were made in [44] and [107]. On the one hand, these commercial packages facilitate the work of railway engineers and researchers thanks to their powerful functions and friendly user interface. On the other hand, some details that are of interest to users are not available yet for confidential reasons. Therefore, in-house codes are also common as alternatives in research institutes due to their complete flexibilities, such as ADTreS developed by the Railway Dynamics Research Group at Politecnico di Milano in Italy and TPLDYNA at SWJTU in China.

4.3 Dynamics of a single suspended wheelset system

From a mathematical point of view, the dynamic behaviours of a system is governed by its differential equations of motion. In order to show the differences in the dynamic behaviour of a wheelset on a roller versus on a track, the equations of motion of a suspended wheelset on the roller and on the track are derived, respectively, in this section.

4.3.1 Equations of motion of a wheelset on rollers

The equations of motion of a wheelset placed on the rotating rollers encompass the essential features of the wheel-rail geometry, the frictional forces transmitting between the wheel and roller, and the elastic and damping forces generated by the suspension [108]. The wheelset is allowed to move in the yaw and lateral directions. Hence, the system can be considered as a two degrees of freedom (DOF) system and the two equations of motion describing its dynamics are: the lateral motion of the wheelset

$$m\ddot{y} + F_{yl} + F_{yr} + K_y y + C_y \dot{y} + \frac{mg\lambda}{l}y = 0 \tag{4.1}$$
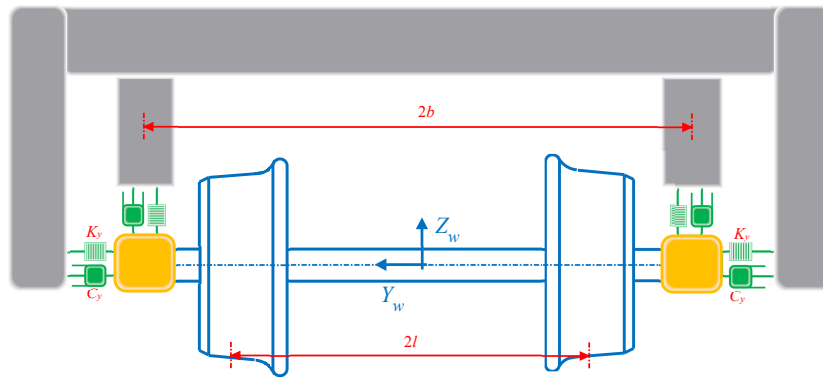
and the yaw motion of the wheelset

$$I_z\ddot{\psi} + b^2 K_x \psi + b^2 C_y \dot{\psi} + (F_{xr} - F_{xl})b + M_{zl} + M_{zr} - mg\lambda l\psi - M_{dc} = 0 \tag{4.2}$$

where y and ψ denote the lateral displacement and yaw angle of the wheelset, respectively, K and C represent the stiffness and damping of the primary suspensions, m and

I stand for the mass and moment of inertia of the wheelset, F and M are the contact force and spin moment, g is the gravitational acceleration, λ is the equivalent conicity of the wheel, l is the half distance between the contact points, b is the half gauge of the primary suspensions, and M_{dc} presents the moment caused by the so-called de-crowning effect of the roller rig. More details regarding this issue can be found in Section 4.4. In addition, the subscripts x, y and z refer to the directions of force and moment, and l and r refer to the left- and right-hand side of the wheelset. A schematic presentation of the single suspended wheelset system with symbols used in the equations is shown in Figure 4.1.

Figure 4.1: *A single suspended wheelset.*

The determination of the contact forces is the most challenging part to set up the equations of motion of the wheelset system, which can be done by the methods proposed in Chapter 3 or simply by Hertzian theory [42] combined with Kalker's linear theory [56].

4.3.2 Equations of motion of a wheelset on a track

The equations of motion of a suspended wheelset on the track have a similar form to that on a roller rig as presented in Equations 4.1–4.2 except the term of M_{dc} which is only applicable to wheel-roller contact case. There is no need to repeat the equations once more here, while it is worth mentioning that there are two main aspects responsible for the differences of the dynamic behaviour of the wheelset on the track versus on the roller rig governed by these equations. The first is the different creep coefficients which depend on the size and dimension of the contact patch resulting in different creep forces, and the second is an effective increase in the equivalent conicity λ for a wheelest running on rollers resulting in the increase of the magnitude of the gravitational angular stiffness, which can explain that the critical speed of a wheelset running on the roller rig is generally lower than on the track.

4.4 MBS model of a roller rig system

The expressions of the dynamic equations of motion of a wheelset on rollers and a track presented in preceding section are helpful for understanding the sources of the differences of the two systems in terms of the dynamic behaviour. It is concise and

straightforward but too simple to be applied for further study such as a virtual test. Therefore, a more detailed MBS model of a roller rig system is developed in SIMPACK in this section. The roller rig for the simulation purpose in this thesis specially refers to a full-scale roller rig for a single wheelset test unless otherwise stated. Figure 4.2 presents a typical layout of this kind of roller rig under consideration. The complete roller rig consists of a mechanical system and an actuation system which are simulated together.
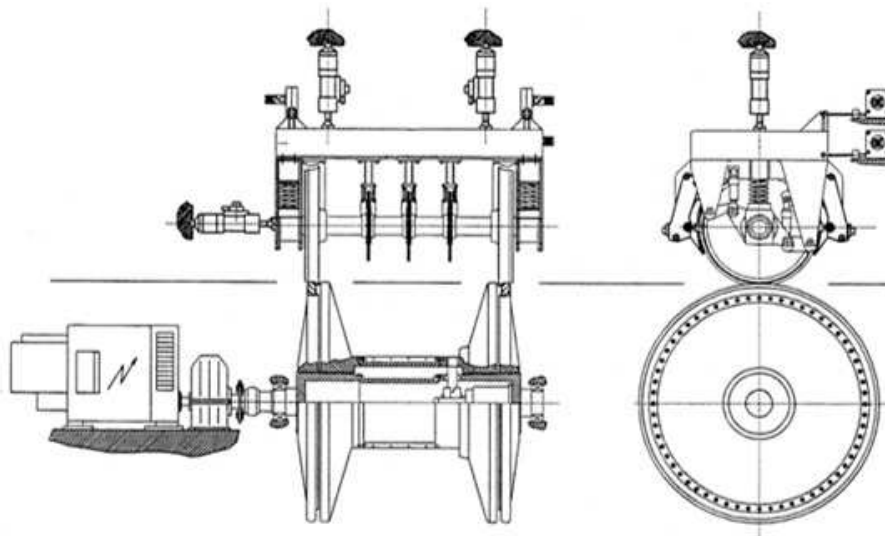
Figure 4.2: *Mechanical layout of a roller rig for tests on a single wheelset.*

4.4.1 Roller rig mechanical system modelling

The MBS model of the roller rig mechanical system consists of six rigid bodies with 13 state variables and two constraints as shown in Figure 4.3 (left). The portal frame is fixed to the inertial frame and connects to the half-bogie through actuators. The half-bogie has four DOFs, namely the vertical and lateral translations plus yaw and roll rotations. It connects to the axle boxes through the primary suspensions. The contact between the wheelset and the rollers introduces two degrees of constraint in the system, hence, the wheelset has four DOFs which are longitudinal and lateral translations, and yaw and pitch rotations. The roller (assumed to have a radius of 1 m) can only rotate about its axis of revolution. The typical wheel and rail combination S1002/UIC60 with the rail inclination 1:40 and 1435 mm track gauge are used. The normal contact force is evaluated according to Hertzian theory, while the tangential contact force calculation is implemented according to the FASTSIM algorithm [56] with a constant friction coefficient of 0.5. The additional creepage terms related with the rotation of the roller [47] are considered.

The MBS model of the roller rig also accounts for the de-crowning phenomenon [4, 34] that occurs when the wheelset performs a yaw rotation respective to the rollers, resulting in a component of the normal force in the horizontal plane which in turn leads to a de-stabilising yaw moment applied on the wheelset as illustrated in Figure 4.3 (right). Since de-crowning is not taken into account in the SIMPACK version [97] used

to defined the model, this effect is introduced as an additional yaw moment which is applied on the MBS model via co-simulation with SIMULINK according to Equation 4.3 derived from references [4, 34]:

$$M_{dc} = \frac{N l^2 \psi}{r_0 + s_0} \tag{4.3}$$

where N is the sum of normal force components on the left and right wheels, and r_0 and s_0 are the nominal radii of the wheel and roller, respectively.
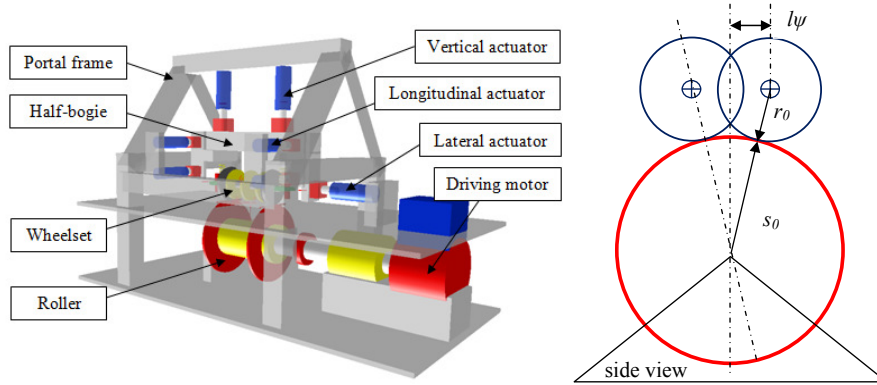

Figure 4.3: *MBS model of roller rig (left) and the de-crowning effect (right).*

4.4.2 Roller rig actuation system modelling

The roller rig actuation system consists of multiple modules accomplishing different tasks:

1. a vertical actuation module, consisting of two actuators producing a desired combination of vertical forces on the two sides of the half bogie;

2. the lateral actuation module, consisting of a single actuator which is used to apply a lateral force on the half bogie;

3. the yaw actuation module, which is used to control the yaw rotation of the half-bogie. This module may consist of a variable number of actuators (4 in the scheme of Figure 4.2), depending on the specific mechanical layout adopted in the design of the rig;

4. a traction module, driving the rollers according to a desired speed profile;

5. the differential gear module, driving the two rollers in different speeds by an additional motor via a differential gear.

Modules 1 and 2 are typically operated in force control mode, whereas module 3 is normally operated in position control and module 4 in speed control. Based on the author's knowledge, at least for the BU300, KRRI and CARS benches, the references of actuation modules 1, 2 and 3 can be defined in various ways which include manual control by a human operator, the execution of a sequence of simple waveforms such as

ramps, holds, sinusoids or generic time histories that are generated externally and fed to the control system prior to the execution of the test. Module 5 is based on a modified design of the roller rig specially for curving test. More details the application of this module will be given in Chapter 6.

Considering a similar configuration of actuation system of the BU300 rig, the mathematical model of the actuation system assumes hydraulic actuation for the vertical and lateral actuation modules and electro-mechanical actuation for the yaw actuation, traction and differential gear modules.

A third-order dynamic model is introduced for each hydraulic actuator in the vertical and lateral actuation modules. According to the characteristic equations of hydraulic actuators, the numerical model is defined in SIMULINK, see Figure 4.4. Equation 4.4 represents the dynamic response of the servo valve, where x_k is the position of the valve, i_k is the input exciting current, G_{vm} is the current gain, and σ_v and ξ_v are the valve natural frequency and damping factors, respectively. Equation 4.5 describes the fluid continuity equation, where P_k is the difference of pressure between the two chambers of the actuator, A is the area of the piston, V_0 is the initial volume in the two chambers of the actuator, β is the fluid compressibility coefficient, C_{ep} is the total leakage coefficient, K_c is the flow-pressure coefficient relating the flow rate to the difference of pressure P_k , K_q is the valve flow gain relating the flow rate to the position of the servo valve x_k, y_{hyd}, k is the physical displacement of the actuator (cf. [23] for more details).

$$\frac{1}{\sigma_v^2}\ddot{x}_k + \frac{2\xi_v}{\sigma_v}\dot{x}_k + x_k = G_{vm}i_k \tag{4.4}$$

$$\frac{V_0}{2\beta}\frac{dP_k}{dt} + \left(\frac{C_{ep}}{2} + K_c\right)P_k + A\frac{dy_{hyd,k}}{dt} = K_q x_k \tag{4.5}$$

A PI regulator is adopted in the hydraulic actuator control loop. This control strategy is chosen in order to obtain small errors for constant reference values (as happens in steady state curving) together with low noise sensitivity. As mentioned above, the electro-mechanical actuations are assumed for yaw actuation, traction and differential gear modules. Therefore, they are treated as ideal actuators in the model. PI regulators are also adopted, neglecting actuators' dynamics on account of the much larger passband and accuracy of these actuators, resulting in a lower complexity of the overall model for the actuation system.
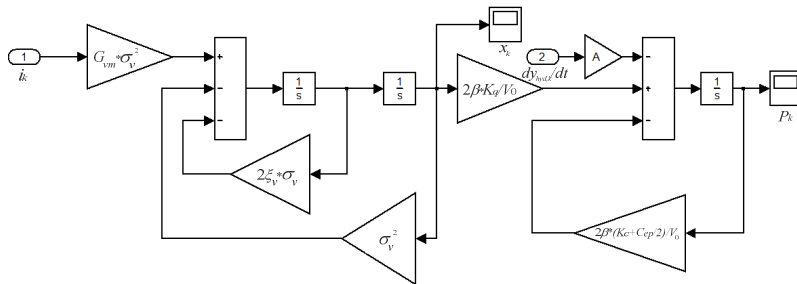

Figure 4.4: *Hydraulic actuator control loop in SIMULINK.*

4.5 MBS model of a rail vehicle

To define the dynamic behaviours of the wheelset on the roller rig and further compare with that on a real track under operational conditions, a complete rail vehicle model is needed. An MBS model of a high-speed rail vehicle with two suspension's stages is developed in SIMPACK based on the high-speed Italian train ETR470, as shown in Figure 4.5. The model consists of a set of rigid bodies including a carbody, two bogie frames, four wheelsets, and eight axle-boxes as well as suspension components. The non-linearities of the suspensions and wheel-rail geometry contact are taken into account as with the roller rig. The same parameters as the roller rig model are used for wheel-rail contact geometry and contact force calculation.
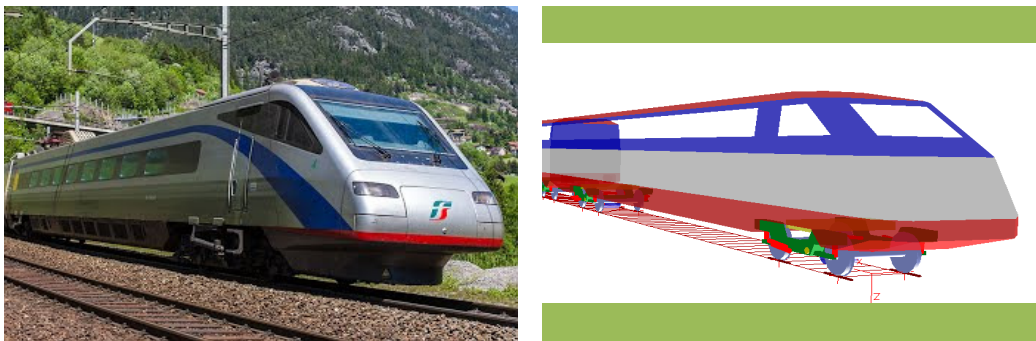
Figure 4.5: *ETR470 on track (left) and its MBS model (right).*

It should be mentioned that the parameters of the vehicle's suspension system are not necessarily the same as those of the roller rig. In addition, the configuration of the vehicle model may need to be adjusted, depending on the test type being considered. This vehicle model was validated by comparison with the results presented by S. Bruni *et al.* in reference [23].

PROCEDURE FOR TESTS ON A SINGLE-WHEELSET ROLLER

5.1 Chapter summary

To test any new applications or designs for improving railway performances, e.g. new concept suspension system and optimizing the match of profiles or materials of the wheel and rail, and devising methods of detecting defects on a roller rig, the leading-edge testing methods are required [100]. Due to the inherent differences of the roller rig test compared with field test, the testing procedure and the underlying test principle and method on a roller rig are of particular importance to an efficient and successful test. A general testing procedure for a wheelset on a roller rig will be described in this chapter based on a detailed discussion on the testing method and principle for using a full-scale roller rig.

5.2 Testing principle of roller rigs

The testing principle of a testing facility is of importance to a successful representation of the real operating conditions which shall be reproduced by the experiment. The roller rig simulates the motion of the wheel on the endless track by the motion on rollers. The most common method to reproduce wheel-rail contact on roller rigs can be classified as Hertzian simulation and Geometrical simulation [65].

In Hertzian simulation principle, the average or maximum contact stress, based on the Hertz theory, are simulated with pre-calculated curvatures of wheel and roller profile and dimensions, and the contact ellipse produced by the rig has the same ratio of axis with the actual wheel and rail combination to be tested, which ensures the similarity of the property of friction interaction, thus, effectively simulating the stress distribution

Figure 5.1: *TNO-TPD test rig (left) and its concept presentation (right).*

between wheel and rail under field conditions, but the details of the wheel and rail profiles are neglected. Therefore, this kind of test rig is mainly used for contact study rather than for the investigation of vehicle dynamics. The most common test rig of this kind is a disc-on-disc rig such as the one located at TNO TPD in Delft (see Figure 5.1). The set-up consists of two wheels, one a scale-model (1:3.68) of a wheel and the other representing the rail called wheel-rail or roller. The effect of the limited radius of roller on the contact patch is compensated by adjusting the lateral radius of the roller. Another example of the roller rig using Hertzian simulation principle is the JD-1 rig at Tribology Research Institute in SWJTU, China [74]. It has been used to study rail corrugation in particular, and rail-wheel adhesion behaviour in general.

For Geometrical simulation principle, the actual or scaled profiles of wheel and rail are precisely ground. This type of simulation provides a complete description of wheel-rail geometric contact relationship and of all the important forces including flange contact, for both tangent and curved track conditions. The common configuration of this kind of facility can be found in a variety of forms, such as the 1:5 scaled roller rig originally built at MMU (now at IRR in the University of Huddersfield) in the UK, another similar one at Politecnico di Torino (PoliTo) in Italy, see Figure 5.2, the roller rig for tests on a full-scale bogie at NTSEL in Japan, and the six-axle full-scale roller rig for tests on complete vehicles at SWJTU in China, see Figure 2.1 in Chapter 2.
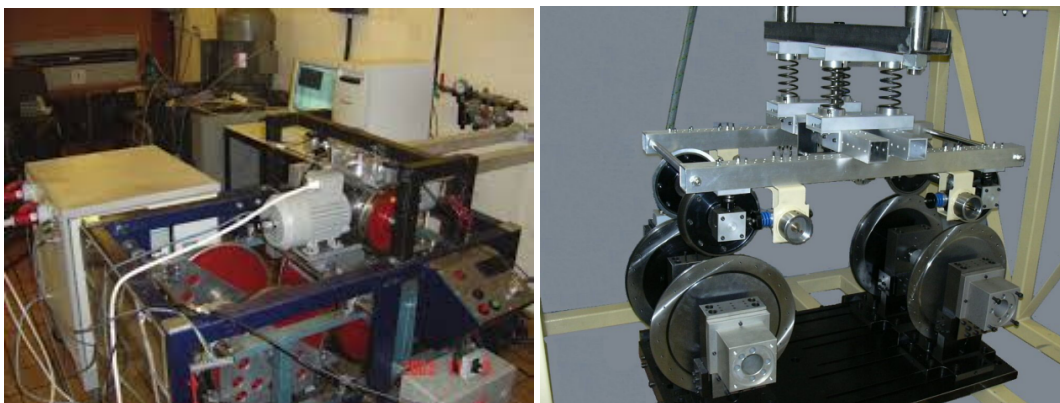
Figure 5.2: *The roller rigs at IRR (left) and PoliTo (right).*

There is another kind of roller rig belonging to this category, which is a compromise between the complexity and cost of the complete vehicle test rig and the similarity of the reduced scale roller rig. Such sort of roller rigs are designed for a single full-scale wheelset test, as the BU300 rig at Lucchini RS in Italy and the RaSSP roller rig owned by DB Systemtechnik in Germany, see Figure 1.1. As mentioned before in Chapter 1 and Chapter 2, this kind of roller rig is the main study subject in this thesis, therefore the following discussions are mainly based on this specific test rig configuration.

Basically, both the Hertzian and Geometrical simulation principles are able to simulate the wheel-rail contact stresses, however, the change of geometrical relationship by employing the Hertzian simulation makes it impossible to simulate flange contact condition and wheel-rail geometric contact condition. Consequently, it fails to reproduce the contact force and wear on the flange and dynamic behaviour of the wheel related to the variation of wheel and rail profiles. Therefore, this testing principle is particularly applicable to reduced-scale roller rig or single wheel-on-wheel rig for simplicity. In contrast, Geometrical simulation is capable of reproducing the contact condition between wheel and rail with a good approximation in terms of contact geometry as well as contact stresses especially for full-scale roller rigs, although the semi-axis ratio of the contact patch slightly differ from the field condition. The details about the advantages and disadvantages of using different types of roller rigs for railway application are discussed in [79].

5.3   Testing procedure

The testing procedure of a roller rig in laboratory may differ slightly for each specific test, but the main steps remain the same for the roller rigs with similar configurations. Generally, the test on a full-scale roller rig can be run in the following four modes of operation:

1. Set-up mode;

2. Manual mode;

3. Sequence-based mode;

4. Time history-based mode.

Modes of operation 1) and 2) are *manual* modes, which means the operation of the roller rig is directly controlled by the user, although the roller rig control unit can be used to reduce the risk of improper use, e.g. by implementing time constants/ramps to avoid the abrupt change of forces and displacements applied by the actuators, and by introducing appropriate warning and alarm thresholds.

Modes of operation 3) and 4) are *automated* modes, which means a sequence of operations is defined by the user and then executed automatically on the test rig. The difference between the *sequence-based* and *time history-based* modes is that in the first case the variation of the references to the actuators is defined using simple time waveforms such as *ramps* and *holds*, whereas in the second case general time histories are defined for the references. Therefore, a reference generator is required in mode 4) for providing control signals to the control unit since the aim of this test mode is mainly to reproduce the realistic condition of a wheelset running on the track.

The whole testing procedure for a single wheelset roller rig can be divided into three phases similar to the approach proposed in reference [20, 65] namely the preparatory phase, followed by the trial phase in which the operation mode should be chosen, and finally the post-processing phase.

Firstly, thoroughly clean the surfaces of the wheels and rollers, measure the profile shapes and hardness of the surfaces prior to commencing new tests which is so-called preparatory phase. After these preparations are completed, the operation mode should be selected. For instance, if mode 4) is selected, the loading will be commenced by actuators in the following sequence provided that all references (time history-based) of control unit are ready. A general loading sequence is presented in Figure 5.3.
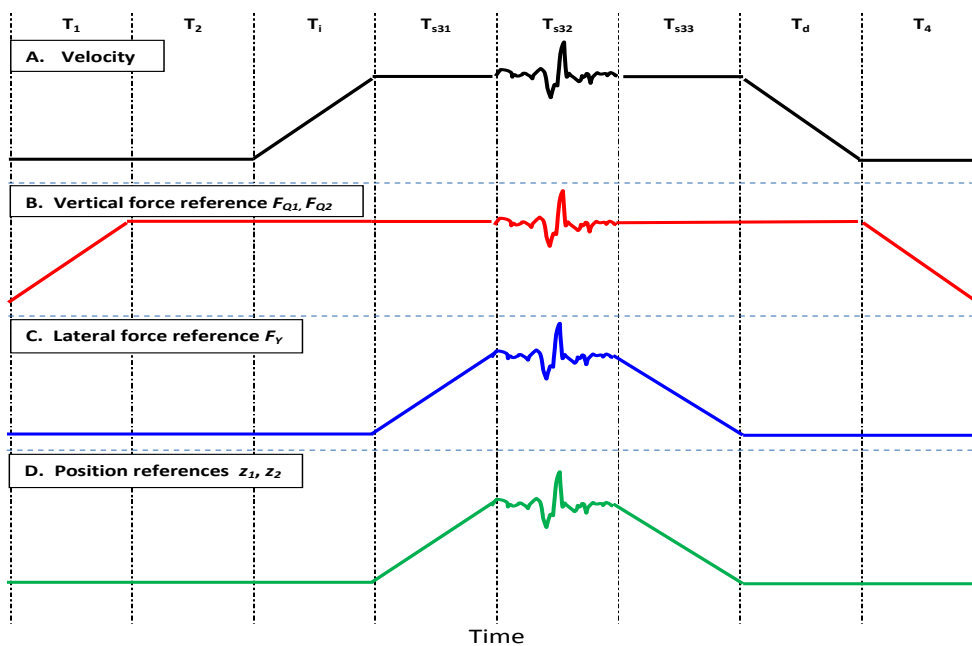
Figure 5.3: *Loading sequence on a roller rig.*

The wheelset is first lowered to just come into contact with the roller at the central position. As the load is being applied, the monitor system continually samples the load values. To achieve a certain loading condition, the vertical load is increased to the needed value without any unloading as shown in section T_1 of the curve **B** in Figure 5.3. This keeps the loads accurate in value (see section T_2 of of the curve **B**). After ensuring that the vertical load is correct, the roller is driven to the desired test speed as shown in section T_d of curve **A** in Figure5.3. Meanwhile, the excitations may be applied by actuators such as the case shown in section T_{s31} of curves **C** and **D** in Figure 5.3, representing the external forces and constraints applied on the roller rig.

The following parameters are constantly monitored during each test:

- vertical, lateral and longitudinal loads by taking the load cell readings from the computer,

- speed of the roller and wheelset,

- lateral displacement and yaw angle of the wheelset,

54

- contact forces by dynamometric wheelset and/or roller,

- any unusual phenomena like excessive vibrations, corrugations, noise, temperature, etc.

After the predefined cycles of revolutions or steps are completed, the excitations applied by the actuators are removed gradually (section T_{s33} of curves **C** and **D**). Then the speed of the roller is gradually reduced till the roller is completely stopped as shown in section $T_d - T_4$ of curve **A** in Figure 5.3. The vertical load is then released, and the profiles of the wheel and roller are again measured. Then the test comes into final post-processing state including data collection and analysis, report generation etc.

5.4   Generation of references for the actuators

It can be seen from the preceding section that the roller rig enables a railway wheelset to be tested under various conditions with a suitable reference. Therefore, the core of this testing procedure in preparatory phase is to generate the control reference signals. Generally, two methods can be used to accomplish this task depending on different control objectives, namely the physical-based method and theoretical-based method. The difference of the references obtained from each method is attributed to the different feedback used in the control loop, see Figure 5.4. More details will be introduced in sequence.
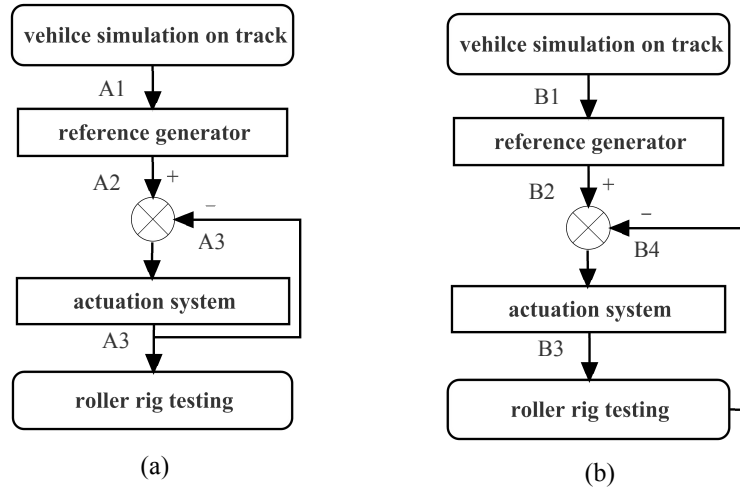
Figure 5.4: *Scheme of reference generation: (a) the physical-based method, and (b) the theoretical-based method.*

5.4.1   The physical-based method

The method shown in Figure 5.4(a) definitely adheres to the real physical system. The feedback directly comes from actuator, which can be force or stroke of the cylinder depending on the working mode of actuators. A good example of this application is given by S. Bruni *et al.* in paper [23].

While the accuracy of this method is shown to be case dependent for curving test [72, 73]. As discussed in Chapter 3, the curvature of the roller of a test rig affects not

only the size of the contact patch and the distribution of the normal pressure but also the creepages and tangential tractions. The initial deviation arises mainly from differences in the dynamic behaviour of the wheelset running on the test rig compared to the same wheelset running on the track. In order to fully reproduce the contact condition between wheel and rail on the roller rig, especially the contact forces, the references obtained above need to be further corrected, more details will be given in Chapter 6. It should be noted that the numerical models of the control unit is not required for reference generation in this case, but they are necessary when a correction loop is introduced. One program has been developed for the roller rig at CARS for commissioning test based on this method.

5.4.2 The theoretical-based method

This method is not consistent with the physical system, only aiming at controlling the contact forces produced on roller with the contact references from track simulation as depicted in Figure 5.4(b). The method is possible in theory, but hardly feasible in practice due to its extremely high reliability requirements for control unit and measurement unit. Therefore, it is difficult to obtain converged results even in numerical simulation.
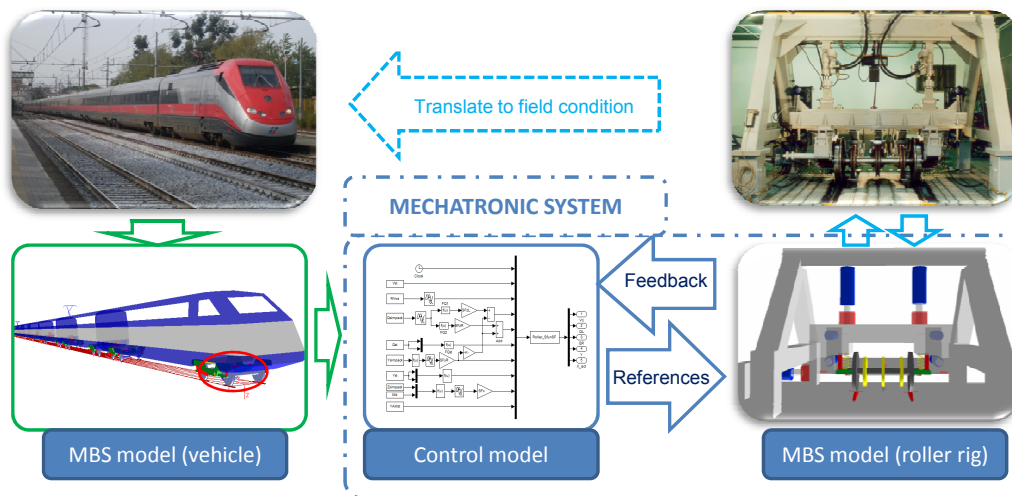
Figure 5.5: *Architecture of the virtual test on a full-scale roller rig.*

5.5 Virtual test of a roller rig

It is clear from the discussion above that a numerical model of the roller rig system is of importance to define the control references for running a test on a single wheelset roller rig. Moreover, a numerical implementation of the testing procedure called virtual test is a very important complement and extension to the physical test. Firstly, it can be used to design, select and optimize the testing programmes. Secondly, it is useful for checking the safety and feasibility of a physical test to be performed. Thirdly, it can provide a first prediction for the test result. If the virtual test model is validated for certain typical manoeuvres on the roller rig, the extrapolation to simulation scenarios going beyond the possibilities of the rig will be possible. Fourthly, the control laws

developed for the virtual test can be adopted to the physical test case [41]. Last but not lest, it can be used as a tool for post-processing, e.g. comparisons between theoretical and experimental results.

The virtual test of a roller rig is achieved by means of the co-simulation of an MBS roller rig model and different mathematical models for each actuation module (defined in Chapter 4). The schematic presentation of the complete process of the co-simulation applied to perform the virtual test simulation is described in Figure 5.5.

As shown in Figure 5.5, the references for the roller rig actuators are defined based on the simulation results of a complete railway vehicle based on the physical-based method. The mathematical model of the roller rig is inherently a multi-physic model, as it needs to incorporate both a mathematical description of the roller rig as a mechanical MBS and a model of the different actuation modules in the rig, which are either electro-mechanical or hydraulic systems.

Two specific test concerning curve negotiation and wheel wear will be described in detail in Chapter 6 and Chapter 7 within the framework introduced in this chapter.

CHAPTER 6

CURVING TEST ON A ROLLER RIG

6.1 Chapter summary

Curving performance is one of the most importance evaluation criteria for a rail vehicle, while the field experiment on rail vehicle curving negotiation can prove to be challenging due to the difficulties in adequately controlling the test conditions. Therefore, the curving testing study in laboratory is of interest to railway engineers and operators, nevertheless, the achievements are still limited due to the complexity and difficulty involved in this problem, such as the difficulties in recreating the centrifugal forces experienced by a vehicle passing a curve and the complexity of dynamically manoeuvring the test rigs. Some attempts have been made to deal with this issue, for instance, a specific curved track simulator was set up at the National Research Council in Canada and a complicated curving simulation mechanism designed for a complete vehicle test rig have been used in the laboratory of SWJTU in China [115]. Nevertheless, it is rare to find the information about curving test on a single wheelset roller rig in the literature and actually some doubts have been raised concerning the ability of this kind of roller rig to effectively reproduce the running dynamic behaviour of a wheelset on a curve [17, 79].

The objective of the curving test may be various in reality based on different research aims. It is assumed that the objective of this test is to reproduce the contact forces generated at the wheel-rail interfaces of a wheelset mounted on a complete vehicle running on a curve by the roller rig. The aim of this chapter is to show that realistic running conditions can be achieved on a roller rig even for the curve negotiation scenario by introducing more advanced methods for the definition of the actuators' references, especially in the case when the roller rig is equipped with a differential gear.

6.2 Configuration of the roller rig for curving test

In the existing implementations of roller rigs for a single wheelset, the two rollers are rigidly connected and actuated to rotate at the same angular speed. In this section, besides this base arrangement of the traction module, a modified design is considered which includes a differential gear with the purpose of having slightly different angular speeds of the two rollers. It should be noted that such an arrangement is at present not used in any of the existing roller rigs of this kind, however it is used in some scaled and full-scale roller rigs for tests on bogies or vehicles [54, 77, 115]. Therefore, it is interesting to investigate the improvements in terms of replication of curving that are enabled by this layout of the test rig, which is aimed at better controlling the longitudinal creepages at wheel-roller contact.

As shown in Figure 6.1, the modified configuration of the traction module includes a main motor that drives the input shaft of the differential gear according to a reference time history defined for the mean angular speed of the two rollers and a secondary motor that realises the speed difference between these two rollers. The rotation of the two rollers at slightly different angular speeds can be used to simulate the different curvature of the inner and outer rail in a curve and, more in general, to modify the longitudinal creepages on the two wheels which will in turn affect the longitudinal contact forces generated by the wheelset during the test, eventually leading to a better match of the contact forces to their targets.
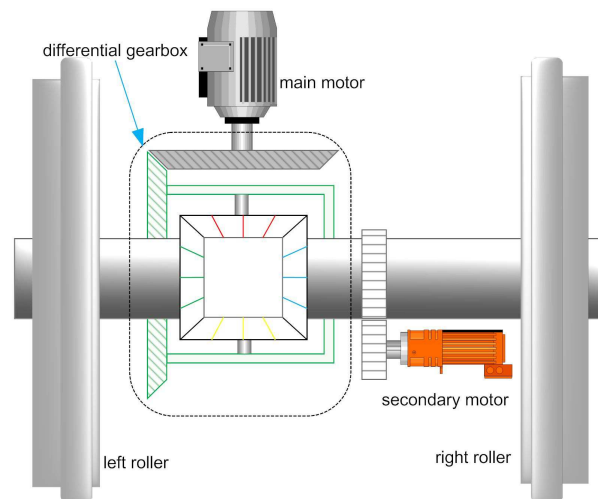
Figure 6.1: *Scheme of the traction module including a differential gear.*

6.3 Testing methodology

The method is backed by the use of the mathematical model of the roller rig developed in Chapter 4 and uses an iterative correction scheme, comparing the time histories of the contact force components from the roller rig test as predicted by the mathematical model to a set of target contact force time histories coming from the numerical simulation of the complete vehicle model also defined in Chapter 4. Two correction methods

are introduced to perform the iterative correction of results, the first one considering a standard arrangement of the roller rig, the second one assuming that a differential gear is introduced in the existing rig, allowing to differentiate the rolling speed of the two rollers.

The different actuation modules need to be operated in close interaction one with the other, in order to reproduce realistic testing conditions for the wheelset. This is achieved starting from some target time histories of the contact forces and of the wheelset angle of attack that are representative of the running condition considered. These are used to define suitable time histories of the references for the different actuation modules, with the final goal of minimising the difference between the target contact forces and those actually obtained during the test.

The simplified method proposed in [23] is based on a quasi-static balance of the forces acting on the wheelset and half beam, which is not satisfactory especially for the scenario of a vehicle running through a curve.

In this thesis, an improvement of the method proposed in [23] is introduced, consisting of applying some correction factors defined according to the original method, to compensate for the different contact conditions occurring on the roller rig compared to a line test, as shown in Chapter 3.

The correction factors are defined iteratively with the aim of minimising some measure of the difference between the target contact forces and those obtained on the roller rig. To estimate the contact forces obtained in a test on the roller rig, the MBS model of the roller rig defined in Chapter 4 is used.

In order to run the simulation as close as possible to reality, the physical-based reference generation method described in Chapter 5 is applied. The process for the definition of the correction factors is illustrated by the flowchart in Figure 6.2: starting from the target time histories of the contact forces and angle of attack, a first approximation of the time history of the actuator references $R_{i,1}$ is defined according to the simple method proposed in [23]. Here subscript i denotes the actuation module considered with $i = 1 - 5$ for left vertical, right vertical, yaw, lateral and differential gear respectively.

These first approximation references are used to initiate the iterative process shown in Figure 6.2: the actuator references defined at iteration j are used as the inputs to perform a numerical simulation of the wheelset dynamics on the roller rig according to the multi-body model presented in Chapter 4. The simulation results are compared to the target time histories of the contact forces and deviations $\Delta E_{k,j}$ are computed at iteration j for each k-th target contact force component for $k = 1 - 6$ corresponding respectively to the vertical, lateral and longitudinal on the left and right side wheel of the wheelset. The definition of the deviations $\Delta E_{k,j}$ is given by:

$$\Delta E_{k,j} = \frac{\mu(y_{k,j}(t) - y_k^{ref}(t))}{\mu(y_k^{ref}(t))} \times 100\% \tag{6.1}$$

where $\mu(\cdot)$ denotes averaging over time, $y_{k,j}(t)$ is the time history of the k-th output from the roller rig at j-th iteration and $y_k^{ref}(t)$ is the corresponding target time history.

Next, the value of the correction factors $F_{i,j}$ are defined based on the deviations obtained, and a new time history of the actuator references is obtained by applying the

correction factors on the previous time histories:
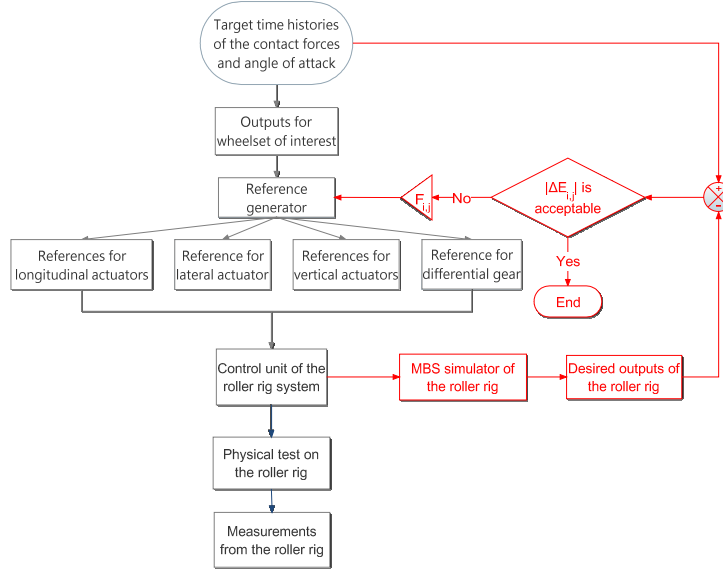
$$R_{i,j+1}(t) = R_{i,j}(t)F_{i,j} \tag{6.2}$$

Figure 6.2: *Flowchart of the correction procedure.*

The procedure is iterated until all deviations $\Delta E_{k,j}$ fall within an acceptable tolerance. In this way, the proposed methodology attempts to control the differences in the contact forces in a roller rig test compared to the target, relying on a multi-body model of the roller rig. It is worth noting that the model is able to work in batch mode which makes it possible to invoke each subsystem automatically.

Different possible ways of defining the correction factors $F_{i,j}$ are proposed in the following sections, depending on the objectives of the test to be performed.

6.3.1 Partial correction

Previous research [73] has proven that it is difficult to reproduce on a single wheelset roller rig the time history of all components of wheel-rail contact forces during a significant running condition of the vehicle. In particular, due to the rigid connection of the two rollers the longitudinal creepages occurring on the two wheels cannot be controlled independently. In this method, corrections are only applied on the references fed to the vertical, lateral and yaw actuation modules, therefore $i = 1 - 3$. This method is suited to reduce the deviation of the vertical and lateral forces on the left and right wheel, but it does not allow controlling the deviation of the longitudinal contact forces with respect to their reference value. However, the longitudinal component of contact force can be compensated by a suitable estimation formula which is introduced in Section 6.4. Therefore, targets $y_k^{ref}(t)$ are defined for $k = 1 - 4$ corresponding respectively to the vertical and lateral contact force on the left and right wheel.

It should be noted that only the sum of the lateral contact forces of the left and right wheels can be directly controlled by the lateral actuation system due to the rigid

connection of the wheels established by the solid axle, whereas the distribution of the lateral contact forces on the two wheels depends on the creepage conditions of the wheelset and can be controlled by adjusting the yaw angle of the wheelset.

In this way, the correction factor for the i-th actuation system only depends on the deviation $\Delta E_{k,j}$. The correction factors are therefore introduced according to Equation 6.3.

$$\underset{i=1-3}{F_{k,j+1}} = \begin{cases} a^{\frac{\Delta E_i}{c}} & \text{if} \quad \Delta E_i > \varepsilon; \\ b^{\frac{\Delta E_i}{d}} & \text{if} \quad \Delta E_i < -\varepsilon; \\ 1 & \text{if} \quad |\Delta E_i| \leq \varepsilon. \end{cases} \tag{6.3}$$

with

$$\begin{cases} \Delta E_1 = \Delta E_{1,j}; \\ \Delta E_2 = \Delta E_{2,j}; \\ \Delta E_3 = \max(\Delta E_{3,j}, \Delta E_{4,j}). \end{cases} \tag{6.4}$$

where $F_{i,j}$ represents correction factor with an initial value of one which is applied on each reference as a multiplier, and ε is a given tolerance, coefficients $a > 1, b < 1, c$ and d are positive constants which can be determined by trial and error based on the initial deviations before correction. The choice of these coefficients has an influence on the rate of convergence.

6.3.2 Optimal correction

In order to tackle the difficulties mentioned in preceding section, an optimal correction strategy is proposed. Better results can be expected by a roller rig including a differential gear in the system actuating the rollers, so that it is possible to drive the two rollers to rotate at slightly different speeds, with both speeds defined by the control system. In this section, a correction strategy is elaborated under the assumption that such additional device is included in the test bench, with the aim of ensuring a good agreement of the longitudinal contact forces to their target while keeping the good match on the lateral and vertical contact forces.

In this case, a different correction method is proposed, by which the correction factors are iteratively determined so to minimise a figure of merit J defined as the Euclidean norm of deviations $\Delta E_{k,j}$ for $k = 1 - 6$ corresponding to the vertical, lateral and longitudinal contact force components on the two wheels. The correction factors are introduced for all five actuation modules $i = 1 - 5$ for left vertical, right vertical, lateral, yaw and differential gear respectively. Therefore, the problem of finding the correction factors F_i can be stated as:

$$J(F_1, \ldots, F_5) = \sqrt{\sum_{k=1}^{6} \Delta E_{k,j}^2} = min \tag{6.5}$$

The initial value of correction factors are [1, 1, 1, 1, 0], respectively, for $i = 1 - 5$ corresponding to no correction state of the reference, together with a rigid rotation of the rollers. When the optimisation problem presented in Equation 6.5 is solved, the correction factors which are the variables in this problem are obtained simultaneously.
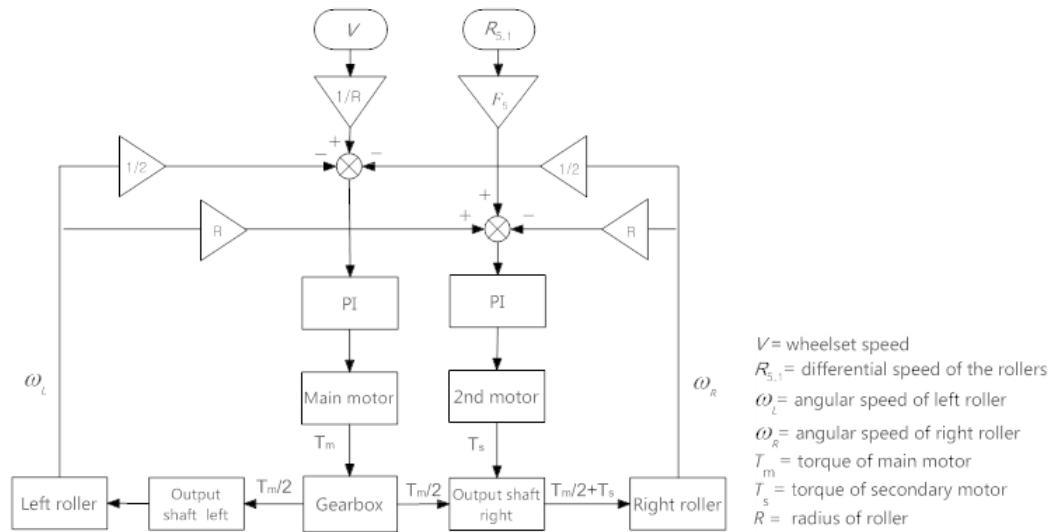
Figure 6.3: *The application of differential gear element.*

The schematic presentation of the correction on the modified layout of the roller rig is shown in Figure 6.3. The reference of the main motor is the wheelset speed, whereas the reference of the secondary motor is the desired differential speed of the two rollers, which is subject to the correction factor F_5, cf. Equation 6.5.

It is worth pointing out that this approach can also be applied on the conventional roller rig without differential gear, but the optimal results depend on the test conditions and test specimen. Therefore, it is not a generic method to obtain the desired results for a traditional roller rig. The method proposed in Section 6.3.1 is therefore a better alternative in the case of partial correction.

6.4 Test conditions and simulation results

In order to verify the correction strategies proposed, different tracks consisting of tangent track, transition and full curve with different radius are considered in simulation cases listed in Table 6.1.The leading wheelset of the first bogie of the vehicle is chosen to generate reference time histories fed to control unit. The target contact force time histories are generated by means of numerical simulation performed using the MBS model of a complete railway vehicle defined in Chapter 4.

6.4.1 Control system response

The control system is pivotal to the success and accuracy of the test in which the actuators should possess adequate response speed and pass-band. To evaluate the performance of the control system, the responses of the actuation module are investigated as shown in Figure 6.4.

The results indicate that the performances of the actuators are adequate for this study, as they are able to follow the reference signals very well with a negligible phase lag. However, the validation of the proposed method to derive the control signals for

Table 6.1: *Simulation cases*

Case No.	Velocity [m/s]	Radius [m]	Cant deficiency [mm]
1	45	600	366
2	45	900	194
3	45	1200	108
4	45	1500	56.4
5	45	2000	4.82
6	37	600	199
7	32	600	111
8	29	600	64.3
9	25	600	9.28
10	45	600	456
11	45	600	416
12	45	600	316
13	45	600	266
14	45	600	216
15	45	600	166

the roller rig needs more evidence from the comparisons between the vehicle and rig with respect to the dynamic behaviour of the wheelset interested. To this end, a set of comparisons and analyses among the results from vehicle, normal roller rig with and without correcting loop model are carried out in the following sections.
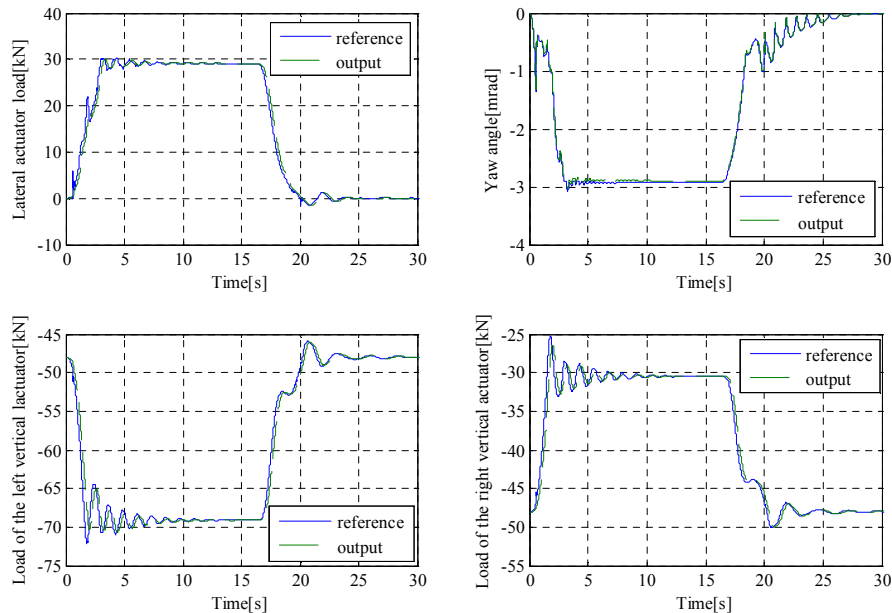
Figure 6.4: *Responses of the actuation module.*

6.4.2 Results for no correction model

For the purpose of comparison, the simulation Case 1 has been chosen to show the results from the roller rig test before reference correction. Figure 6.5 presents the time

histories of the vertical (left) and lateral (right) components of the contact forces at the wheel-rail/roller interface for the case of no correction (references derived according to the method proposed in [23]).
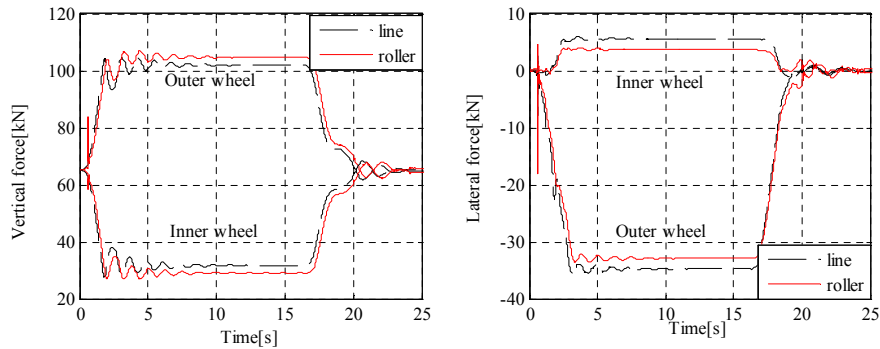

Figure 6.5: *The time history of the vertical (left) and lateral contact force (right).*

It can be seen that the roller rig reproduces well the vertical component of the contact forces although a slight delay appears due to the limitation of the pass band of the actuators. As far as the lateral component of the contact force is concerned (shown in Figure 6.5, right), it can be observed that the difference on the outer and inner wheel is approximately 6% and 40%, respectively, at the full curve section. It should be pointed out that the absolute deviations on the two wheels are nearly the same approximately 2 kN.

The difference observed shall be ascribed to the fact that the lateral creep forces of the inner and outer wheels are not able to be controlled separately, whereas only the sum of them is controlled through the action of the lateral actuator. The distribution of the lateral contact forces on the two wheels depends on many factors such as the creepage conditions and the contact parameters influencing the force-creepage relationship.
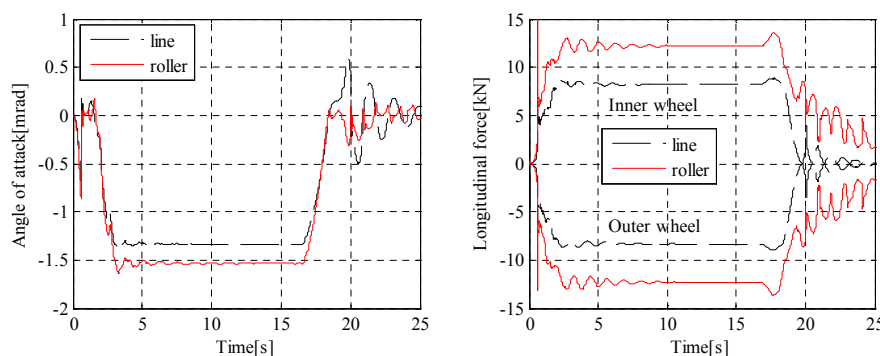
Figure 6.6: *Angle of attack the wheelset (left) and longitudinal contact force (right).*

Figure 6.6 shows the time histories of the angle of attack (left) of the wheelset and that of the longitudinal component of the contact forces (right) obtained on the track and on the roller rig. As far as the angle of attack of the wheelset is concerned, the difference between the two results in the steady state curving condition is approximately 10% ,

whereas for the longitudinal force component a larger difference is observed, due to the different longitudinal creepage conditions of the wheelset on the roller rig and on the track as discussed in Chapter 3. It is worth recalling that the two rollers of the rig are rotating at the same speed, so the difference in the rolling speed of the outer and inner wheels cannot be reproduced. Furthermore, the variation of the rolling radius of the roller produced by a lateral displacement of the contact point brings an additional term in the longitudinal creepages of the wheelset on the roller as discussed in Chapter 3 (cf. [47]), which is not present for the wheelset running on the track.

In order to investigate the dependency of the deviations of the contact components caused from the rig test on the track conditions simulated, a set of simulations is performed with varied curve radius, rolling speed and curve super-elevation.
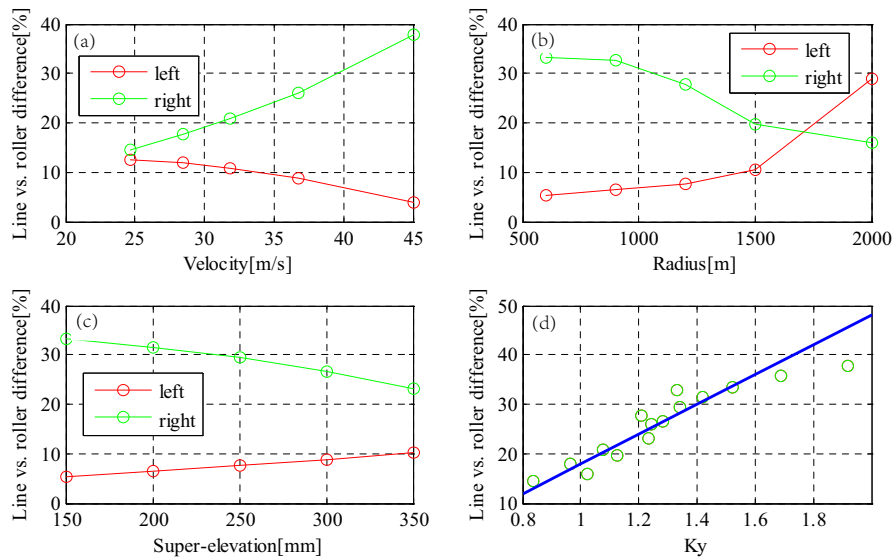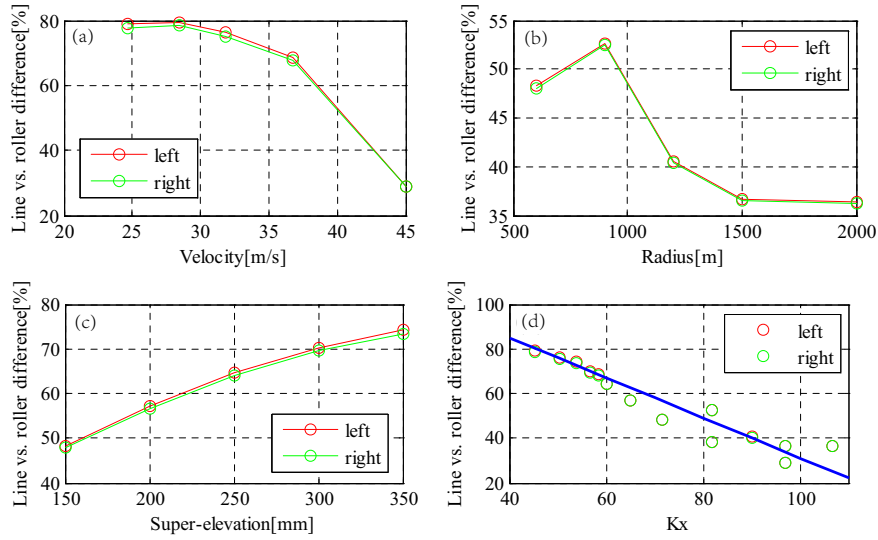

Figure 6.7: *Line vs. roller difference in terms of lateral contact force.*

The percentage difference of the lateral and longitudinal component of the contact force obtained from the test and the complete vehicle on line simulation are presented in Figure 6.7 and Figure 6.8, respectively. In Figure 6.7(a) and Figure 6.8(a) the percentage difference is displayed as function of the rolling speed (for the same curve radius and super-elevation), in Figure 6.7(b) and Figure 6.8(b) the same quantity is displayed as function of the curve radius (for the same wheelset rolling speed and curve super-elevation), and finally in Figure 6.7(c) and Figure 6.8(c) the same is shown as function of the super-elevation (for the same wheelset rolling speed and curve radius).

It is observed from Figure 6.7(a)-(c) that the variation trend in terms of the lateral wheel-rail contact force components is approximately opposite with respect to the left and right wheel, and the average value is approximately equal to 20%. Figure 6.8(a)-(c) present that the difference with respect to the longitudinal wheel-rail contact force components decreases with the increase of rolling speed and curve radius, whereas, it increases with the increase of super-elevation.

In order to translate the test results on the roller rig to the field test, it is necessary to find the relation between the two systems. To this end, a variable K_i is introduced to

Figure 6.8: *Line vs. roller difference in terms of longitudinal contact force.*

relate the deviations to the test conditions, which is approximately linear as observed in Figure 6.7(d) and 6.8(d). The definition of K_i and the estimation formula of the mean value of the percent difference ΔE_i (%) are given by Equations 6.6- 6.8.

$$K_x = V \left(\frac{R}{h} \right)^{\frac{1}{3}} \tag{6.6}$$

$$K_y = \frac{V}{R^{\frac{1}{3}} h^{\frac{1}{4}}} \tag{6.7}$$

$$|\Delta E_i| = m_i K_i + n_i \tag{6.8}$$

where V is the rolling speed of the wheelset, R is the curve radius, and h is the super-elevation, the subscript $i = (x, y)$ corresponds to the case of longitudinal and lateral, respectively, $m_x = -0.9$, $m_y = 30$, $n_x = 121$ and $n_y = -12$ are constants which can be determined by a linear regression performed on the data presented in Figure 6.7(d) and 6.8(d), respectively.

As mentioned above, the variation trend in terms of the lateral wheel-rail contact force components is approximately opposite for the left and right wheels, so only the right wheel is shown in Figure 6.7(d). Equation 6.8 can be used to estimate the experimental difference in any combinations of curve parameters in the given range of K_i, also can be treated as a correcting reference after validation in the process of transferring the laboratory results to field conditions.

6.4.3 Results for the partial correction method

This section presents the results from virtual tests based on the partial correction method. Figure 6.9 shows the time histories of the vertical, lateral and longitudinal contact force components before and after the correction which are compared to their respective target signals for Case 5 in the left column and for Case 10 in the right column.
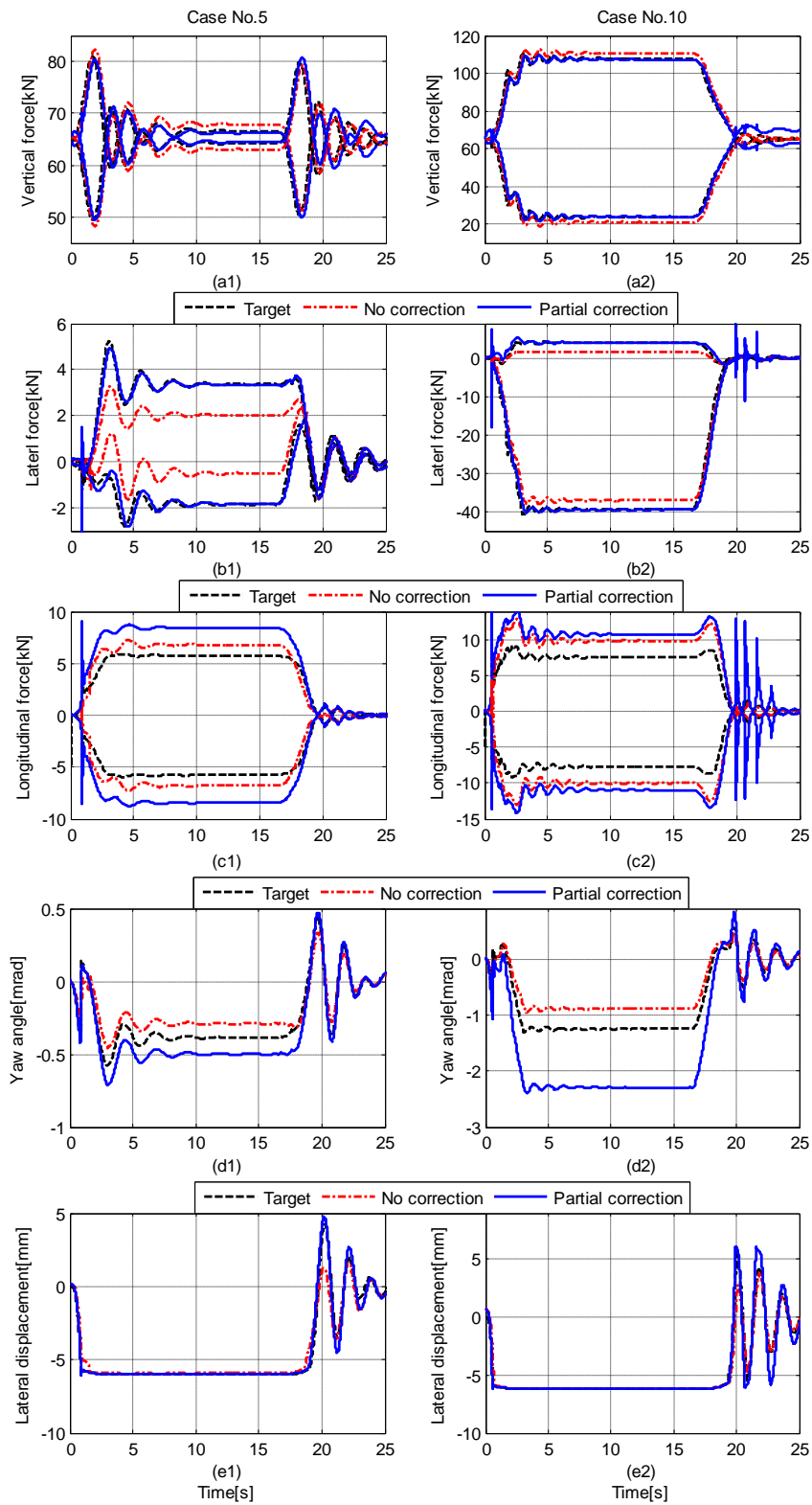
Figure 6.9: *Comparison of time histories with partial correction for Cases No.5 and10.*

It can be seen from Figure 6.9(a1)-(b2) that the corrected time histories of the vertical and lateral components of contact force are in much better agreement with the target signals compared with the no correction condition in both cases under consideration. However, the deviations caused in the longitudinal component of the contact force slightly increase with respect to the no correction condition, which results from the tuning of the references of the yaw actuators as shown in Figure 6.9(c1) and (c2). The method used to compensate the remaining deviations will be addressed subsequently.

To investigate the sensitivity of the method proposed to the track conditions, simulations were performed considering various curve radius, rolling speed and cant deficiency as listed in Table 6.1. The variation of the deviations of the vertical and lateral wheel-rail contact force components of the wheelset in the line and on the roller rig are presented in Figure 6.10.
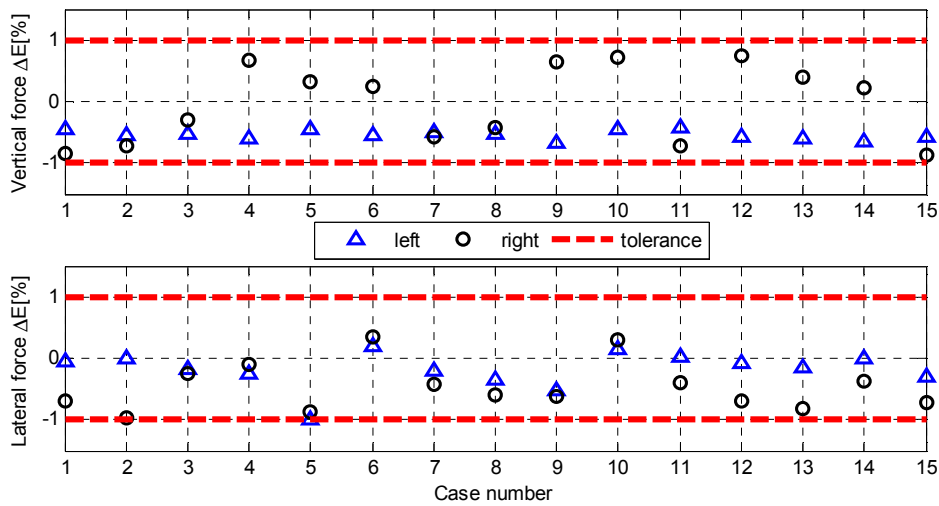
Figure 6.10: *Line vs. roller deviation in the vertical (upper) and lateral contact forces (lower).*

It can be observed from Figure 6.10 that the deviations between wheel-roller contact and wheel-rail contact in terms of vertical and lateral forces are confined within prescribed tolerance $\varepsilon = 1\%$ for all the running conditions considered. The deviations of the longitudinal forces show a trend with the vehicle speed, curve radius and cant deficiency, as presented in Figure 6.11.

In reference [73] it was shown that the relatively large deviations of the longitudinal forces obtained on the roller rig compared to the vehicle running on a track can be well approximated by an interpolation function. In this way, the results of an experiment carried out on the roller rig can be used, at least in first approximation, to analyse the behaviour of the wheelset on track not only for the vertical and lateral forces, but also for the longitudinal ones.

The same procedure is carried out here, and the results suggest that the variation trend of the deviations is similar to that of reference [73]. It is interesting to find that the estimation formula K_x obtained by linear regression in this reference remains valid in this case, as shown in Figure 6.11 (d).
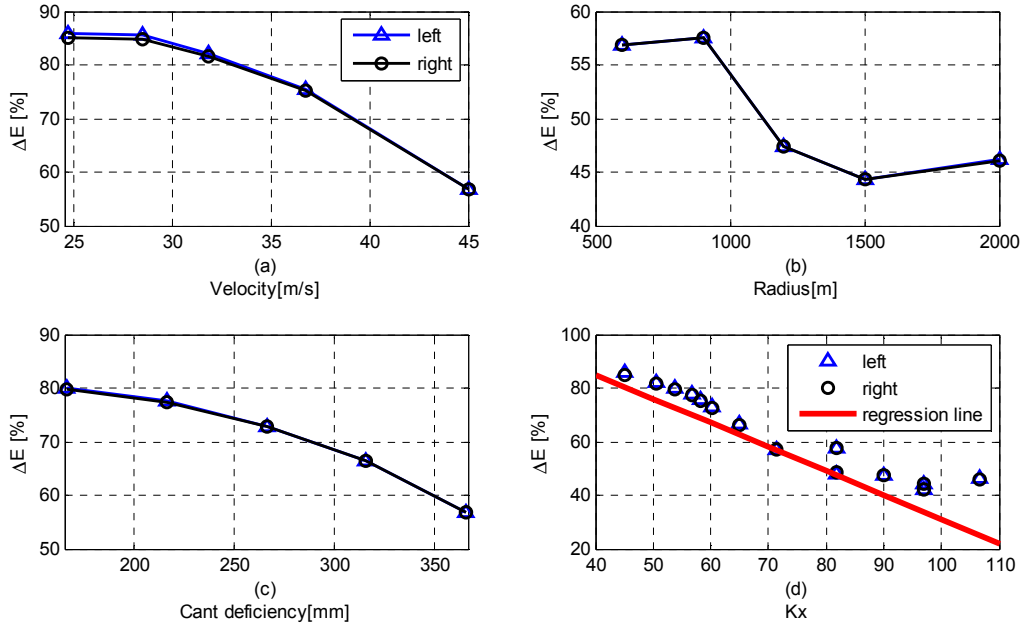
Figure 6.11: *Line vs. roller deviation in terms of longitudinal contact force.*

6.4.4 Results for the optimal correction method

In order to solve the optimization problem expressed in Equation 6.5, the MATLAB built-in function $fminsearch$ is used. Being the calculation process quite time consuming, only simulation Cases No.1, 5, 9 and 10 are chosen as examples. Table 6.2 resumes the correction factors introduced for the different actuator references, and compares the deviations ΔE_k obtained on the different contact force components for the case with no correction (i.e. references defined according to the method described in [23]) and for the optimal correction. Additionally, the final row in the table show the value of the figure of merit J, cf. Equation 6.5.

Very small deviations are obtained for all contact force components after correction (second column in each case), although the initial deviations with no correction (first column in each case) are sometimes large, up to more than 80%. This conclusion applies to a wide range of curving conditions, can therefore be considered as having general validity for the experimental simulation of wheelset curving on a roller rig.

The time history of the vertical, lateral and longitudinal contact force components after optimisation are compared to their respective target signals for Case No.5 (smallest cant deficiency) in Figure 6.12 left column and for Case No.10 (largest cant deficiency) shown in right column. The time history of the contact force obtained using no correction of the references are also show in the figures as a term of comparison.

The optimally corrected time histories shown in Figure 6.12 have a fairly good agreement with the target signals in terms of contact forces which suggests that the variations of contact forces of the wheelset on curves are able to be reproduced at a desired level of accuracy by means of the roller rig test provided that a suitable method is used to generate the references. With reference to Figure 6.9, it can be observed that the application of the differential gear is not only able to obtain good results in terms of ver-
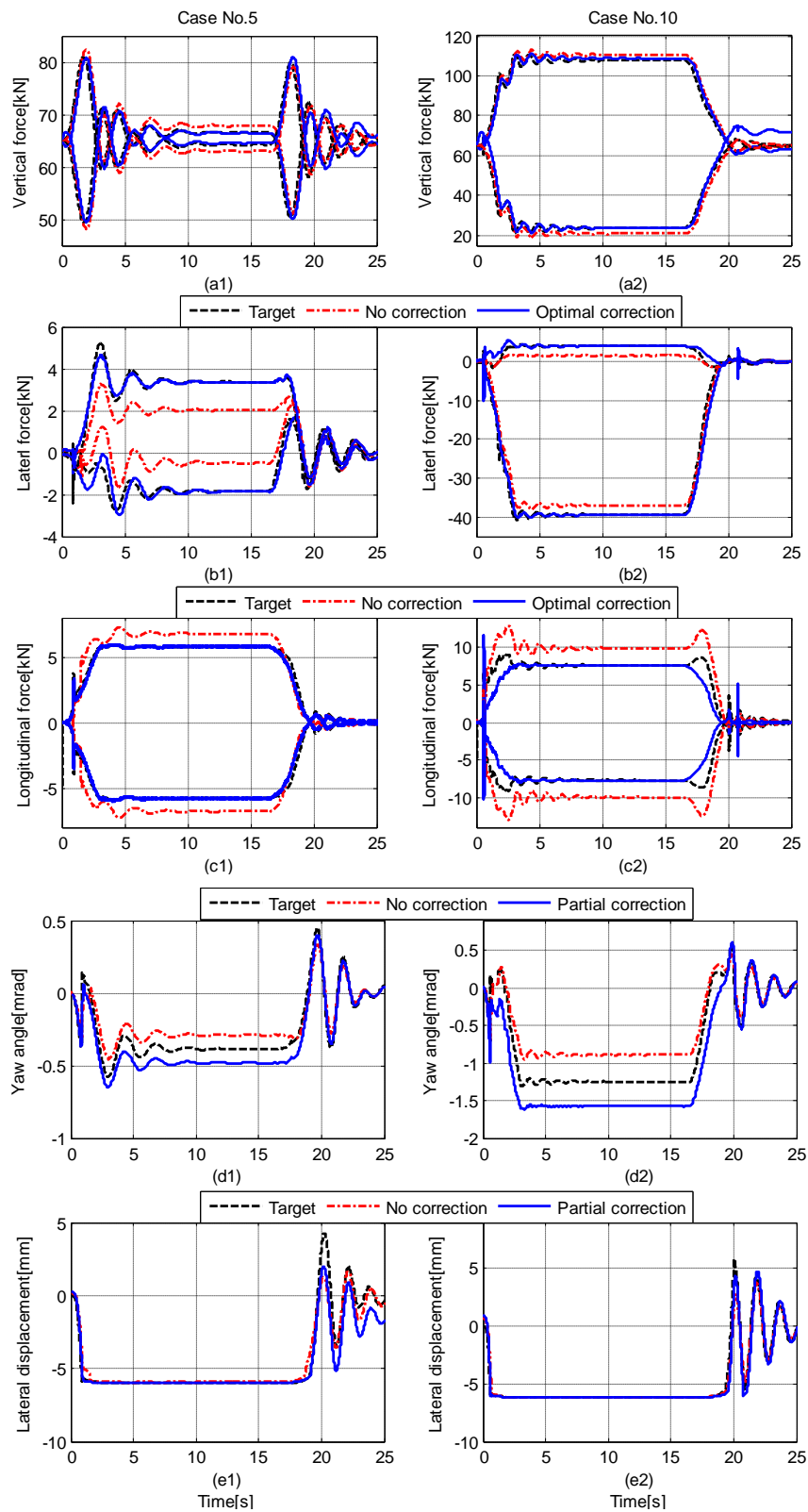
Figure 6.12: *Comparison of time histories with optimal correction for Cases No.5 and10.*

tical and lateral contact force as already obtained using the partial correction method, but also to reproduce the longitudinal force accurately.

Table 6.2: *Results for the optimal correction method (using a diffential gear)*

Actuation module i	Optimised correction factors F_i							
	Case.1		Case.5		Case.9		Case.10	
Left vertical	0.969		0.979		0.972		0.986	
Right vertical	1.085		1.026		1.039		1.117	
Lateral	1.720		1.502		1.882		1.739	
Yaw	0.998		0.985		0.996		0.999	
Secondary motor	0.997		1.778		1.797		0.882	
	Deviation $\Delta E_k[\%]$							
Force component k	No corr.	Opt corr.	No corr.	Opt corr.	No corr.	Opt corr.	No corr.	Opt corr.
Left vertical	3.1	-0.5	1.4	-0.1	2.9	-0.1	3.1	1.0
Right vertical	-9.9	1.0	-1.4	0.5	-3.2	0.9	-13.6	0.3
Left lateral	-13.2	-0.1	-108.3	0.4	-65.9	0.1	-8.1	0.1
Right lateral	-81.8	-0.1	-58.1	-0.8	-76.6	0.1	-80.7	-0.1
Left longitudinal	71.8	-0.2	59.1	0.3	257.1	0.1	33.6	0.1
Right longitudinal	71.9	-0.1	58.8	0.3	254.0	0.4	33.9	0.2
Figure of merit J	131.5	1.1	148.5	1.0	375.3	0.9	95.2	1.0

Results are presented for both correction methods, showing that the deviation of roller rig test results from the considered targets can be kept within low tolerances (1% approximately) as far as the vertical and lateral contact forces on both wheels are concerned, For the longitudinal forces, larger deviations are obtained on a test rig with standard arrangement (rollers rigidly connect), but can be reduced substantially in case a differential gear is introduced.

WEAR TEST ON A ROLLER RIG

7.1 Chapter summary

Railway wheel wear prediction is a traditional topic, which plays a relevant role in railway maintenance. The lifetime of the wheels is usually determined by the duration of the wear process before the wheel surface wear at some profile point reaches a critical value. To avoid the degradation of the vehicle performances, the wheels need to be re-profiled to restore their original profiles. This maintenance operation involves costs and immobilization time which decreases the profitability of the operation of the rolling stock.

An accurate prediction tool for wheel profile state in service can guarantee the wheelset to serve at its longest life with safer and more reliable operation. In addition, it is useful for optimising the maintenance and replacement schedule. In other words, accurate prediction of wheel wear substantially helps in achieving the goals of maximum safety and availability, minimum unexpected failure of components and maintenance, consequently reducing the cost significantly. Therefore, it has always been an attractive subject for railway operators and engineers.

Extensive theoretical and experimental work has been done for understanding the wear mechanisms and predicting the wear evolution in the wheel-rail interface [15, 31, 36, 48, 49, 70, 117]. From a theoretical point of view, two approaches are generally used to predict railway wheel wear in the tribological investigation: sliding contact by using Archard's equation [9] and rolling/sliding contact by using the energy dissipation effect [22, 82].

From an experimental point of view, three types of tests are commonly performed to study wear. The first type is the twin disc or pin-on-disc test concentrating on the tribological level [68, 116] where the testing condition can be strictly controlled. This kind of wear test is designed to establish the wear mechanisms, to identify the wear

regimes of the wheel/rail material and to determine the wear coefficients necessary for the wear modelling [22]. The second is the full-scale roller rig test where the actual geometry characteristics of the wheel and rail profiles can be taken into account, and the real operating conditions can be simulated within a controllable environment [21]. The last one consists of taking measurements of the wheel profile for a train under study at regular intervals of mileage run. Strictly speaking, this is not a test like the other two mentioned above, rather than a data collecting process because the contact condition is not under control. However, the measured wheel profile data are very useful for wear modelling validation.

This chapter focuses on the full-scale roller rig test for the railway wheel profile wear study. A set of virtual wear tests on the roller rig based on the numerical model developed in Chapter 4 are performed within the framework of the testing procedure described in Chapter 5.

7.2   Wear phenomenon in the wheel-rail interface

The wear phenomenon may be classified by mechanism and by engineering consequence, and it can be further divided into four different types from the mechanism point of view, namely adhesive wear, abrasive wear, corrosive wear and fatigue wear [88]. The wear mechanisms are often coupled, which make the wear phenomenon difficult to describe. For wheel and rail service life, abrasive wear, adhesive wear and fatigue wear are among the decisive factors, while the evolution of wheel and rail profiles is mainly due to abrasive and adhesive wear [69]. However, many studies of the wheel-rail contact focus on adhesive wear only.

Theoretically, railway wheel wear takes place in two forms, namely regular wear which refers to the change in the transversal profile, and irregular wear or out-of-roundness of wheel which is the formation of periodic wear in circumferential direction of the wheel. In general, these two forms are treated separately in modelling methodology because of the different production mechanism and evolution law. Regular wear is dominant in terms of wear damage in practice, which is produced by slowly varying values of contact forces and slips associated with the longitudinal and lateral motions of the wheelset [67]. Only regular wear is concerned in this chapter.

7.3   Virtual wear test on a roller rig

A virtual wear test is a numerical simulation program to reproduce the test on a roller rig in laboratory. The basic structure of a virtual wear test on a roller rig is presented in Figure 7.1.

It can be seen from Figure 7.1 that the virtual test starts from the vehicle characteristics and initial wheel and rail profiles, a sequence of service conditions (e.g. tangent track running at different speeds, curve negotiation at specified cant deficiencies, etc.) called "vehicle mission profile" in the figure, which is simulated using the MBS model of the rail vehicle model developed in Chapter 4. It is followed by the control references generator which is developed based on the method proposed in Chapter 5 by taking the outputs from the MBS vehicle model. Then the control references are passed to the MBS model of the roller rig developed in Chapter 4. It should be pointed out that although the Hertzian model combined with FASTSIM used for solving the wheel-rail

contact problem inside the MBS model is very fast and reliable, it does not provide the details of the contact patch that are required for wear calculation. Thus, the local contact analysis focusing on the contact patch is necessary. At each integration step of the roller rig simulation, global contact parameters such as the shapes and relative orientation of the profiles, the positions of the contact reference points, the creepages and the normal contact force are fed into the local contact model, i.e. the KP model in this case. The KP model will then iterate the penetration until the same normal force in the global output is achieved. The resulting contact forces and contact patch are used for wear calculation. It should be noted that the KP model used for local contact analysis is able to provide more realistic results compared to the Hertzian model used in MBS simulation, while the inconsistency introduced during this process is difficult to compensate especially in the case of highly non-Hertzian contact conditions. That is the reason why the proposed EKP model suitable for highly non-Hertzian contact problems is not used here. Finally, a model for the estimation of the wheel profile evolution is needed to calculate the distribution of removed material in each contact patch which is the task addressed.
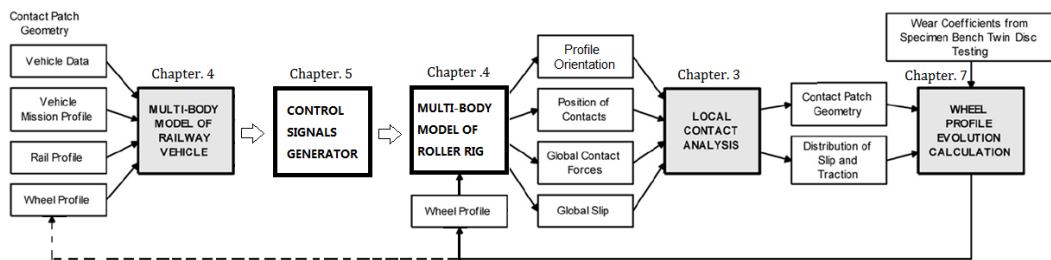
Figure 7.1: *Wear simulation on roller rig, adapted from [67].*

It can be found that the virtual test procedure described above is very similar to the approach commonly used for the wheel profile wear prediction, for instance the approach used in [67]. The major differences are the inclusion of a roller rig model and a reference generation process. Moreover, there are tow options of completing the profile updating loop in a virtual test. In more detail, the updated profiles can be applied to the vehicle model that is used for generating new references for the roller rig with updated profiles as presented in dashed line in Figure 7.1, or the updated profiles are directly applied to the roller rig model as indicated by solid line in Figure 7.1. Obviously, the second way is simpler since the test keeps running without the need of updating control references which implies this method ignores the effect of the change in wheel profile of the vehicle model for the generation of control references.

Actually, the profile updating strategy is also very important in the wear simulation process. A frequent profile updating strategy could result in unnecessary computational effort. On the other hand, if the profiles are not updated at the appropriate time, it may lead to inaccuracies in the final worn wheel profile or divergence in numerical simulation. Different wheel profile updating strategies were compared in [14] and it was found that the most efficient one is based on the maximum wear depth, i.e. the profile is updated when a given threshold of the maximum value of cumulative wear depth is reached. A sensitivity analysis showed that a threshold of 0.1 mm is a good

compromise between calculation accuracy and computational cost.

In order to ensure the convergence in the numerical simulation, a smoothing process of the updated profiles is needed. Different smoothing strategies were compared in [14] as well. It suggests that a combination of a moving average applied to the cumulative wear depth before profile updated and a cubic smoothing spline applied to the updated profiles before starting a new iteration of the wear calculation, is a good option for this purpose.

7.4 Wheel profile evolution calculation

Archard's equation is commonly used in adhesive wear prediction in the field of tribology. Actually, it has been calibrated for use with wheel and rail steels and has been applied successfully for different applications [15,36,48,49]. Archard's equation states that the volume of material worn V_w is proportional to the sliding distance s and the normal load N, and inversely proportional to the hardness of the material concerned H as expressed by Equation 7.1.

$$V_w = K \frac{Ns}{H} \tag{7.1}$$

where K is the wear coefficient which represents the proportion of all the asperity contacts resulting in the production of a worn particle [10].

The applications mentioned above suggest that the critical part of the application of Archard's equation lies in the determination of coefficient K. Currently, it can be derived from laboratory tests or, alternatively from extensive calibration based on geometrical comparisons between simulated and measured wheel profiles. Nowadays there exist in literature a few wear charts and maps for the wear coefficient as a function of contact pressure and sliding speed, concerning different rail-wheel materials and environments cf. [10, 48]. The available wear maps are mostly for dry conditions, and they are not very accurate due to the limited number of experiments available in each condition. Hence such maps are of restricted usefulness and it would be desirable to have more accurate maps.

The problem is that the experimental determination of K is difficult and subject to some uncertainty which should be taken into account to improve the predictability of the models. To this end, a probabilistic approach will be proposed in the following sections. Although a probabilistic approach can be used for the wear coefficient [11, 12], it has in fact usually been treated deterministically, for instance, the application cases mentioned above. Nevertheless, descriptions of the use of probabilistic approaches to determine the wear coefficient are rarely found in the literature, especially in railway wheel wear prediction.

7.4.1 Wear coefficient

Among many experimental investigations of the wear coefficient determination, the work due to the research group at the Royal Institute of Technology (KTH) is the most worthwhile to be mentioned. They assumed K is function of sliding speed and contact pressure between the contact pair. The observation from test shows that the relationship between K and sliding speed and contact pressure is also dependent of material and contact conditions (e.g. dry, wet). Therefore, they constructed a wear map based

on the analysis and interpolation of different sets of experimental data, including twin-disc and pin-on-disc results, on different materials and with dry contact conditions, see Figure 7.2. This makes the wear function material-independent but introduces an approximation in the method, and it is only applicable under dry condition [86]. This map is commonly used in railway field for dealing with wear problem. However, the wear coefficient K from the KTH wear map must be recalibrated for any specific wheel-rail combination or condition to obtain more realistic results compared with field measurement [15, 50].
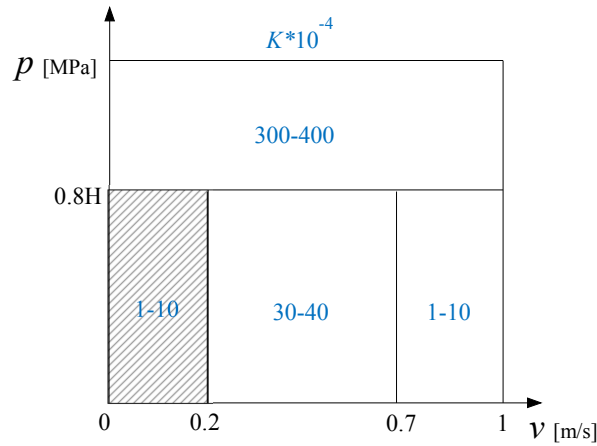
Figure 7.2: *Wear map for dry wheel-rail contact, adapted from [48].*

For simplicity, the common method to obtain the wear coefficient is taking the middle value of each region from the KTH wear map [49]. It leads to an averaging effect in the wear prediction and of course there is no uncertainty considered at all, consequently reducing the accuracy of the final result. This method for the determination of K is labelled MV method in the thesis.

To take the experimental uncertainties in the identification process of the wear coefficient and overcome the issue of having few measurements, Universal Kriging technique [28] is used for the determination of K to take advantage of the spatial dependence of measures in sliding speed v (m/s) and pressure p (MPa) plane. The proposed model [27] allows an uncertainty analysis of the value of the coefficient K, so that a prediction interval for K associated to each choice of v and p can be obtained instead of a single punctual prediction. As a consequence, this model predicts a range for the amount of wheel wear, which is desirable in practical maintenance for railway operators.

The measurement data were obtained from experiments carried out at the University of Sheffield by wear testing machine under different conditions with different wheel and rail materials. For demonstration purpose, the experimental results from $Class D$ wheel (H=2.45e3 MPa) versus $BS11$, $UICA$, $UICB$ and $1\%Chr$ rail under dry condition are chosen. Most of observations are in the domain $O = \{0 < v < 0.08, \ 400 < p < 1300\}$ which fall into the shaded region in Figure 7.2. Therefore, a spatial model with linear drift is used to estimate the wear coefficient and to exploit the similarities among different materials and the spatial dependence of measurements.

A linear model for the drift

Firstly, a linear model is applied to estimate the drift (large scale variability) [53] and assess whether there are statistically significant differences in wear coefficient K of the 4 different rail materials. Given that the distribution of K is highly asymmetrical and concentrates in a small region, a logarithmic transformation on this variable is performed.

Then we start fitting a linear model with response $\log K$, quantitative predictors the sliding speed v and the contact pressure p, and the categorical variable of the rail material (as well as their interactions). Variable selection leads to the reduced model:

$$\log K = \beta_0 + \beta_1 k_a + \beta_2 k_b + \beta_3 k_c + \beta_4 k_a v + \beta_5 k_b v + \beta_6 k_c v + \beta_7 k_a p + \beta_8 k_b p + \beta_9 k_c p + \varepsilon \tag{7.2}$$

where $k_i (i = a, b, c)$ are dummy variables that take the value of 1, indicating the corresponding rail material of $BS11$, $UICB$ and $1\%Chr$, respectively, and $k_i = 0$ indicates $UICA$ rail.

Table 7.1: *Estimates, standard errors and t-tests for the nullity of the coefficients of the linear model*

	Estimate	Std. Error	t value	Pr (>|t|)
β_0	2.564	0.114	22.52	< 2.2e-16
β_1	-3.651	0.442	-8.26	6.17e-13
β_2	-3.081	0.514	-5.99	3.33e-08
β_3	-4.145	0.571	-7.27	8.31e-11
β_4	14.534	2.213	6.57	2.33e-09
β_5	22.564	5.079	4.44	2.30e-05
β_6	23.498	4.337	5.42	4.16e-07
β_7	0.00243	0.000431	5.64	1.57e-07
β_8	0.00170	0.000433	3.91	1.67e-07
β_9	0.00258	0.000470	5.49	3.10e-07

Table 7.1 lists the coefficients estimated, the standard errors and the p-values of the t-tests for the nullity of such coefficients: all the regressors are significant. Moreover, the F-test assesses the significance of the model (p-value < 2.2e-16) and the adjusted coefficient of determination R^2 is quite high (0.65), so the model fits well the data. However, residuals do not respect the independence assumption that is fundamental for the linear model used. In fact, residuals are spatially correlated (the space being the v and p plane) and this fact should be taken into account to obtain an accurate value of the coefficient K. To this end, the Universal Kriging [53] method is chosen for prediction and uncertainty analysis of the wear coefficient, and this method is named UK method in this thesis.

Prediction and uncertainty analysis

The measurements are assumed to be spatial data with coordinates of the sliding speed v (m/s) and the contact pressure $\tilde{p}$ (10^{-4} MPa) where the pressure scale is changed to obtain comparable coordinate ranges. The aim is to predict the wear coefficient K within the domain $D = \{0 < v < 0.25,\ 0 < \tilde{p} < 0.2\}$, taking advantage of the spatial correlation of data. The following assumption is made.

$$\log K(\mathbf{s}) = \mu(\mathbf{s}) + \delta(\mathbf{s}), \quad \mathbf{s} \in D \tag{7.3}$$

where $\mu(\cdot)$ is the drift given by Equation 7.2 and $\delta(\cdot)$ is a zero-mean second-order stationary random process with variogram $2\gamma(\cdot)$.

A spherical variogram model is used to fit the estimated one, fixing the nugget thanks to some repeated measures of the wear coefficient in the same position s. The UK method is then used to predict $\log K(\cdot)$ on a grid in the domain D, for each of the 4 rail materials considered. Moreover, the prediction variance is also computed on the grid, allowing the construction of 90% pointwise prediction intervals under the assumption that $\log K(\cdot)$ is Gaussian.

Figure 7.3 shows the wear coefficient maps predicted with the UK method in domain O for $ClassD$ wheel combined with the rail $BS11$ (a1-a3) and $UICA$ (b1-b3), and Figure 7.4 for the rail $UICB$ (a1-a3) and $1\%Chr$ (b1-b3). The lower and upper bounds depict the 90% pointwise prediction intervals. It is important to notice that UK method prediction is more informative than the wear map in Figure 7.2 (K= 5e-4 in the domain O by the MV method), and it is associated a rigorous quantification of uncertainty (prediction intervals).
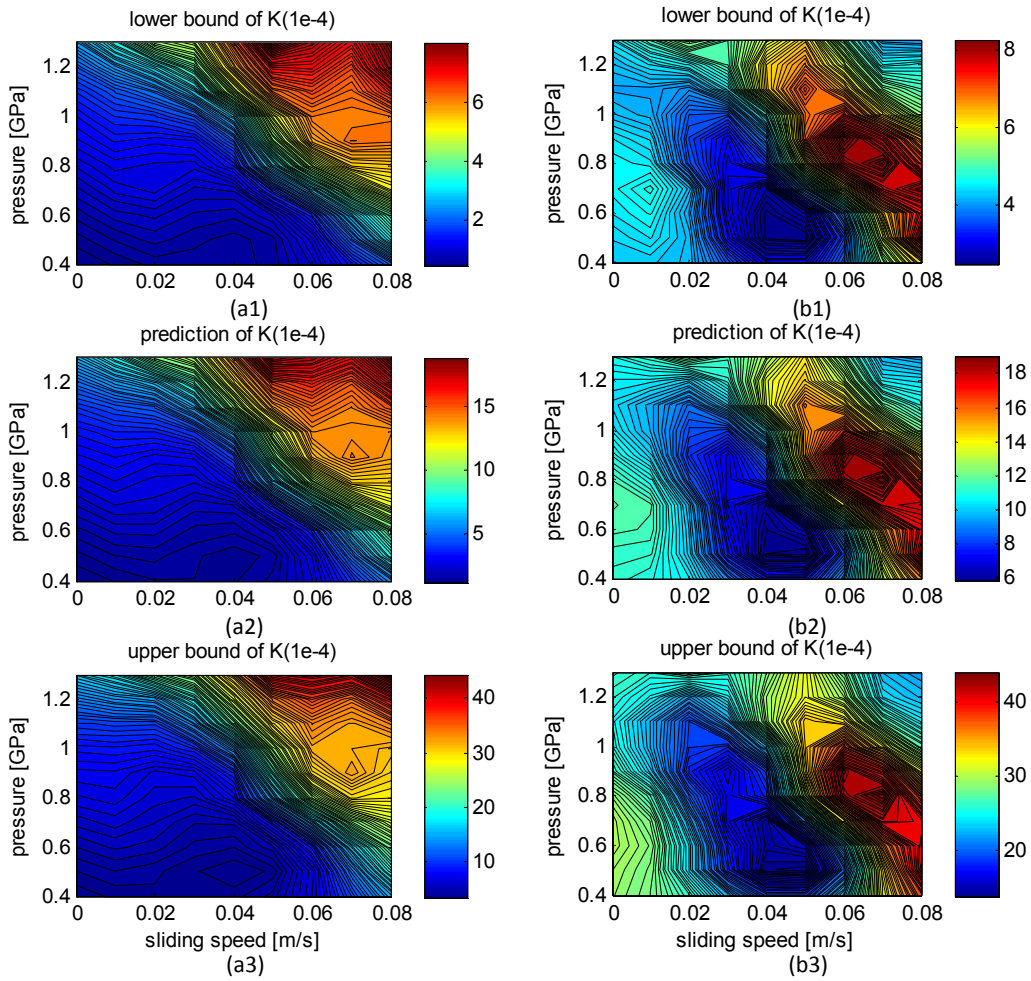

Figure 7.3: *Wear coefficient maps of $ClassD/BS11$ (left) and $ClassD/UICA$ (right).*

With reference to Figure 7.2, it can be concluded that the wear coefficients obtained

from KTH wear map are qualitatively acceptable in most cases because some of the wheel-rail material combinations manifest similar pattern of wear regime, for instance $ClassD$ wheel versus $BS11$, $UICB$ and $1\%Chr$ rail. However, it must be recalibrated for quantitative prediction of wear for specific contact pair due to the statistically significant difference exist, e.g. $UICA$ rail in Figure 7.3 compared to others. This result has proven that the relationship between the wear coefficient, the sliding speed and the contact pressure is material-dependent. Therefore, it is hardly possible to have universal wear coefficients for various wheel and rail combinations without considering the uncertainty.

It should be pointed out that the UK method is able to provide accurate prediction in the domain O, while out of this domain it is not guaranteed.
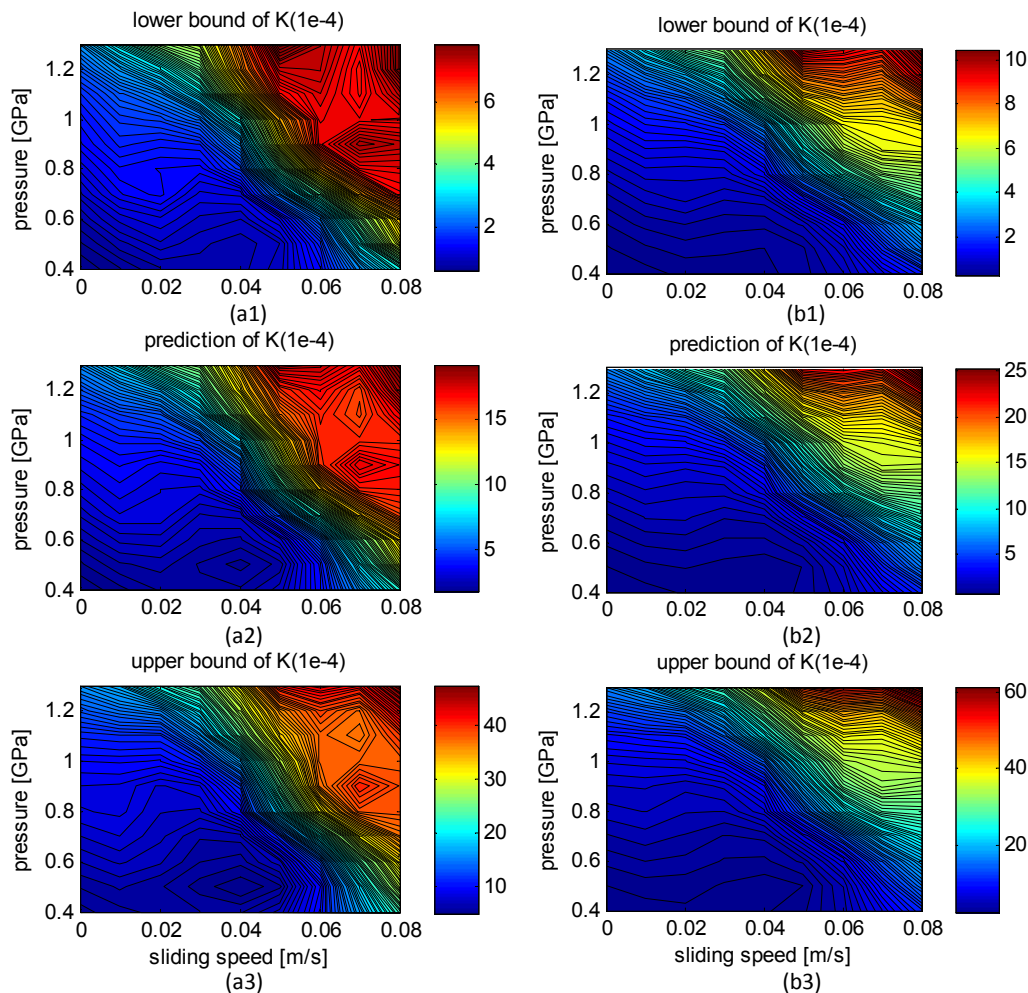

Figure 7.4: *Wear coefficient maps of $ClassD/UICB$ (left) and $ClassD/1\%Chr$ (right).*

7.4.2 Wear depth

The sliding distance s in Equation 7.1 is another very important parameter for wear estimation. Moreover, the sliding speed v is also required to determine the wear coefficient K as discussed above. Therefore, the sliding speed and sliding distance need

to be determined locally for the wear calculation considering the global contact problem is solved by FASTSIM in this study. To this end, the contact patch is divide into 50×50 elements with the size of $\Delta x \times \Delta y$ for each element. In the slip area of the contact patch, the sliding speed and sliding distance for the duration of traversing the longitudinal increment Δx can be expressed in the following forms by neglecting the elastic contribution according to the method implemented in [48].

$$v = V \begin{bmatrix} \xi_x - \xi_z y \\ \xi_y + \xi_z x \end{bmatrix} \tag{7.4}$$

$$s = |v| \frac{\Delta x}{V} \tag{7.5}$$

where V is the vehicle speed, ξ_x the longitudinal creepage, ξ_y the lateral creepage, ξ_z the spin creepage, and x, y the cartesian coordinates of the contact patch.

According to Equation 7.1, the wear depth d_w in each element can be calculated as follows:

$$d_w = K \frac{|s| p}{H} \tag{7.6}$$

The total wear distribution over the contact patch is obtained by adding the wear depths for each element in the slip zone for all longitudinal strips of the contact patch.

7.4.3 Comparison between the UK model and MV model

For simplicity, the wear depth calculation Equation 7.6 is called the UK model when wear coefficient K is obtained by the UK method and called MV model when K is obtained by the MV method. In order to check the effect of the uncertainty of the wear coefficient on the wear simulation results, the two cases listed in Table 3.3 in Chapter 3 are chosen to make comparisons between the UK and MV models. The wear coefficient K is determined according to the UK method when the pressure and sliding speed fall into the domain O, and the MV method is applied for the rest.

Figure 7.5 shows the maximum pressure distribution, maximum sliding speed and normalized wear depth within the contact patch from top to bottom, for Case 1 (left column) and Case 2 (right column), respectively. It can be observed that the maximum pressure is approximately 1000 MPa, and the maximum sliding speed in this contact patch is approximately 0.02 m/s for Case 1. Therefore, the UK method for wear coefficient determination is fully valid for the entire contact patch. The maximum wear depth over the contact patch calculated by the UK model (black line) is considerably smaller than the one estimated by the MV model (blue line) for Case 1 as shown in Figure 7.5 (left bottom). The result of the MV model is close to the upper bound result of the UK model. For Case 2, the maximum pressure is approximately 1400 MPa which exceeds the pressure limit in domain O, while the maximum sliding speed is around 0.05 m/s still within the domain O. The wear depth predicted with the MV model for this case is approximately 30 % lower than the UK model.

The simulation results show that the uncertainty of the wear coefficient has a considerable influence on the wear prediction results in some circumstances, and the UK model is able to provide the wear within a range instead of a single value in the commonly used methods. Of course, some more validations for the UK method are needed

for further application. However, the UK model is chosen for running the virtual wear test simulations in the following section.
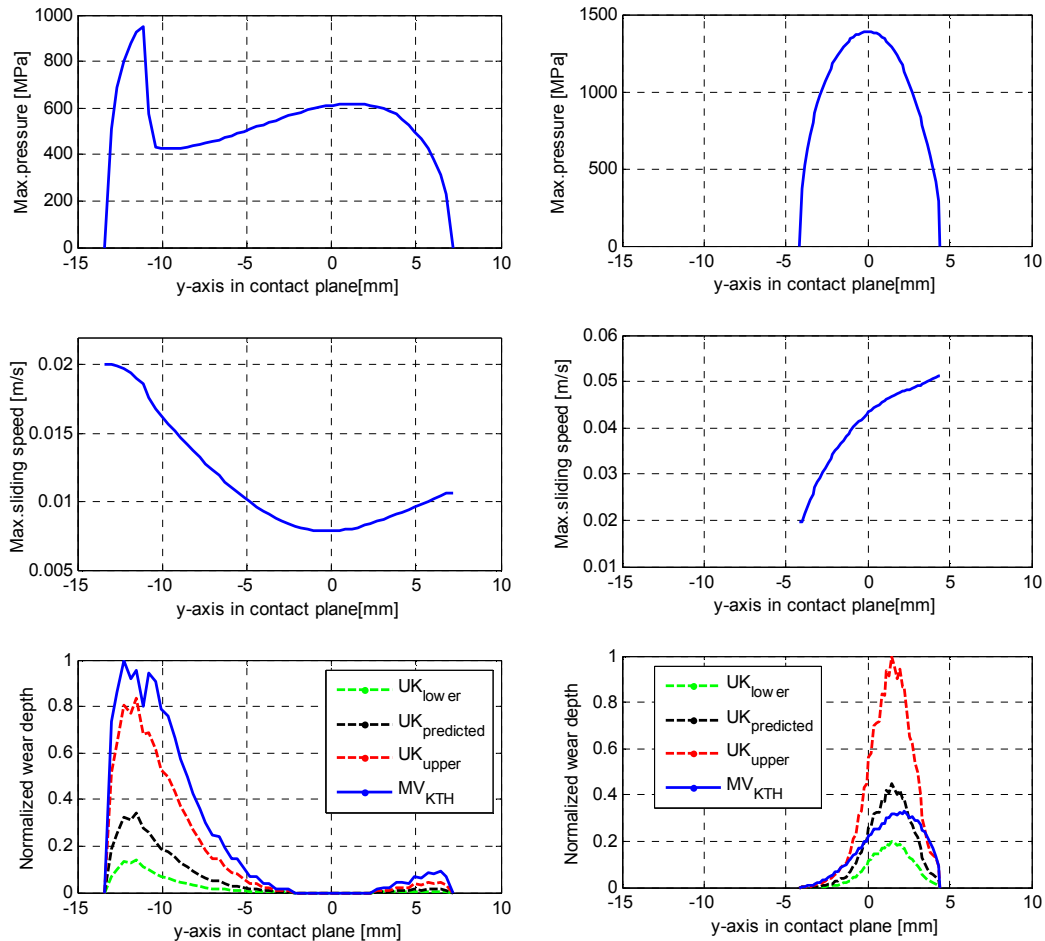
Figure 7.5: *Calculation results for Case 1 (left) and Case 2 (right) in Table 3.3 with different methods: UK_{lower} indicates the results from the UK method with the lower bound of K, $UK_{predicted}$ indicates the results from the UK method with the predicted value of K, UK_{upper} indicates the results from the UK method with the upper bound of K, and MV_{KTH} indicates the results from the MV method.*

7.5 Virtual test results and discussion

The proposed UK model has been incorporated into the virtual test simulation program aiming at estimating the wheel profile evolution of the rail vehicle developed in Chapter 4. The curve condition No.10 in Table 6.1 in Chapter 6 is chosen to demonstrate the virtual test. The complete track is modelled as symmetric with respect to left and right curves, and its total length is 3500 m. It consists of a short section of tangent track, a transition entry into the curve, full curve, an exit transition, another short section of tangent track and then a symmetrical section.

The test was performed according to the procedure introduced in Section 7.3. Two virtual tests were carried out on the roller rig with and without corrected control references according to the partial correction method proposed in Chapter 6. The wheel

wear of the leading wheelset of the complete vehicle is also calculated for the purpose of comparison with the results from the roller rig tests. Theoretically, the wear produced on the left- and right-hand wheels of the wheelset under test should be the same because of the symmetrical curved track condition considered. Therefore, only half of the complete track is taken into account for wear calculation. The amount of wear produced on each wheel profile after passing through the entire track can be obtained by simply summing up the wear of the left- and right-hand side wheels.
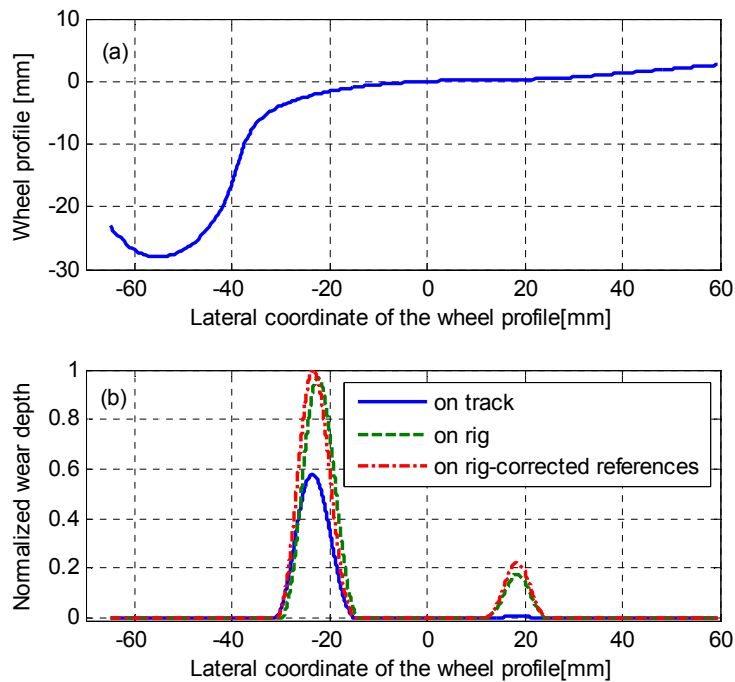
Figure 7.6: *Wheel profile wear on the roller rig versus on the track:(a) original wheel profile and (b) normalized wear depth.*

Only one iteration is run on the given track, and the wear depth on the wheel is normalized for comparison. The results from the UK predicted are shown in Figure 7.6. It can be observed that the roller rig is able to correctly reproduce the locations of flange and tread wear on the wheel profile, considering as a reference to the simulation results of the complete vehicle running on the track, whereas the amount of wear of the wheel produced on the roller rig is much higher than the wheel wear produced on the track. The correction on the references for the roller rig makes the wear location closer to the track case, but the magnitude is remain larger than the track case. This phenomenon can be explained by the accelerated effect of the roller rig on the contact surface damage discussed in Chapter 3.

CHAPTER 8

CONCLUSIONS AND FUTURE WORK

8.1 Conclusions

Roller rigs are being used in the railway community all over the world to better understand the rail vehicle behaviour and the mechanism of wheel-rail contact with the final aim at developing faster, safer and more efficient railways. They have contributed much to modern railway technology. However, the roller rig test will never completely replace the field test on real track because the inherent differences exist in the roller rig system with respect to the real wheel-rail contact system. Moreover, not all types of track conditions and excitations can be fully reproduced on most roller rigs depending on the design.

In order to exploit the best potential of roller rigs for railway application, a full-scale single wheelset roller rig has been chosen as an example for a comprehensive investigation in this work. As the roller rig is mainly used for the study of rail vehicle dynamics and wheel-rail contact mechanics, this thesis deals with these two aspects in great detail theoretically combined with typical test cases.

As far as the usage of the roller rig on wheel-rail contact study is concerned, a novel non-Hertzian contact model called EKP has been proposed and validated by comparison with the software CONTACT. The EKP model is an extension of the well-known Kik-Piotrowski model. Besides the inherent advantages of the original model, it possesses some new features including the capability of solving both wheel-rail and wheel-roller contact problems with enhanced correspondence to CONTACT for highly non-Hertzian contact conditions, and the ability of considering the effect of the yaw angle of the wheelset against the rail/roller on the shape of the contact patch and pressure distribution, which is a feature generally missing in the existing models although it is significant in certain circumstances. This analysis provides a useful framework for better interpreting the results of wheel-rail contact tests performed on a roller rig e.g. wear

and/or rolling contact fatigue tests.

To reproduce the real dynamic behaviour of a wheelset on a real track as close as possible using the single wheelset roller rig, an appropriate test procedure needs to be defined, particularly in terms of actuators' references, to make sure that meaningful wheel-rail contact conditions can be reproduced. A new method is proposed in this thesis for the optimisation of tests performed on full-scale roller rigs for a single wheelset by means of correction of actuator references in order to best reproduce the behaviour of a wheelset and especially the wheel-rail contact forces in a running condition of interest as obtained from MBS simulation. The method is supported by the use of a mechatronic model of the roller rig system implemented by means of co-simulation. Two correction strategies have been proposed. The first one considers a standard arrangement of the roller rig (rollers rigidly connected in torsion): it is shown in this thesis that this strategy allows the accurate reproduction of the vertical and lateral contact forces on both wheels but introduces inevitable deviations from the case of the wheelset running on a real track in terms of the longitudinal contact forces. Though, these deviations can be compensated by means of a suitable post-processing of results, the effect of these deviations on the wheelset behaviour (e.g. flange climb, wheel wear) cannot be eliminated from the test itself. The second correction strategy assumes that a differential gear is introduced to the rig, allowing the rolling speed of the two rollers to be controlled separately. The inclusion of the differential gear makes it possible to reproduce the full wheel-rail contact condition in terms of contact forces on the roller rig for a wheelset running on a curve, with assistance of an optimal correction for control references, ultimately leading to very small deviations of all contact force components as compared to the case of the wheelset running on a real track. This result is obtained for various curving conditions, i.e. for different combinations of the running speed, track curvature and cant deficiency. In conclusion, the testing methods presented in this thesis can be used to achieve a better correspondence between the actual running conditions of a wheelset and experiments performed on single wheelset roller rig.

This study suggest that it is possible to evaluate the practical performance of dynamics and contact mechanics in the railway systems using roller rigs, reducing the need for line tests. Despite that the focus of this thesis is on roller rigs for a single wheelset, a similar approach could be considered for more complex roller rigs allowing e.g. the test of a complete railway bogie.

The potential offered by advanced computing tools and intelligent control methods means that roller rigs can continue to offer advantages over field test. They also provide data in new areas where numerical methods are not yet proven or working outside the scope of validation. Although field testing of prototype vehicles will never be completely eliminated, roller rigs will continue to be a valuable tool to researchers and developers as an intermediate stage between computer simulations and track testing [41].

8.2 Future work

The non-Hertzian contact model proposed in this thesis has been developed with the long-term goal of providing an advanced model for wheel-rail and wheel-roller contact calculation with the best compromise between accuracy and computational effort. To

make the model complete, further work will focus on the extension of the scope of validation of the proposed model to cover a wider range of contact conditions encountered in reality and on the investigation of the effects on the tangential contact solution caused by the changes in the normal solution obtained from the proposed model, eventually developing an advanced model applicable to complete three-dimensional contact problem in rail vehicle dynamics on-line simulation. As a further step, the complete contact model will be integrated into the vehicle system dynamics simulation to investigate the influence of the proposed contact modelling method on the dynamic behaviour of the vehicle as well as on the roller rig.

The results obtained from the proposed testing methodology are assessed by means of numerical experiments performed using a mathematical model of the roller rig, but the use of this methodology in real tests on a full-scale roller rig is envisaged as a future step of the research.

Bibliography

[1] K. Ahn, J. Park, and S. Ryew. The construction of a full-scale wheel/rail roller rig in Korea. In C. Lambert and G. Holst, editors, *8th IEEE International Conference on Automation Science and Engineering*, August 2012.

[2] P.D. Allen. *Error quantification of a scaled railway roller rig*. Doctoral dissertation, Manchester Metropolitan University, Manchester, UK, 2001.

[3] P.D. Allen. *Handbook of railway vehicle dynamics*, chapter 15, Scaling testing, pages 507–525. Taylor & Francis Group, Boca Raton, 2006.

[4] P.D. Allen and S.D. Iwnicki. The critical speed of a railway vehicle on a roller rig. *Proc. Inst. Mech. Eng. Part F: Journal of Rail and Rapid Transit*, 215:55–64, 2001.

[5] B. Allotta, R. Conti, E. Meli, L. Pugi, and A. Ridolfi. Development of a HIL railway roller rig model for the traction and braking testing activities under degraded adhesion conditions. *International Journal of Non-Linear Mechanics*, 57:50–64, 2013.

[6] A. Alonso, J. G. Giménez, and M. García. Analytical methodology to solve the geometric wheel-rail contact problem taking into account the wheelset yaw angle. In *24th International Symposium on Dynamics of Vehicles on Roads and Tracks*, August 2015.

[7] A. Alonso and J.G. Giménez. Tangential problem solution for nonelliptical contact areas with the fastsim algorithm. *Vehicle System Dynamics*, 45(4):341–357, 2007.

[8] A. Alonso, A. Guiral, L. Baeza, and S. Iwnicki. Wheel-rail contact: experimental study of the creep forces-creepage relationships. *Vehicle System Dynamics*, Supplement 52:469–487, 2014.

[9] J.F. Archard. Contact and rubbing of flat surfaces. *Journal of Applied Physics*, 24:981–988, 1953.

[10] J.F. Archard. *Wear control handbook*, chapter Friction and wear of materials. ASME, 1980.

[11] Jr. Ávila da Silva, C. R. and Pintaude G. Uncertainty analysis on the wear coefficient of archard model. *Tribol. Int.*, 41(6):473–481, 2008.

[12] Jr. Ávila da Silva, C. R., Pintaude G., Al-Qureshi H.A., and Krajnc M.A. An application of mean square calculus to sliding wear. *Journal of Applied Mechanics*, 77(2), 2010.

[13] J. Ayasse and H. Chollet. Determination of the wheel rail contact patch in semi-Hertzian conditions. *Vehicle System Dynamics*, 43:161–172, 2005.

[14] G. Barbarino. *A fast and reliable mathematical model for the prediction of railway wheel wear*. Master thesis, Politecnico di Milano, Milan, Italy, 2004.

[15] A. Bevan, P. Molyneux-Berry, B. Eickhoff, and M. Burstow. Development and validation of a wheel wear and rolling contact fatigue damage model. *Wear*, 307(1-2):100–111, 2013.

[16] N. Bosso, A. Gugliotta, E. Napoli, and A. Somà. Simulation of a scaled roller rig. In *5th ADAMS/Rail Users' Conference*, May 2000.

[17] N. Bosso, A. Gugliotta, and A. Somà. Dynamic behavior of a railway wheelset on a roller rig versus tangent track. *Shock and vibration*, 215:467–492, 2004.

Bibliography

[18] N. Bosso, A. Gugliotta, and A. Somà. Dynamic identification of a 1:5 scaled railway bogie on roller rig. *Transactions on The Built Environment*, 88:829–838, 2006.

[19] N. Bosso, M. Spiryagin, A. Gugliotta, and A. Somà. *Mechatronic Modeling of Real-Time Wheel-Rail Contact*. Springer, Heidelberg, 2013.

[20] F. Braghin, S. Bruni, and G. Diana. Experimental and numerical investigation on the derailment of a railway wheelset with solid axle. *Vehicle System Dynamics*, 44:305–325, 2006.

[21] F. Braghin, S. Bruni, and F. Resta. wear of railway wheel profiles: a comparison between experimental results and a mathematical model. In H. Ture, editor, *17th International Symposium on Dynamics of Vehicles on Roads and Tracks*, pages 478–489, August 2001.

[22] F. Braghin, R. Lewis, R.S. Dwyer-Joyce, and S. Bruni. A mathematical model to predict railway wheel profile evolution due to wear. *Wear*, 261:1253–1264, 2006.

[23] S. Bruni, F. Cheli, and F. Resta. A model of an actively controlled roller rig for tests on full size wheelsets. *Proc. Inst. Mech. Eng. Part F: Journal of Rail and Rapid Transit*, 215:277–288, 2001.

[24] F.W. Carter. On the action of a locomotive driving wheel. *Proc. Roy. Soc. Lond. Ser*, 112:151–157, 1926.

[25] C. Cattaneo. Sul contatto di due corpi elastici. *Accademia de Lincei, Rendi conti*, 27:339–346, 1938.

[26] F. Cheli, G. Diana, and E. Leo. Mathematical model of a full scale locomotive roller rig model. In *Proceeding of IMECE 2008*, October -November, 2008.

[27] M.A. Cremona, B.B. Liu, and Y. Hu. Prediction of railway wheel profile wear under uncertainty of wear coefficient. Report, Politecnico di Milano, 2014. Unpublished.

[28] N.A.C. Cressie. *Statistics for spatial data*. Wiley, 1993.

[29] S. Damme, U. Nackenhorst, A. Wetzel, and B. Zastrau. On the numerical analysis of the wheel-rail system in rolling contact. In P. Schiehlen, editor, *System Dynamics and Long-Term Behaviour of Railway Vehicles, Track and Subgrade*, pages 155–174, 2002.

[30] L. Deters and M. Proksch. Friction and wear testing of rail and wheel material. *Wear*, 258:981–991, 2005.

[31] B. Dirks. *Simulation and measurement of wheel on rail fatigue and wear*. Doctoral dissertation, Royal Institute of Technology (KTH), Stockholm, Sweden, 2015.

[32] G. Dreher, F. Jobst, G. Götz, L. Mauer, A. Mielkarek, J. Nestmeier, and H. Örley. Active control of a wheel/rail vehicle demonstrated up to 530 km/h on the German roller test rig. In *8th International Symposium on Dynamics of Vehicles on Roads and Tracks*. Swets and Zeitlinger, August 1983.

[33] R.V Dukkipati. Dynamics of a wheelset on roller rig. *Vehicle System Dynamics*, 30:409–430, 1998.

[34] R.V. Dukkipati. Lateral stability analysis of a railway truck on roller rig. *Mechanism and Machine Theory*, 36:189–204, 2001.

[35] K. Ejiri, Y. Michitsuji, Y. Suda, S. Lin, and H. Sugiyama. Running stability analysis of independently rotating wheelset with negative tread conicity using scaled-model roller rig. In W. Zhang and M. Gong, editors, *23rd International Symposium on Dynamics of Vehicles on Roads and Tracks*, Qingdao, August 2013.

[36] R. Enblom. *On simulation of uniform wear and profile evolution in the wheel-rail contact*. Doctoral dissertation, Royal Institute of Technology (KTH), Stockholm, Sweden, 2006.

[37] A. Erba. *On the dynamic behavior of a railway bogie on a roller rig*. Master thesis, Politecnico di Milano, Milan, Italy, 2012.

[38] A. Facchinetti, S. Bruni, and W.H. Zhang. Rolling stock dynamic evaluation by means of laboratory tests. *International Journal of Railway Technology*, 2:99–123, 2013.

[39] D. Fletcher and J. Beynon. Development of a machine for closely controlled rolling contact fatigue and wear testing. *Journal of testing and evaluation*, 28(4):267–275, 2000.

[40] J.A. Greenwood and J.B.P. Williamson. The contact of nominally flat rough surfaces. *Proc. R. Soc. A*, 295:300–319, 1966.

[41] M. Gretzschel and A. Jaschinski. Design of an active wheelset on a scaled roller rig. *Vehicle System Dynamics*, 41:365–381, 2004.

[42] H. Hertz. Über die berührung fester elastische körper. *J Für Die Reine U Angew Math*, 92:156–171, 1882.

[43] H. Hur, J. Park, W. You, and T. Park. A study on the critical speed of worn wheel profile using a scale model. *Journal of Mechanical Science and Technology*, 23:2790–2800, 2009.

[44] S. Iwnicki. *The Manchester Benchmarks for Rail Vehicle Simulation (Supplement Vehicle System Dynamics)*. CRC Press, 1999.

[45] S. Iwnicki and A. Wickens. Validation of a MATLAB railway vehicle simulation using a scale roller rig. *Vehicle System Dynamics*, 30(3-4):257–270, 1998.

[46] M.H.A. Janssens and B. Asmussen. Curve squeal workpackage 4b: Rig testing inventory. ERRI project report, UIC, 2003.

[47] A. Jaschinski, H. Chollet, S.D. Iwnicki, A. H. Wickens, and J. V. Würzen. The application of the roller rigs to railway vehicle dynamics. *Vehicle System Dynamics*, 31:345–392, 1999.

[48] T. Jendel. Prediction of wheel profile wear-comparisons with measurements. *Wear*, 253:89–99, 2000.

[49] T. Jendel and M. Berg. Prediction of wheel profile wear. *Vehicle System Dynamics*, Supplement 37:502–513, 2002.

[50] Y. Jin, M. Ishida, and A. Namura. Experimental simulation and prediction of wear of wheel flange and rail gauge corner. *Wear*, 271:259–267, 2011.

[51] K.L. Johnson. The effect of tangential contact force upon the rolling motion of an elastic sphere on a plane. *Transactions of ASME, Journal of Applied Mechanics*, pages 339–346, 1958.

[52] K.L. Johnson. *Contact Mechanics*. Cambridge University Press, 1985.

[53] R. Johnson and D. Wichern. *Applied Multivariate Statistical Analysis (6th Edition)*. Pearson, 2007.

[54] J. Kalivoda and P. Bauer. Curving behaviour of 2-axle bogie with independently rotating wheels-simulations and scaled roller rig tests. In W. Zhang and M. Gong, editors, *23rd International Symposium on Dynamics of Vehicles on Roads and Tracks*, 2013.

[55] J.J. Kalker. *On the Rolling Contact of Two Elastic Bodies in the Presence of Dry Friction*. Doctoral dissertation, Delft University of Technology, Delft, The Netherlands, 1967.

[56] J.J. Kalker. A fast algorithm for the simplified theory of rolling contact. *Vehicle System Dynamics*, 11:1–13, 1982.

[57] J.J. Kalker. *Three-Dimensional Elastic Bodies in Rolling Contact*. Kluwer Academic Publishers, Dordrecht/ Boston/ London, 1990.

[58] A. Keylin and M. Ahmadian. Wheel-rail contact characteristics on a tangent track vs a roller rig. In C. Lambert and G. Holst, editors, *Proceedings of the ASME 2012 Rail Transportation Division Fall Technical Conference*, 2012.

[59] W. Kik, D. Moelle, C. Bogo, and G. Ferrarotti. The Manchester benchmarks ADAMS/rail - MEDYNA statement of methods. *Vehicle System Dynamics*, Supplement 31:49–65, 1999.

[60] W. Kik and J. Piotrowski. A fast, approximate method to calculate normal load at contact between wheel and rail and creep forces during rolling. In I. Zobory, editor, *Proceedings of 2nd Mini-conference on contact mech.and wear of rail/wheel systems*, 1996.

[61] N. Kim and T. Park. A study on the dynamic performance of the 200 km/h Korean tilting train by means of roller rig test. *Journal of Mechanical Science and Technology*, 23:910–913, 2009.

[62] K. Knothe. History of wheel/rail contact mechanics: From Redtenbacher to Kalker. *Vehicle System Dynamics*, 46(1-2):9–26, 2008.

[63] K. Knothe and H. Le The. A contribution to calculation of contact stress distribution between elastic bodies of revolution with non-elliptical contact area. *Computers and Structures*, 18:1025–1033, 1984.

[64] K. Knothe and H. Le The. A method for the analysis of the tangential stresses and the wear distribution between two elastic bodies of revolution in rolling contact. *Int. J. Solids Structures*, 21(8):889–906, 1985.

[65] S. Kumar and N.A. Allsayyed. Wheel/rail adhesion wear investigation using a quarter scale laboratory testing facility. In *Proceedings of the IEEE*, pages 247–254, January 1996.

[66] Y. Kunimatsu and Y. Terumichi. Vehicle models for the dynamic behaviour of roller rigs in a running test. In *Proceedings of the Second International Conference on Railway Technology: Research, Development and Maintenance*, August 2014.

[67] R. Lewis, F. Braghin, A. Ward, S. Bruni, R.S. Dwyer-Joyce, K. Bel Knani, and P. Bologna. Integrating dynamics and wear modelling to predict railway wheel profile evolution. In *Proceedings of 6th International Conference on Contact Mechanics and Wear of Rail/Wheel Systems*, June 2003.

[68] R. Lewis and U. Olofsson. Mapping rail wear regimes and transitions. *Wear*, 257:721–729, 2004.

Bibliography

[69] Z.L. Li. *Wheel-rail rolling contact and its application to wear simulation*. Doctoral dissertation, Delft University of Technology, Delft, The Netherlands, 2002.

[70] Z.L. Li and J.J. Kalker. Simulation of severe wheel-rail wear. In *Proceedings of the Sixth International Conference on Computer Aided Design, Manufacture and Operation in the Railway and Other Advanced Mass Transit Systems*, pages 393–402. Computational Mechanics Publications, 1998.

[71] C. Linder. *Verschleiss von Eisenbahnrädern mit Unrundheiten*. Doctoral dissertation, Techn. Wiss. ETH Zürich, Zürich, 1997.

[72] B.B. Liu and S. Bruni. A method for testing railway wheel sets on a full-scale roller rig. *Vehicle System Dynamics*, 53(9):1331–1348, 2015.

[73] B.B. Liu, S. Bruni, and C.Y. Chang. Mechatronic system simulation of a full-scale roller rig for a single wheelset. In *Proceedings of the Second International Conference on Railway Technology: Research, Development and Maintenance*, August 2014.

[74] Q. Liu, B. Zhang, and Z. Zhou. An experimental study of rail corrugation. *Wear*, 255:1121–1126, 2005.

[75] T. Matsudaira, N. Matsui, S. Arai, and K. Jokose. Problems on hunting of railway vehicle on test stand. *Trans. ASME. J. Eng. Ind. ser. B*, 91(3):879–885, 1969.

[76] A. Matsumoto, Y. Sato, M. Nakata, M. Tanimoto, and K. Qi. Wheel-rail contact mechanics at full scale on the test stand. *Wear*, 191:101–106, 1996.

[77] A. Matsumoto, Y. Sato, H. Ohno, T. Mizuma, Y.Suda, M. Tanimoto, and Y. Oka. Study on curving performance of railway bogies by using full-scale stand test. *Vehicle System Dynamics*, Supplement 44:862–873, 2006.

[78] A. Matsumoto, Y. Sato, H. Ono, and Y. Wang. Creep force characteristics between rail and wheel on scaled model. *Wear*, 253(1):199–203, 2002.

[79] S.Z. Meymand, M.J. Craft, and M. Ahmadian. On the application of roller rigs for studying rail vehicle systems. In C. Lambert and G. Holst, editors, *Proceedings of the ASME 2013 Rail Transportation Division Fall Technical Conference*, pages 147–156, Singapore, October 2013. World Scientific.

[80] M. Miyamoto. JR rolling stock testing plant capable of testing at a speed of 500 km/h. Quarterly report 32, Railway Technical Research Institute, Japan, 1991.

[81] M. Naeimi, Z.L. Li, and R. Dollevoet. Scaling strategy of a new experimental rig for wheel-rail contact. *World Academy of Science, Engineering and Technology International Journal of Mechanical, Aerospace, Industrial and Mechatronics Engineering*, 8(12):1787–1794, 2014.

[82] T.G. Pearce and N.D. Sherratt. Prediction of wheel profile wear. *Wear*, 144:343–351, 1991.

[83] J. Piotrowski and H. Chollet. Wheel-rail contact models for vehicle system dynamics including multi-point contact. *Vehicle System Dynamics*, 43(6-7):455–483, 2005.

[84] J. Piotrowski and W. Kik. A simplified model of wheel/rail contact mechanics for non-Hertzian problems and its application in rail vehicle dynamic simulations. *Vehicle System Dynamics*, 46(2):27–48, 2008.

[85] O. Polach. A fast wheel-rail forces calculation computer code. *Vehicle System Dynamics*, Supplement 33:782–739, 1999.

[86] J. Pombo, J. Ambrósio, M.Pereira, R. Lewis, R. Dwyer-Joyce, C. Ariaudo, and N. Kuka. Development of a wear prediction tool for steel railway wheels using three alternative wear functions. *Wear*, 271:238–245, 2011.

[87] J. Pombo, J. Ambrósio, and M. Silva. A new wheel-rail contact model for railway dynamics. *Vehicle System Dynamics*, 45(2):165–189, 2007.

[88] E. Rabinowicz. *Friction and wear of materials*. John Wiley and Sons, New York, 1965.

[89] F. J. Redtenbacher. *Die Gesetze des Locomotiv-Baues*. Mannheim, 1855.

[90] A. Rovira, A. Roda, R. Lewis, and M.B. Marshall. Application of fastsim with variable coefficient of friction using twin disc experimental measurements. *Wear*, 274:109–126, 2012.

[91] J. Santamaría, E. G. Vadillo, and J. Gómez. A comprehensive method for the elastic calculation of the two-point wheel-rail contact. *Vehicle System Dynamics*, Supplement 44:240–250, 2006.

[92] A. Schmid. Generation of excitation data for a wheel/rail system test rig using simulation. In *SIMPACK User Meeting*, August 2003.

[93] A.A. Shabana, K.E. Zaazaa, and H. Sugiyama. *Railroad vehicle dynamics : a computational approach*, chapter 1, Introduction, pages 1–33. Taylor & Francis Group, LLC, Boca Raton, 2007.

[94] Z.Y. Shen, J.K. Hendrick, and J.A. Elkins. A comparison of alternative creep-force models for rail vehicle dynamic analysis. *Vehicle System Dynamics*, 12:79–87, 1983.

[95] M.Sh. Sichani, R. Enblom, and M. Berg. Comparison of non-elliptic contact models: towards fast and accurate modelling of wheel-rail contact. *Wear*, 314:111–117, 2014.

[96] M.Sh. Sichani, R. Enblom, and M. Berg. A novel method to model wheel-rail normal contact in vehicle dynamics simulation. *Vehicle System Dynamics*, 52:1752–1764, 2014.

[97] SIMPACK AG. *SIMPACK documentation-Version 8.904a*, 2011.

[98] M. Taheri and M. Ahmadian. Contact patch comparison between a roller rig and tangent track for a single wheelset. In C. Lambert and G. Holst, editors, *Proceedings of the Joint Rail Conference*, 2012.

[99] D. Ullrich. Simulation of contact phenomena at full-scale wheel-on-rail test rigs. In *Proceedings of the Second International Conference on Railway Technology: Research, Development and Maintenance*, August 2014.

[100] D. Ullrich and M. Luke. Simulating rolling-contact fatigue and wear on a wheel/rail simulation test rig. In *World Congress on Railway Research*. UIC, November 2001.

[101] P. J. Vermeulen and K. L. Johnson. Contact of nonspherical elastic bodies transmitting tangential forces. *Journal of Applied Mechanics*, 1964.

[102] K.D. Vo, H.T. Zhu, A.K. Tieu, and P.B Kosasih. FE method to predict damage formation on curved track for various worn status of wheel/rail profiles. *Wear*, 322–323:61–75, 2015.

[103] E.A.H. Vollebregt. User guide for contact, rolling and sliding contact with friction. Technical report TR09-03, VORtech BV, Delft, The Netherlands, 2015. version 15.1.

[104] E.A.H. Vollebregt and P. Wilders. Fastsim2: a second-order accurate frictional rolling contact algorithm. *Comput Mech.*, 47:105–116, 2011.

[105] W. Wang, H. Zhang, H. Wang, Q. Liu, and M. Zhu. Study on the adhesion behaviour of wheel/rail under oil, water and sanding conditions. *Wear*, 271:2693–2698, 2011.

[106] L. Wei, J. Zeng, and R. Luo. Effect of roller rig conditions on stability test for high speed vehicles. In W. Zhang and M. Gong, editors, *23rd International Symposium on Dynamics of Vehicles on Roads and Tracks*, Qingdao, August 2013.

[107] C. Weidemann. State-of-the-art railway vehicle design with multi-body simulation. *Journal of Mechanical Systems for Transportation and Logistics*, 3(1):12–26, 2010.

[108] A.H. Wickens. *Fundamentals of rail vehicle dynamics : guidance and stability*. Swets & Zeitlinger Publishers, Lisse, The Netherlands, 2003.

[109] A.H. Wickens and A.O. Gilcrist. The dynamic of railway vehicle on straight track: Fundamental considerations of lateral stability. *Proc. I. Mech. E*, 180:29–44, 1965.

[110] M. Yan. *A study of the inherent errors in a roller rig model of railway vehicle dynamic behaviour*. ME thesis, Manchester Metropolitan University, Manchester, UK, 1993.

[111] W. Yan and F.D. Fischer. Applicability of the Hertz contact theory to rail-wheel contact problem. *Arch. Appl. Mech.*, 70:255–268, 2000.

[112] G. Yang. *Dynamic analysis of railway wheelsets and complete vehicle systems*. Doctoral dissertation, Delft University of Technology, Delft, The Netherlands, 1993.

[113] Y.Q. Zeng, X.G. Shu, C.H. Wang, and W.D. Yu. Study on three-dimensional wheel/rail contact geometry using generalized projection contour method. In W. Zhang and M. Gong, editors, *23rd International Symposium on Dynamics of Vehicles on Roads and Tracks*, Qingdao, August 2013.

[114] W.H. Zhang, J.Z. Chen, X.J. Wu, and X.S. Jin. Wheel/rail adhesion and analysis by using full scale roller rig. *Wear*, 253:82–88, 2002.

[115] W.H. Zhang, H.Y. Dai, Z.Y. Shen, and J. Zeng. *Handbook of railway vehicle dynamics*, chapter 14, Roller rigs, pages 458–504. Taylor & Francis Group, Boca Raton, 2006.

[116] Y. Zhu, J. Sundh, and U. Olofsson. A tribological view of wheel-rail wear maps. *International Journal of Railway Technology*, 2:79–91, 2013.

[117] I. Zobory. Prediction of wheel/rail profile wear. *Vehicle System Dynamics*, 28:221–259, 1997.